EVOLUTION OF CORONAL MASS EJECTION LONGITUDINAL STRUCTURE THROUGH INTERPLANETARY SPACE

Lauren Ashleigh James

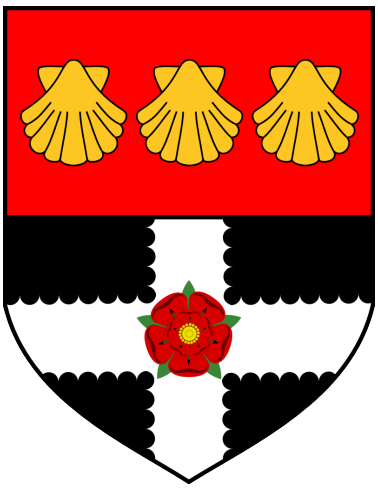

Department of Meteorology
School of Mathematical, Physical and Computational Sciences
University of Reading

A thesis presented for the degree of
Doctor of Philosophy

May 2023

Abstract

Accurately forecasting the arrival of Coronal Mass Ejections (CME) at Earth is important to enable the mitigation of the associated space weather risks to society. This is only possible with accurate modelling of the event. To do so, we must understand the propagation of a CME through the heliosphere and quantify the performance of models through comparison with spacecraft observations. For the 12 December 2008 Earth-directed CME event, we compute ensembles using the Heliospheric Upwind eXtrapolation with Time dependencies (HUXt) solar wind model to analyse CME distortion with a structured solar wind and explore hindcast Arrival Time Error (ATE). By highlighting the impact CME shape has on Root-Mean-Square-Error (RMSE) values, we show that time-elongation profiles of fronts captured by the *Heliospheric Imager* (HI)-1 instrument onboard *Solar-TErrestrial RElations Observatory* (STEREO) mission matches those of the modelled CME nose and flank and can therefore be used to infer details of the longitudinal extent of the CME. We then show that accounting for CME distortion is important in enabling accurate estimates of the CME arrival at Earth. This can be achieved by either using observations of multiple features in HI data to infer CME evolution or mapping the solar wind back to a lower inner boundary to allow CMEs to be distorted close to the Sun. For the event studied, we show that these two approaches resulted in a reduced RMSE by at least 19% compared to tracking the flank only or when compared to the CME deterministic run the RMSEs fell by 12% and 22% respectively, and obtain ATE values of less than three hours. By these approaches, the lead time value is assessed as a function of HI observation quantity.

Declaration

I confirm that this is my own work and that the use of all material from other sources has been properly and fully acknowledged.

		23/05/2023
Lauren A. James		Date

Acknowledgements

First and foremost, my gratitude is expressed to my supervisors Professor Chris Scott and Professor Mathew Owens for their endless encouragement throughout the last few years and for providing me with the opportunity for me to pursue a PhD. I would also like to thank Dr Luke Barnard for their technical support and insightful ideas. My appreciation is extended to the department's SPATE research group who have always created a welcoming environment and provided useful feedback throughout my research. Thank you to Professor Mike Lockwood and Dr Chris Westbrook for being a supportive monitoring committee, and for their insightful comments and suggestions. I have made some endearing friends throughout my PhD experience. Thank you for keeping me in high spirits, and for your unwavering support and belief in me. Thank you to Reading Knights Korfball Club 2019-2022, who have provided endless memories, healthy escapism, and promoted happy well-being, especially throughout the pandemic. It was a pleasure to serve terms as the social secretary and the president during my PhD. This acknowledgement would not be personal without reference to a song which has enabled me to keep a positive and realistic view through the PhD ···

"Slow down, you're doin' fine.
You can't be everything you wanna be before your time."
- Vienna by Billy Joel

Lastly, I would like to thank the Science Technology Facilities Council for the studentship that allowed me to conduct this thesis. The skills developed and opportunities to present my work have been invaluable and will be beneficial to

future careers. When this project started 3.5 years ago, the forthcoming pandemic and the impact it would have on our lives were unseen. The unlimited support I received from family, friends, and colleagues never went unnoticed and it is the reason I am able to present this thesis. Thank you.

Contents

List of Abbreviations

Given below is a list of abbreviations that appear throughout the thesis. Names of spacecraft and onboard instruments are displayed in italics. In the case where it is not a true abbreviation (i.e., does not have a extended name), the reason for the naming convention is given in parenthesis.

ACE	*Advanced Composition Explorer*.
ASE	Arrival Speed Error.
ATE	Arrival Time Error.
BRaVDA	Burger Radial Variational Data Assimilation.
CAT	CME Analysis Tool.
CCMC	NASA's Community Coordinated Modeling Center.
CME	Coronal Mass Ejection.
COR	*Coronagraph*.
CR	Carrington Rotation.
ELCon	Elliptic Conversion.
ELEvoHI	ELipse Evolution model based on Heliospheric Imager.
ENLIL	(A large-scale, numerical model of the heliosphere, named after an ancient Mesopotamian god associated with wind, air, earth, and storms).

EUHFORIA European Heliospheric Forecasting Information Asset.

EUVI *Extreme UltraViolet Imager*.

FP Fixed-Phi.

GIC Geomagnetically Induced Current.

HCS Heliospheric Current Sheet.

HEEQ Heliocentric Earth Equatorial.

HI *Heliospheric Imager*.

HM Harmonic Mean.

HMF Heliospheric Magnetic Field.

HUXt Heliospheric Upwind eXtrapolation with Time dependencies.

IMPACT *In situ Measurements of PArticles and CME Transients*.

LASCO *Large Angle and Spectrometric Coronagraph*.

MAS Magnetohydrodynamic Algorithm outside a Sphere.

MHD Magnetohydrodynamic.

MOSWOC UK Met Office's Space Weather Operation Centre.

NASA National Aeronautics and Space Administration.

NOAA National Oceanic and Atmospheric Administration.

PLASTIC *PLAsma and SupraThermal Ion Composition*.

PSP NASA's *Parker Solar Probe*.

RMSE Root-Mean-Square-Error.

S/WAVES *STEREO/WAVES*.

SECCHI	*Sun-Earth Connection Coronal and Heliospheric Investigation*.
SEPs	Solar Energetic Particles.
SIR	Stream Interaction Regions.
SOHO	ESA's *Solar and Heliospheric Observatory*.
SSE	Self-Similar Expansion.
STEREO	*Solar-TErrestrial RElations Observatory*.
SWEPAM	*Solar Wind Electron, Proton, and Alpha Monitor*.
SWPC	NOAA's Space Weather Prediction Center.
WSA	Wang-Sheeley Arge (solar wind speed prediction method).

List of Figures

List of Tables

Chapter 1

Introduction

1.1 Thesis motivation

Space Weather is the study of disruptive changes to the near-Earth environment, resulting in an impact on technology (*Hapgood and Thomson*, 2018; *Hapgood et al.*, 2021). Short-term changes are driven by solar activity, with the main driver of geomagnetic activity on Earth being caused by Coronal Mass Ejections (CMEs). Technologies such as transport systems, satellites, and the power grids are susceptible to space weather events. As a result, our modern-day living is at risk of severe disruption and the UK Government now includes space weather events in its National Risk Register (*Cabinet*, 2020). Fortunately, risk mitigation techniques can be implemented to reduce detrimental impacts. However, for this to be feasible, accurate forecasting of space weather events is required.

CME forecasting is operational at the UK Met Office's Space Weather Operation Centre (MOSWOC) and NOAA's Space Weather Prediction Center (SWPC), for example, using computationally demanding numerical models of the Sun-Earth system. These models require near-Sun observations to simulate the Magnetohydrodynamic (MHD) environment and show CME distortion and expansion from onset out to Earth's orbit. Understanding the propagation of CMEs throughout the heliosphere

was greatly improved by the development of remote sensing images of the events throughout the heliosphere. The *Heliospheric Imager* (HI) instrument onboard *Solar-TErrestrial RElations Observatory* (STEREO) allowed structural features of CMEs to be identified via dense plasma regions which give higher intensity of scattered photospheric light. Interpretation of these features in two-dimensional images enables information about the three-dimensional shape to be inferred. This thesis will explore this, in particular the Ghost Front theory (*Scott et al.*, 2019), further through an in-depth analysis of a CME event.

Remote sensing images provide data that can be used to assess model performance in simulating CME propagation before the event reaches Earth. This gives improvement of the lead time of CME warning and initialisation of risk mitigation services. This thesis will demonstrate the use of HI data to quantify model performance for a CME case study and assess if there is value in the model performance for improving the accuracy of CME arrival predictions near-Earth.

As well as this, the thesis will present a technique to acknowledge inner boundary uncertainties in CME modelling. Ensemble modelling can be used to explore the parameter space by perturbing inner boundary conditions and statistically analysing differences in model outcome. However, the computation demand of models can limit the number of model runs that make up the ensemble. In recent years, an extremely efficient heliospheric model (*Owens et al.*, 2020a) has been developed allowing many-member ensembles to be computed (*Barnard et al.*, 2020).

1.2 Structure of the thesis

Space Weather is discussed in greater detail in Chapter 2 through a discussion of the Sun-Earth system, plasma physics, and the understanding of Coronal Mass Ejections from the Sun to Earth's environment. In Chapter 3, the discussion focuses on the observations of Coronal Mass Ejections. The STEREO mission and the onboard HI instrument are introduced in this chapter, thus, enabling interpretation of the remote sensing data used in the thesis. Through observations of CMEs, modelling methods have been developed. Some are designed to demonstrate the expansion of CMEs through the heliosphere, whilst others aim to estimate the near-Earth environment to inform space weather operations. A discussion of the broad range of models is

had in this chapter, with emphasis on models that aid operational forecasting.

The CME case study from 12 December 2008 is introduced in Chapter 4. Using HI data gathered during the event, the ghost front theory is explored. Furthermore, the method for an ensemble approach to CME modelling is discussed and the results of an ensemble-based hindcast are shown. This chapter thus explores whether the ghost front theory interpretation enhances the accuracy of estimating a CME arrival at L1. In Chapter 5, a novel technique is explored to model the distortion of a CME closer to the Sun by lowering the inner boundary of the model, after which, the experiment of the previous chapter is repeated.

Multiple HI observations of the same CME are presented. Therefore, in Chapter 6, the accuracy of the L1 estimated arrival is explored as a function of lead time, and of the quantity of HI observations used to inform the model. The ghost front interpretation of the bright front features in HI images is continued through this chapter.

The work is concluded in Chapter 7, including ideas for future work to enhance the findings presented.

Chapter 2

The Sun - Earth System

2.1 The Sun

The Sun is a 4.6 billion-year-old star positioned in the centre of our solar system. The solar atmosphere, known as the corona, is a plasma (ionized gas) consisting primarily of Hydrogen (about 92 %) and Helium (approximately 7.8 %), with traces of Oxygen, Carbon, and Nitrogen. It exhibits extremely high temperatures on the order of 10^6 K. On the other hand, the visible surface of the Sun, known as the photosphere, is considerable cooler (between 4000 K to 6000 K) which means the gas there is mainly neutral atoms with a very small percentage of ions present. An equilibrium of gravitational force and internal pressure from energy generation within the core holds the Sun together. The visible surface of the Sun, called the Photosphere, has a radius of 696 000 km, or 1 $R_\odot$ (solar radii). The structure of the Sun can be divided into its interior structure and its atmosphere, which have further divisions into several distinct regions (Figure 2.1) that are discussed in more detail in the following section.

2.1.1 Structure

The solar interior is shaped by energy generation and transfer within the Sun. It consists of three regions; the core, the radiative zone, and the convection zone. At the

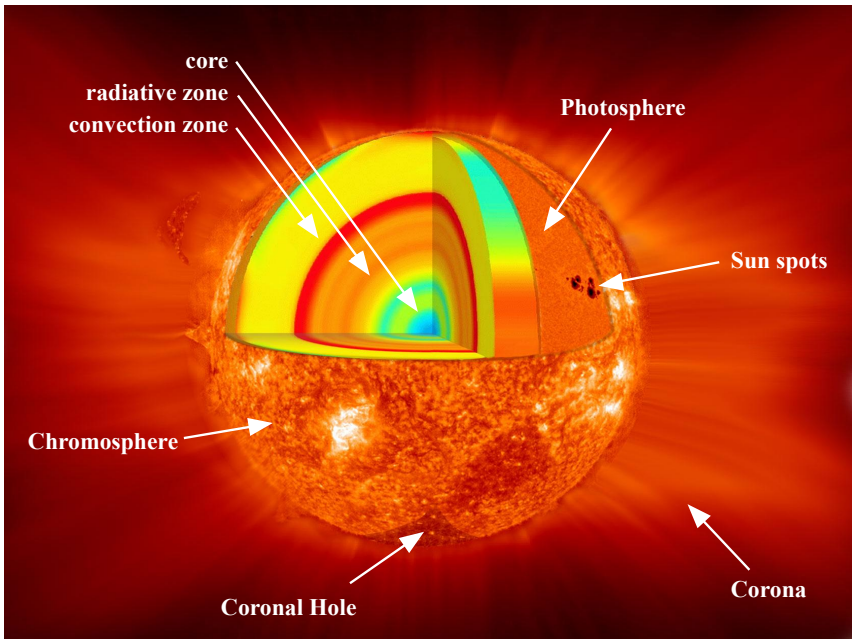

Figure 2.1: A labelled diagram of the Sun's layers. Sourced and adapted from the original version at NASA (`https://www.nasa.gov/mission_pages/sunearth/multimedia/Sunlayers.html`, accessed May 2023).

centre, the core extends to a radius of $0.2\,R_\odot$ and generates 99 % of the Sun's energy by fusion reactions, in which hydrogen is converted into helium and releases energy in the form of photons. The fusion reactions occur because the core has extremely high temperatures (15 million K) and high plasma density ($1.6 \times 10^5\,\mathrm{kg\,m^{-3}}$) due to a strong gravitational force.

In the radiation zone, between the heliocentric distances of $0.2\,R_\odot$ to $0.7\,R_\odot$, the generated energy is transferred away from the core by radiative diffusion of photons. The temperature gradient between the base and the top of the layer is sufficiently low such that convection cannot occur.

Above $0.7\,R_\odot$, the temperature gradient becomes great enough so that energy transfer is dominated by convective processes. The temperature at the base of the layer is sufficiently cool enough for heavy ions to keep hold of their electrons, trapping the heat and making the plasma unstable. Consequently, large-scale motions of plasma occur in the convection zone. The higher temperatures at the base of the convective zone create plasma parcels of lower density than their surroundings. These parcels of plasma rise to the surface of the Sun and cool, affecting its buoyancy

and causing it to fall back deeper into the Sun. A magnetic field which is present throughout the Sun's convection zone (discussed further in the next section). Buoyancy of a parcel increases when more magnetic field threads through it and aids the rising of parcels to the surface. This dynamic system produces a granulated appearance on the visible surface of the Sun. The boundary between the change in the dynamic behaviour of the plasma is called the *tachocline*. Here, it is believed the Sun's magnetic field is generated (*Browning et al.*, 2006; *Guerrero et al.*, 2016).

The solar surface is known as the Photosphere. Over its 500 km height, the temperature decreases from 6000 K to 4400 K. The plasma density is low enough so that photons can escape into the solar atmosphere and beyond.

Layers of the Sun's atmosphere are characterised by the vertical temperature profile, shown in Figure 2.2. Above the photosphere, the lowest part of the Chromosphere is the coolest layer of the Sun. The temperature slowly increases with radial distance up to 10 000 K at 2000 km. Over the whole radial distance of the chromosphere, plasma density declines logarithmically from $10^{-5}\,\mathrm{kg\,m^{-3}}$ to $10^{-9}\,\mathrm{kg\,m^{-3}}$.

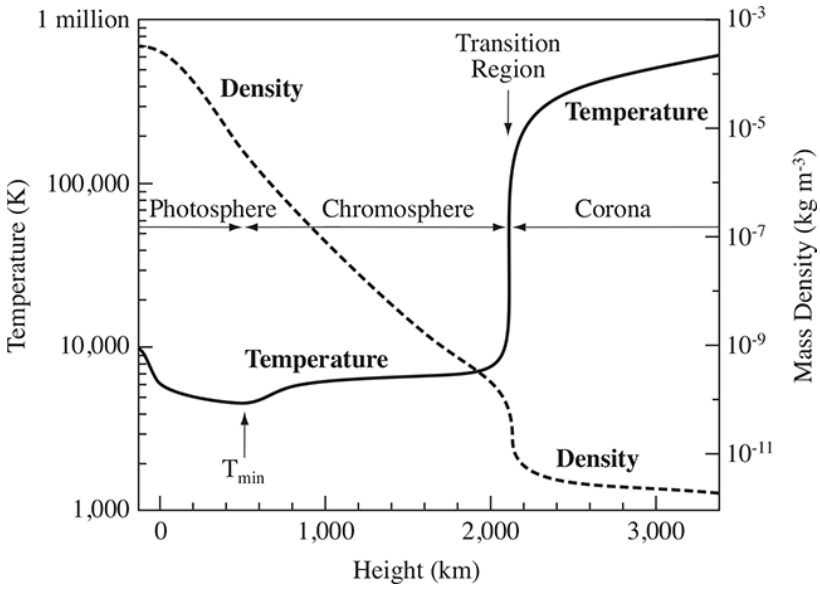

Figure 2.2: A schematic for the mean value of temperature and density as a function of height in the solar atmosphere. Sourced from *Priest* (2020).

A sudden enhancement of temperature, from 6×10^3 K to 10^6 K, occurs between 2000 km to 2200 km, marking the *transition region*. Plasma density decreases rapidly with height (10^{-9} kg m^{-3} to 10^{-12} kg m^{-3}). The cause for the rapid temperature increase in the transition region is an unexplained phenomenon (e.g., *Aschwanden et al.*, 2007; *Moortel and Browning*, 2015).

Beyond this is the corona. It is the least dense region of the solar atmosphere, approximately 10^{-12} kg m^{-3}, but also has the highest temperature. The temperature increases slowly with radial distance, up to 0.7×10^6 K at 3200 km from the photosphere, increasing to $\geq 1.6 \times 10^6$ K at greater distances. The reason for this intense heating remains unanswered, as discussed in previous studies (e.g. *Aschwanden et al.*, 2007; *Moortel and Browning*, 2015). The Sun's corona exhibits a significant temperature contrast with the cooler interstellar medium of space. This temperature difference creates a pressure imbalance, leading to a steep pressure gradient. Consequently, particles in the corona acquire speeds substantial enough to escape the corona, traveling anti-sunward at supersonic velocities and contribute to the formation of the solar wind.

2.1.2 Magnetic Field configuration

The extremely high temperatures within the Sun result in the fluid being ionised, forming a plasma. As this plasma moves, the motion of the charged particles creates an electrical current and, thus, a magnetic field (in accordance with Ampère's Law). The Sun rotates in the same sense as the planets orbital motion, the solar atmosphere takes 27 days to complete a full rotation as seen from Earth. However, the Sun is not a solid body and the rotation speed of the photosphere varies with latitude, slowing down towards the solar poles (*Stix*, 1989). One complete equatorial rotation is a Carrington Rotation (CR), after Richard *Carrington* (1859). Successive rotations have been labelled numerically since 1853. Due to plasma dynamics within the Sun, the magnetic field is generated by the *Solar Dynamo* producing a far more complex magnetic structure than is seen within solid planetary bodies (*Cameron et al.*, 2017).

At the ''minimum'' of the solar cycle, the Sun's magnetic field is dipolar, with the internal field lines aligned generally meridionally between the two poles. By differential rotation of the Sun, the poloidal magnetic field is dragged along with the

plasma forming a stretched field along regions of quickest rotation. This Ω-*effect* generates toroidal magnetic flux. Across 5-6 years of solar rotations, the magnetic field becomes wound around the Sun, therefore having a toroidal magnetic field. This is illustrated in Figure 2.3. Kinks appear as the magnetic field coils on themselves, called flux tubes. Due to magnetic buoyancy, the flux tubes are forced up through the solar surface and loop into the chromosphere, creating sunspots on the photosphere in the process (*Parker*, 1955).

The dense magnetic field threading through sunspots suppresses the transportation of plasma and energy upward through the outer convection zone (*Stix*, 2004; *Thomas and Weiss*, 1992). As a result, the sunspot temperature is approximately 2000 K cooler than the surrounding photosphere. Hence, these regions appear as darker spots when viewed at visible wavelengths of light (Figure 2.1), as was studied telescopically by Galileo (*Galilei*, 1613). Clusters of sunspots are known as *active regions*.

The protruding magnetic flux ropes are subjected to the α-*effect*, whereby the Coriolis force produces a rotation of the flux rope to generate a poloidal magnetic flux (*Steenbeck et al.*, 1966), as illustrated by the small inset in Figure 2.3. Now, the Sun's magnetic field is very structured and disorganised.

This complexity of the Sun's magnetic field cannot be sustained. The large magnetic structures looping above the photosphere constrain plasma within the flux rope. These are visible in images of the Sun. In Hα-solar disk images, they

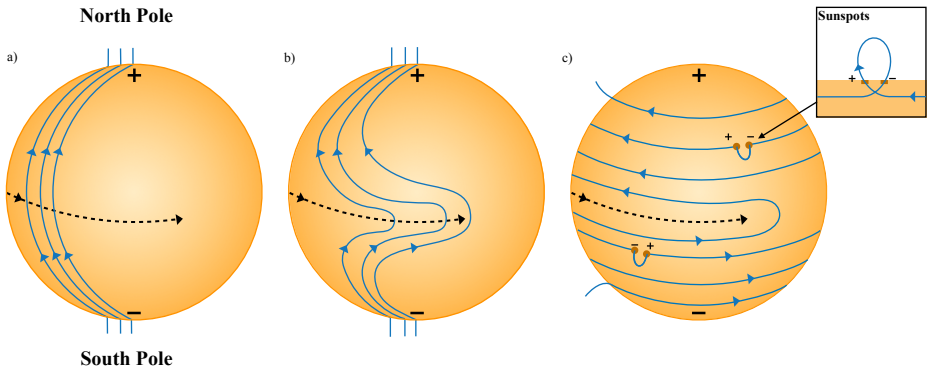

Figure 2.3: The Sun's differential rotation speeds across latitudes impact the structure of the magnetic field. These three panels illustrate a simple warping of the magnetic field lines. Adapted from *Moldwin* (2016).

present as dark lines called *filaments* since the plasma within the magnetic flux loop is cooler and denser than the photosphere. Meanwhile, if seen on the limb of the Sun and, thus, presented against the cooler chromosphere, the filaments are seen as bright features and now called *prominences*. Enhancement in the plasma density can result in an eventual imbalance of forces leading to a sudden eruption of plasma and magnetic field from the Sun. This is a Coronal Mass Ejection (CME), discussed in greater depth in Section 2.4. Reconnection in active regions and CME eruptions simplifies the once complex magnetic field structure of the Sun, organising the field back towards a dipole structure. As such, sunspot numbers are a common measure of solar activity.

2.1.3 Solar Cycle

A pair of sunspots lasts around 100 days; however, the total number of sunspots visible varies over a 11-year cycle called the *solar cycle*. At the start of the cycle, called *solar minimum*, a low count of sunspots appears at mid-latitudes on the photosphere and spot-free days are not uncommon. Over approximately 4 year there is a rapid rise in the total number of sunspots as the Sun's magnetic field becomes more complex. Eventually, *solar maximum* is reached; a peak in the total number of sunspots. A gradual descending phase of the total sunspot number occurs over the next 7 years approximately, bringing the Sun back to solar minimum. Over the cycle from minimum to minimum, the sunspots appear at lower latitudes until they are appearing just above the solar equator in both hemispheres. Figure 2.4 demonstrates this, showing the position of sunspots and the average daily sunspot count since 1874. This trend can be used to identify the end of the solar cycle and mid-latitude sunspots start to appear again for the next solar cycle. Consequently, sections of the solar cycle indicate the level of solar magnetic activity. This is vital for estimating the rate at which solar transients occur. For example, CMEs may erupt at a rate of 1 per a day during solar minimum, but increase to 5 per a day during solar maximum (*Webb and Howard*, 2012).

The solar dynamo process results in the polarity of the Sun's field swapping every solar cycle. It will take 22 years for the Sun to be back in its ''original'' state - this is called the *Hale Cycle*.

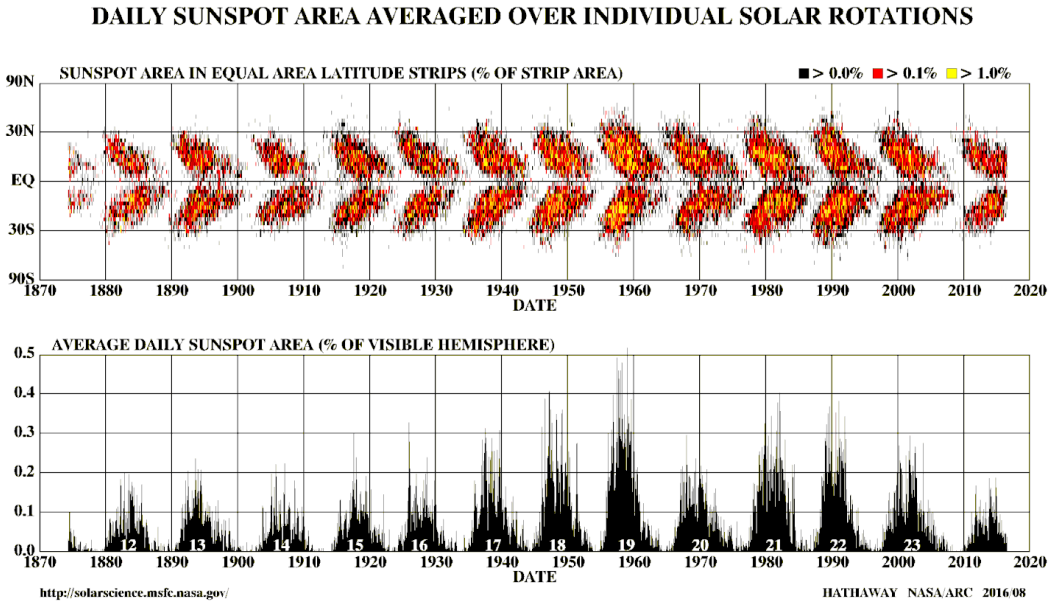

Figure 2.4: The variation in daily average sunspot area position and relative size as a function of time, based on observations since May 1874. (Top) The latitudinal position of sunspot regions. Measurements are made as a percentage of the observational area (i.e., latitude strips of equal area) that is a sunspot region, where the percentage value corresponds to the colour of the data. (Bottom) The percentage of visible hemisphere that is covered by the daily average sunspot area. The variation trends of the two plots correspond to the 11-year solar cycle. Sourced from *Hathaway* (2015).

2.1.4 Magnetic Atmosphere

The Sun's magnetic field extends out through the solar atmosphere, giving structure to the corona made visible in light emitted by the photosphere that is scattered towards the observer by plasma contained within these field lines when seen in X-ray wavelengths. In an idealised dipole structure, the Sun's magnetic field will connect the hemispheres of opposite polarity. For a surface surrounding the dipole at a set distance away from the Sun, some field lines are shallow enough to loop within the surface height such that they have a ''closed'' appearance. Others will loop at heights greater than the surface resulting in field lines being ''open'' and threading through the surface. In one hemisphere, the open field lines will point away from the Sun,

and in the other hemisphere, they will point toward the Sun. However, in reality, the loops connecting these open field lines are carried away from the Sun due to the frozen-in flux theorem (Section 2.2.2), stating that the magnetic field is forced to move with the plasma flowing out of the solar atmosphere (in the sense that the field lines move with the plasma velocity that is define as the mean of the ions and electron velocities, weighted by their mass). In the corona, closed field lines show as bright features called *coronal loops*; plasma is confined to closed magnetic field lines, with temperatures up to 2×10^6 K (*Reale*, 2010). Dark regions are known as *coronal holes* and correspond to open field lines (*Wang*, 2009). Plasma flows away from the solar atmosphere in these regions creating a cooler (1.2×10^6 K), less dense space. Open field lines emerge from the polar regions and closed field lines are positioned over the equator during solar minimum. But during the solar cycle, they both appear across all latitudes.

2.2 Plasma Physics

When discussing the Sun-Earth system, plasma physics is essential to understand the interconnectivity of the system. Plasma physics can be described by either small-scale motions of particles or by large-scale motions of plasma. On small spatial scales it is useful to consider the motion of individual particles in electric and magnetic fields that are imposed from elsewhere - this is called a kinetic approach. When generally describing the Sun's space environment, large-scale motions are considered whereby the plasma is treated as a fluid - this is called Magnetohydrodynamic (MHD). This was essential in the development of theories (i.e. coronal expansion) that have allowed us to understand the heliospheric environment. Thus, the majority of numerical models of the Sun-Earth system are based on MHD simulations, as to be discussed in Chapter 3. Here the conventions of MHD are summarised.

2.2.1 Magnetohydrodynamics

In MHD, electrical and magnetic fields are self-consistently evaluated with the plasma motion. Maxwells equations, the foundation of electromagnetism, describe the behaviour of plasma in this state. These equations are not specified here but are included throughout the chapter where required for further physics applications.

From these, an important MHD equation can be derived which describes how the magnetic force, B varies with time, t:

$$\frac{\partial \boldsymbol{B}}{\partial t} = \nabla \times (\boldsymbol{v} \times \boldsymbol{B}) + \frac{\nabla^2 \boldsymbol{B}}{\mu_0 \sigma} \tag{2.1}$$

where μ_0 is the permeability of free space, v is the plasma velocity, and σ is the plasma conductivity. This is called the magnetic induction equation. The two components of this equation are referred to as the conductive term and the diffusive terms, respectively. In large scale plasmas, the large spatial scale and high electrical conductivity make the conductive term much larger than the diffusive term and we can often neglect the latter. We call MHD theory that neglects the diffusive term *ideal MHD*.

Low-density space plasma is considered collisionless, meaning that plasma will only interact with the magnetic field and the electric field and the effect of collisions between ions and electrons with other ions and electrons (or any other particles present) have negligible effect. As a result, the plasma can be thought to have no electrical resistivity, no thermal conductivity and has infinite viscosity.

Under these assumptions, mass cannot be made or destroyed (i.e., mass continuity equation):

$$\frac{\partial \rho}{\partial t} + \nabla(\rho \boldsymbol{v}) = 0 \tag{2.2}$$

where ρ is the plasma density. A further rule of MHD is that magnetic fields cannot diverge (i.e., magnetic monopoles do not exist and indeed they have never been observed of detected):

$$\nabla \cdot \boldsymbol{B} = 0 \tag{2.3}$$

2.2.2 Frozen-in Flux Theorem

An important concept of ideal MHD is the frozen-in flux theorem. The frozen-in flux theorem states that the magnetic field is constrained to move with the ‘‘plasma velocity’’, which is the average of the bulk flow velocities of the ions and electrons, weighted by their mass.

Since plasma is an electrified fluid, differences between the ion and electron velocities (i.e., currents), by Ampère's law, produce a magnetic force. The relation of how the magnetic force varies with time can be described with the magnetic

induction equation (Equation 2.1). In ideal MHD we neglect the diffusive term and the magnetic induction equation reduces to its convective term only:

$$\frac{\partial \boldsymbol{B}}{\partial t} = \nabla \times (\boldsymbol{v} \times \boldsymbol{B}) \tag{2.4}$$

Magnetic field interaction with an electrical field is given by Faraday's Law. In its differential form, it is given that:

$$\frac{\partial \boldsymbol{B}}{\partial t} = -\nabla \times \boldsymbol{E} \tag{2.5}$$

where $\boldsymbol{E}$ is the electric field. By Equation 2.4 and Equation 2.5, it can be said that for plasma at the convective limit then

$$\boldsymbol{E} = -\boldsymbol{v} \times \boldsymbol{B} \tag{2.6}$$

Therefore, for a surface in space, s, the magnetic flux, F, can be given by the integral form of Faraday's law:

$$\frac{\partial F}{\partial t} = -\oint_s \boldsymbol{E} \cdot \delta \boldsymbol{l} = +\oint_s [\boldsymbol{v} \times \boldsymbol{B}] \cdot \delta \boldsymbol{l} \tag{2.7}$$

where $\boldsymbol{l}$ is the length of the loop encasing s,

Furthermore, it is important to consider the rate at which the magnetic field moves through space. Assuming the magnetic field has the equivalent velocity to the plasma, $\boldsymbol{v}$, then the rate of change of magnetic flux across the length, δl, of the loop, s is:

$$\frac{\partial F}{\partial t} = \upsilon B \delta l = [\boldsymbol{v} \times \boldsymbol{B}] \cdot \delta \boldsymbol{l} \tag{2.8}$$

Integrate around the loop, s:

$$\frac{\partial F}{\partial t} = \oint_s \frac{\partial f}{\partial t} = \oint_s [\boldsymbol{v} \times \boldsymbol{B}] \cdot \delta \boldsymbol{l} \tag{2.9}$$

As Equation 2.7 and Equation 2.9 are equivalent the assumption of the magnetic field moving with the plasma velocity must be true, and therefore, the frozen-in theorem must apply.

2.3 The Heliosphere

The Sun influences a large region in space called the heliosphere. Here, the supersonic solar wind flows continuously away from the Sun, carrying magnetised plasma out

as far as 90 au – 100 au and marking the edge of the heliosphere. Local disturbances in the solar wind are produced from the dynamic Sun, and can impact planets and orbiting bodies (section 2.5).

2.3.1 The Solar Wind

The solar wind is driven by the large pressure gradient between the hot corona and the cooler interstellar medium. Close to the Sun the plasma beta is very low but it rises and is very large throughout most of the heliosphere. Plasma beta, β, is a quantity that describes whether a region of plasma is dominated by magnetic pressure (p_B; Equation 2.11) or thermal pressure (p_T; equation 2.12) via a ratio :

$$\beta = \frac{p_T}{p_B} \tag{2.10}$$

$$p_B = \frac{B^2}{2\mu_0} \tag{2.11}$$

$$p_T = nk_BT \tag{2.12}$$

therefore,

$$\beta = \frac{2nk_BT\mu_0}{B^2} \tag{2.13}$$

where B is the magnetic field, μ_0 is the permeability of free space, n is the number density of electrons, k_B is Boltzmann's constant, and T is temperature.

If $\beta < 1$, the magnetic pressure is dominant (as in the corona), whereas if $\beta > 1$ then thermal pressure dominates and the motions are dominated by the plasma, with the magnetic field carried by the motion. The transition between these two conditions occurs between $10\,R_\odot$ to $20\,R_\odot$ distance from the Sun, above which plasma outflows from the Sun's atmosphere in a radial direction. This is the solar wind. Note that the frozen-in theorem still applies and means that the solar wind drags solar magnetic field outward which also fills the heliosphere.

Coronal Expansion

Parker (1958) theorised an idealised model of the solar wind (i.e., in this case a theory of coronal expansion) which is spherically symmetrical and time independent. The focus of this is to balance the pressure of the coronal and the interplanetary medium

using the conservation of mass (equation 2.14) and the conservation of momentum (equation 2.15). From the assumptions, these equations can be expressed as:

$$\boldsymbol{\nabla} \cdot \rho \boldsymbol{v} = 0 \tag{2.14}$$

$$\rho \boldsymbol{v} \cdot \nabla \boldsymbol{v} = -\nabla p + \boldsymbol{j} \times \boldsymbol{B} + \rho \boldsymbol{F}_g \tag{2.15}$$

where ρ is the plasma density, v is the bulk plasma outflow velocity, p is the plasma pressure, $\boldsymbol{j} \times \boldsymbol{B}$ is the force on plasma due to the magnetic field, and F_g is the force due to gravity.

The solar wind is treated as an ideal one-fluid gas of constant temperature, where the magnetic force is considered negligible. Thus, plasma density varies as a function of distance. Given this, a function of plasma velocity with radial distance is:

$$\left(v^2 - \frac{2k_B T}{m}\right) \frac{1}{v} \frac{\partial u}{\partial r} = \frac{4k_B T}{mr} - \frac{GM_\odot}{r^2} \tag{2.16}$$

where k_B is the Boltzmann constant, G in the universal gravitational constant, $M_\odot$ is the solar mass, and r is the radial distance from the Sun. Equation 2.16 has four solutions, presented in Figure 2.5. Only one solution is viable, confirmed with spacecraft observations. Solar wind velocity increases with radial distance in such a way that it becomes supersonic beyond a ‘‘critical radius’’.

$$r_{cr} = \frac{GM_\odot m}{4k_B T} \tag{2.17}$$

Alfvénic Speed

The Alfvén wave is an electromagnetic-hydromagnetic wave (*Alfvén*, 1942; *Mathioudakis et al.*, 2013; *Tomczyk et al.*, 2007). In plasma, information is passed with incompressible oscillations of ions and magnetic field at a speed of v_a :

$$v_A = \frac{B}{\sqrt{\mu_0 \rho}} \tag{2.18}$$

where B is the strength of magnetic field, μ_0 is the magnetic permeability of free space, and ρ is the density of ions.

There is a region around the Sun at which the speed of the solar wind, V, is equivalent to the Alfvén wave speed ($|V| = |v_a|$), called the Alfvén Surface or the critical region. This region is important as it marks the end of the solar atmosphere

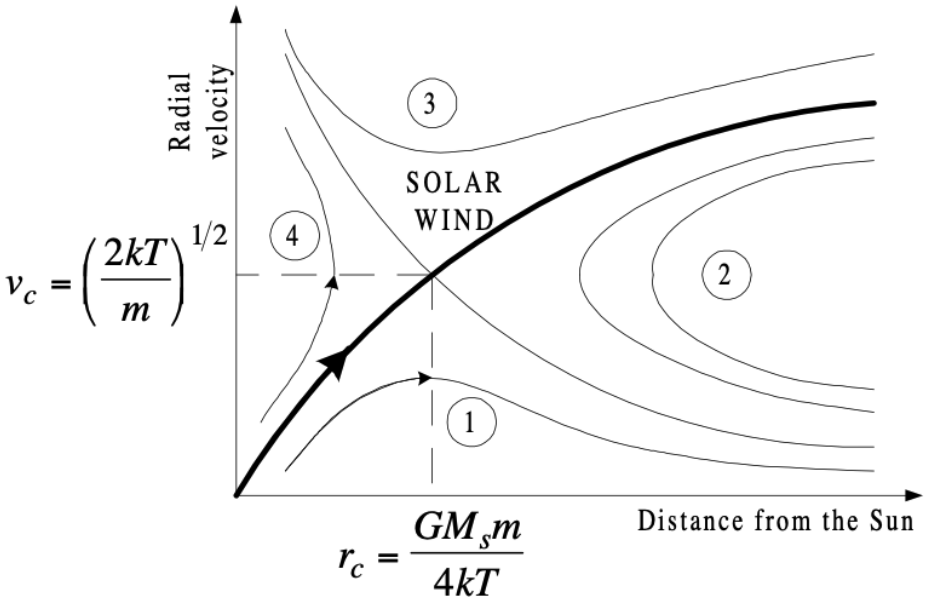

Figure 2.5: The solutions to Parker's coronal expansion equation. The only solution consistent with observations is shown by the bold line, indicating the solar wind speed increases with radial distance from the Sun. Sourced from `http://www.sp.ph.imperial.ac.uk/~mkd/AndreHandout.pdf`

and the beginning of the solar wind flow (*Adhikari et al.*, 2019; *DeForest et al.*, 2014). Within the solar atmosphere, the material flows at sub-Alfvénic speeds ($|V| \ll |\upsilon_a|$). Beyond the critical region, the solar wind carries material away from the Sun at super-Alfvénic speeds ($|V| \gg |\upsilon_a|$). At such large radial distances, the plasma become disassociated from the Sun and cannot propagate back to the corona.

The Alfvén surface was estimated to be between $10\,R_\odot$ to $20\,R_\odot$ from the Sun center (*Zhao and Hoeksema*, 2010). In April 2021, NASA's near-Sun orbiting mission, NASA's *Parker Solar Probe* (PSP), encountered periods of sub-Alfvénic speeds at a distance of $18.8\,R_\odot$ for the first time in history (*Bandyopadhyay et al.*, 2022; *Smith*, 2021). The surface is irregular, as is illustrated by NASA in their PSP animation online at `https://svs.gsfc.nasa.gov/14036#section_credits`. In the upcoming years, there will be the opportunity to learn more about the Alfvén Surface as more data is gathered by spacecraft.

Beyond the critical region, the solar wind velocity will exceed the speed of sound, V_s. The Mach number (Equation 2.19 is the ratio of these two values, and by M

exceeding 1.0 it can be said that the solar wind speed is supersonic.

$$M = \frac{V}{V_s} \tag{2.19}$$

2.3.2 The heliospheric magnetic field

The solar wind continuities to follow the frozen-in flux theorem. The radial outflow of the solar wind carries the fixed magnetic field along, creating the Heliospheric Magnetic Field (HMF). Meanwhile, the magnetic field remains attached to a source

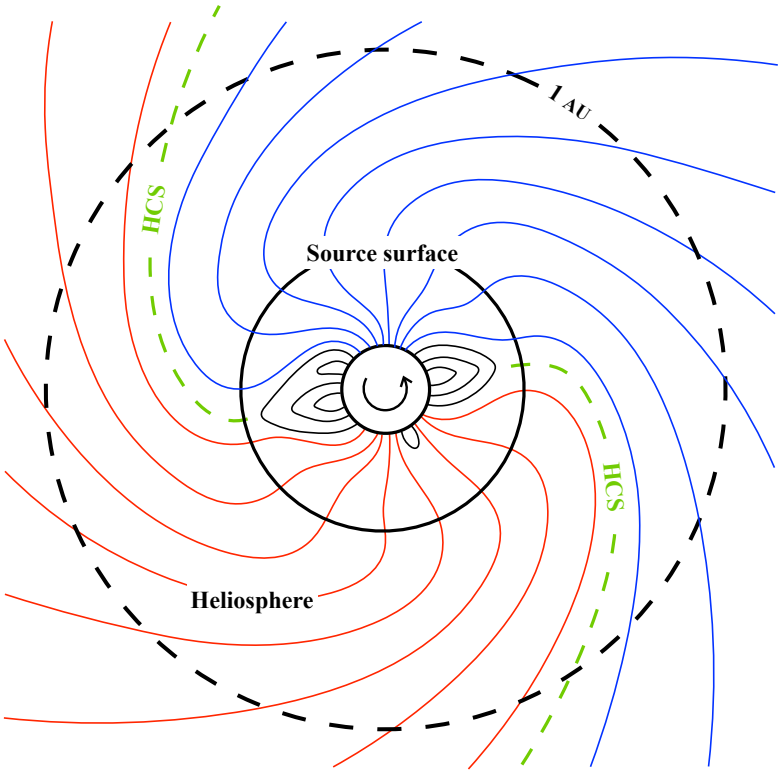

Figure 2.6: A sketch of the steady-state solar magnetic field out to 1 au in the ecliptic plane. Within the solar corona, the region close to the Sun, plasma bounded by open field lines (shown as blue and red lines) undergoes non-radial expansion with height whilst closed field lines (shown as black loops) constrain plasma to these loops. Beyond the source surface, coronal expansion occurs and the plasma flows away from the Sun radially, carrying the magnetic field with it (frozen-in theorem). The footprints of the open magnetic field lines rotate with the Sun. Combining this with the radial outflow of the solar wind causes a spiral configuration of the Heliospheric Magnetic Field. Open field lines can have either polarity, indicated by the blue and red field lines. The neural line between these is the Heliospheric Current Sheet, shown as the green dashed line. Sourced and adapted from (*Owens and Forsyth*, 2013).

region at the Sun. Therefore, due to the Sun's rotation, the HMF is characterised by an Archimedes spiral, commonly named the *Parker spiral*. Figure 2.6 illustrates the Parker spiral out to a radial distance of 1 au, where the magnetic field alignment is about 45° from the radial outflow. Beyond Earth's orbit, the HMF becomes more tightly wound with radial distance from the Sun.

This is a simplified description of the heliosphere, disregarding the complexity of differential solar rotation and varying solar activity. Based on observation at 1 au, the solar wind can be categorised by ''slow'' and ''fast'' velocity; slow solar wind varies between $300\,\mathrm{km\,s^{-1}}$ to $400\,\mathrm{km\,s^{-1}}$ and fast solar wind varies between $600\,\mathrm{km\,s^{-1}}$ to $700\,\mathrm{km\,s^{-1}}$ approximately. The solar sources of these winds are associated with the local magnetic structure. Fast winds map back to coronal holes where open magnetic fields emerged from the corona, meanwhile, slow winds map back to regions of closed magnetic field lines. The acceleration of particles during their escape from the solar atmosphere varies depending on whether the magnetic field lines are open or closed. The open field lines originating from coronal holes provide a direct route to the heliosphere, resulting in an efficient pathway that allows fast solar winds to accelerate more quickly from their source (*Stakhiv et al.*, 2016). The origin of the solar wind also has impact on other properties. Fast solar wind is not very dense ($2\,\mathrm{cm^{-3}} \leq n_p \leq 4\,\mathrm{cm^{-3}}$) and has relatively weak magnetic strength ($3\,\mathrm{nT} \leq \mid B \mid \leq 4\,\mathrm{nT}$). Conversely, slow solar wind is denser ($5\,\mathrm{cm^{-3}} \leq n_p \leq 10\,\mathrm{cm^{-3}}$), has greater magnetic intensity ($4\,\mathrm{nT} \leq \mid B \mid \leq 8\,\mathrm{nT}$) and has greater variability when observed in situ (*Owens*, 2020). Measurements of multiple properties are vital for distinguishing the solar wind type, include element composition which stays relatively consistent as the wind travels out to 1 au (*Geiss et al.*, 1995; *Owens*, 2020; *Stakhiv et al.*, 2016).

During the solar cycle the origin of the fast and slow solar wind will change in accordance to the position of coronal holes. Coronal holes are found in the Sun's polar regions during solar minimum, therefore, fast solar wind emerges from high latitudes whilst slow solar wind emerges from a constrained narrow region about ± 30° from the solar equation. At solar maximum, coronal holes are seen across all latitudes and, thus, fast and slow stream emerge from all latitudes, but slow wind dominates (*Mccomas et al.*, 1998; *Owens*, 2020).

In Section 2.1.4, the occurrence of open magnetic field lines threading a spherical

surface surround the Sun was introduced. Not only does this correspond to fast and slow solar wind, but also another feature present in the heliosphere called streamers. Open field lines will drape over closed field line as the magnetic field expands from the local source to fill the heliosphere. Magnetic field lines emerging from coronal holes will have a polarity. Regions where field lines of opposite polarity converge, known as a helmet streamer, present a neutral layer called a Heliospheric Current Sheet (HCS). Magnetic field lines of the same polarity can also converge and this is known as a pseudostreamer (*Y.-M. Wang and Jr*, 2012).

In the heliosphere, fast and slow streams of solar wind will interact. Fast solar wind stream will carry the magnetic field further into the heliosphere in comparison to the slow wind. As a result, the incident angle of the field line to the radial direction of the fast solar wind will be smaller than in slow wind streams. In addition, a fast stream will ‘‘catch up’’ to a preceding slow stream. Here, Stream Interaction Regions (SIR) occur; field lines become aligned and the solar wind is compressed.

2.4 Coronal Mass Ejections

As the structural complexity of the Sun's magnetic field increases during the solar cycle as magnetic field lines, the field lines reconfigure through a process called reconnection (Section 2.8) to reduce the ‘‘stress’’ (*Cargill et al.*, 2010; *Hesse and Cassak*, 2020; *Russell et al.*, 2015). As a result, large portions of the corona can be forced into the heliosphere upon becoming disassociated from the Sun, creating the transient events known as Coronal Mass Ejections (CME). These events travel through the heliosphere at very fast speeds, ranging from $200\,\mathrm{km\,s^{-1}}$ to $2000\,\mathrm{km\,s^{-1}}$ (*Howard*, 2014; *Moldwin*, 2016). As such, they can reach the orbital distance of Earth in a couple of days for slower events to several hours for fast events. Figure 2.7 shows a *Coronagraph* (COR) image of a CME and highlights its enormous size in comparison to the Sun (which for scale is shown by a white outline circle in the centre of the image). CMEs carry out $10^{11}\,\mathrm{kg}$ to $10^{13}\,\mathrm{kg}$ of coronal matter into the heliosphere with energy in excess of $10^{39}\,\mathrm{J}$ (*Chen*, 2011; *Howard*, 2014; *MacQueen*, 1980; *Moldwin*, 2016). These values are a significant enhancement to the ambient solar wind conditions resulting in local disturbances to the space environment, giving rise to ‘‘Space Weather’’ science. This is discussed in greater detail in Section 2.5.1.

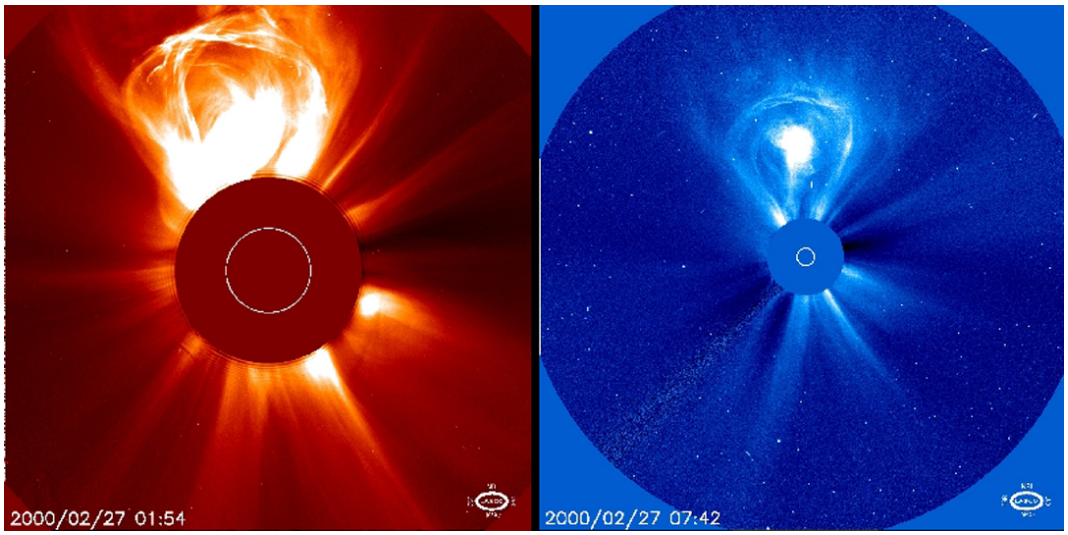

Figure 2.7: Coronal Mass Ejection (CME) on 27 February 2000 in LASCO COR-2 (left) and COR-3 (right) at 01:54 UT and 07:42 UT respectively. Comparison of the two images shows the expansion of the event into the heliosphere.

2.4.1 Magnetic Reconnection

Magnetic reconnection (also known as ‘‘reconnection’’) is the reconfiguration process of oppositely directed magnetic field lines (*Cargill et al.*, 2010; *Dungey*, 1953; *Russell et al.*, 2015). It is analysed theoretically using the fact that mass and energy are both conserved.

Between regions of oppositely directed field lines of a magnetised plasma, such as the HCS, a localised disruption to the current forms a ‘‘diffusive region’’. In this region, oppositely-directed field lines on the two sides of the boundary diffuse together and reconfigure becoming field lines that thread the current sheet. The diffusion occurs because the spatial dimension of the current sheet is small and the convective and diffusive terms in the induction equation (equation 2.1) become similar in magnitude. Therefore reconnection is a breakdown of the ideal MHD and hence also a breakdown of the frozen-in flux theorem. Newly connected field lines (Figure 2.8, green magnetic field line) are severely bent as they form a ‘‘slingshot’’ shape and, thus, apply a large magnetic tension force on the plasma encased by them. From this process, plasma is heated in the diffusive region and decoupled particles are accelerated along the current sheet away from the reconnection site. Interaction

with other plasma and waves turn the bulk accelerated flow velocities into thermal vibrations and so give heating (*Burch and Drake*, 2009; *Hesse and Cassak*, 2020).

Reconnection is a self-driven process and, therefore, believed an essential part of CME onset theories. Reconnection can occur elsewhere in the Sun-Earth system, for example, between the heliosphere and the Earth's magnetic field (discussed in Section 2.5).

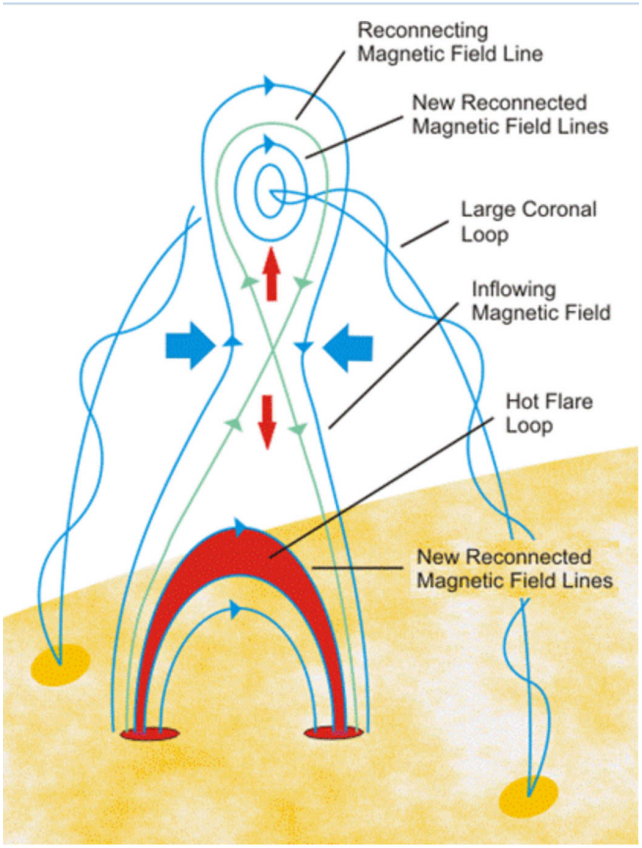

Figure 2.8: A sketch of magnetic reconnection in the solar corona that could be the onset of CME eruption. The reconnection site (where the two green field lines cross) can separate the magnetic field loop emerging from the Sun in two. The blue arrows indicate the region where the magnetic field and current are inflowing. Meanwhile, the red arrows show the direction of free electron movement after reconnection. This process drives a heating in the newly connected regions. Sourced from NASA (`https://www.nasa.gov/content/goddard/reconnection-on-the-sun`, accessed May 2023).

2.4.2 CME Initiation

The onset and initiation of CMEs is are an area of current research. Theories are focused around two stages of initiation; (1) triggers, such as magnetic breakout (*Antiochos et al.*, 1999) and flux cancellation (*Welsch*, 2006), and (2) drivers, such as kink and torus instability (e.g., *Kliem and Török*, 2006; *Kumar et al.*, 2012). An extensive review of theories, included others, can be seen in *Green et al.* (2017). Most theories involve magnetic reconnection, because it is a self-driven process, and twisted flux ropes, to provide the required energy to match CME observations (*Manchester et al.*, 2017). It is deduced that reconnection occurs below a twisted flux rope and, therefore, CMEs contain a flux rope structure out in the heliosphere (*Gosling et al.*, 1995).

Instabilities in magnetic flux ropes are believed to drive their eruption (*Kumar et al.*, 2012). Kink instabilities in flux ropes refer to multiple rotations of the flux rope that exceed a threshold ($\geq 2.5\pi$ rotations depending on the study; e.g. *Ju Jing and Wang*, 2018; *Kumar et al.*, 2012; *Török and Kliem*, 2003). Torus instabilities refers to an rapid decay of on-top perpendicular ambient magnetic field to cause the outward expansion of the flux rope (*Ju Jing and Wang*, 2018; *Kliem and Török*, 2006).

The Flux Cancellation model (*Amari et al.*, 2007; *Welsch*, 2006; *Yardley et al.*, 2018) suggests that the equilibrium of magnetic sheer across a current sheet, which keeps filament material constrained near the Sun, is lost at a reconnection site. As a result, the flux rope moves radially away from the Sun until a new equilibrium is achieved. Eventually, the solar wind acts to pull the flux rope anti-sunward. An extension from this is the Breakout model (*Antiochos et al.*, 1999; *B. J. Lynch and Fisk*, 2004; *MacNeice et al.*, 2004) which suggests the balance between the (upwards) magnetic pressure force and the (downwards) tension force is important to CME initiation. Magnetic reconnection occurring ahead of the filament allows it to move further from the Sun. As the filament expands further from the Sun, a current sheet forms behind it. Here, reconnection occurs and the flux rope becomes disassociated from the Sun.

It is likely several onset theories occur for CMEs to erupt into the heliosphere,

either simultaneously or in quick succession (*Green et al.*, 2017). Numerical models have be created to simulate coronal loop regions to theorise the details of CME initiation.

2.4.3 Kinematics

The solar wind structure into which a CME is ejected and the CME's initial speed will influence CME kinematics between the Sun and the Earth. Generally speaking, the CME will accelerate/decelerate to adjust to the ambient conditions (*Gosling et al.*, 1990; *Lin and Chen*, 2022). For a "fast" CME ($> 1000\,\mathrm{km\,s^{-1}}$), rapid acceleration to the peak speed occurs up to $15\,R_\odot$ followed by a quick deceleration to $50\,R_\odot$ where a near-constant speed is obtained for the remainder of the propagation. For an "intermediate" CME ($400\,\mathrm{km\,s^{-1}}$ to $1000\,\mathrm{km\,s^{-1}}$), a similar but extended trend is seen whereby acceleration occurs out to $20\,R_\odot$ and deceleration occurs to $85\,R_\odot$ after which the CME travels with constant speed. In the case where the CME initial speed is slower ($< 400\,\mathrm{km\,s^{-1}}$) than the ambient solar wind, a so-called "slow" CME, the CME will accelerate to meet the ambient conditions over $25\,R_\odot$ to $30\,R_\odot$ and continue thereafter with constant speed. The mechanism causing the deceleration/acceleration of the CME to converge with the ambient solar wind speed is called the aerodynamic drag (*Gopalswamy et al.*, 2000). From the characterisation of the speed profiles, it is clear that the mechanism causing the initial acceleration of fast and intermediate CMEs is not due to coupling with the solar wind but rather due to an imbalance of forces in the lower corona that drives the CME away from the Sun *Lin and Chen* (2022). A driving force of a CME is provided by the Lorentz force and acceleration due to gravity (*Cargill*, 2004; *Vršnak*, 2006).

The Lorentz force, F_L, is the exerted force on an electric charge, q, moving through an electromagnetic environment:

$$\boldsymbol{F}_L = q(\boldsymbol{E} + \boldsymbol{V} \times \boldsymbol{B}) \tag{2.20}$$

where E is the electric field, V is the velocity, and B is the magnetic field. This force is experienced by all the particles that are frozen in to the magnetic flux rope of a CME. It's been demonstrated that the Lorentz force becomes less influential with radial distance as the CME expands (*Vršnak*, 2006; *Vršnak et al.*, 2004). Therefore, aerodynamic drag in turn is more dominant in CME propagation through

the heliosphere. The Lorentz force can have a longer influence on heavier CMEs (*Vršnak et al.*, 2008) to distances as great as $100\,R_{\odot}$ ($\approx 50\,\%$ of the Earth distance; *Temmer et al.*, 2011).

2.4.4 Structure

In general, CMEs are observed to be relatively symmetrical and geometrical simple curved shapes near the Sun, as the magnetic pressure and curvature forces constrain them. The shape constraints remain whilst the solar wind is in sub-Alfvénic conditions. Beyond the Critical Point, the CME plasma is moving with Alfvénic velocity and begins to move independently from neighbouring plasma. As a result, the CME

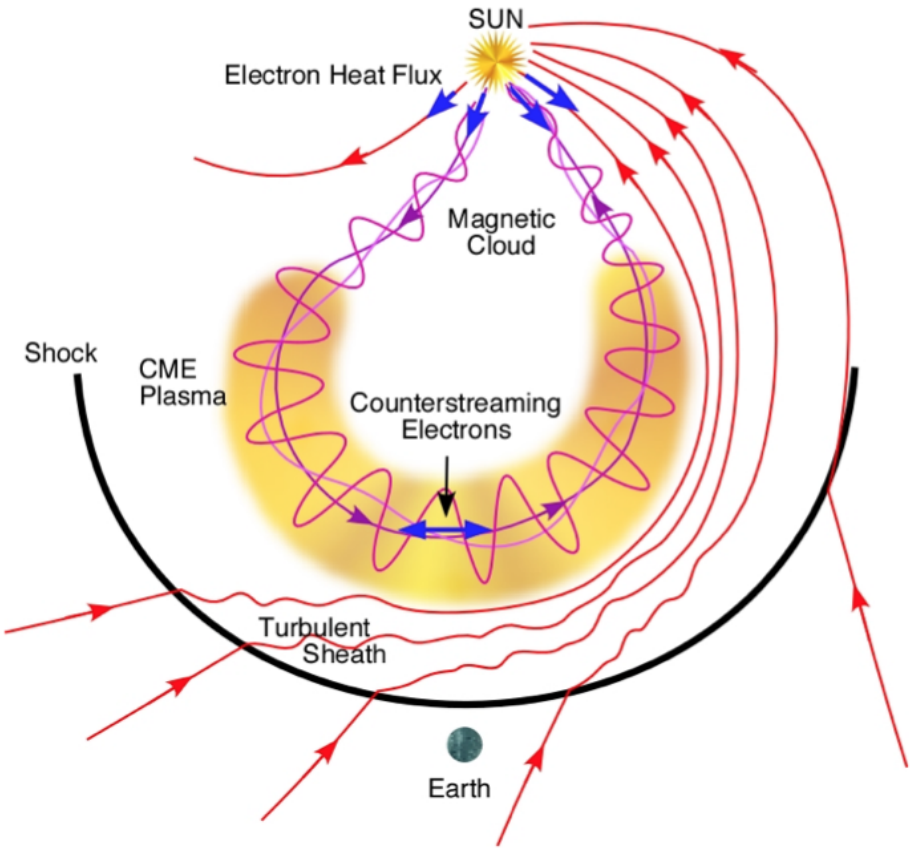

Figure 2.9: Sketch of the idealised Coronal Mass Ejection structure and the leading shock (bold black curve). Magnetic field lines are shown in red; some of these are from the Heliospheric Magnetic Field and others are within the magnetic flux rope. A large density of plasma is bounded to the leading front of the flux rope as indicated by the yellow "C" shape. Sourced from *Zurbuchen and Richardson* (2006).

becomes coupled with the solar wind and morphs with respect to the ambient conditions. Thus, CMEs become distorted from initial shape. As will become apparent later in this thesis, the complexity of CMEs in the heliosphere is an area of current research (e.g., *Jones et al.*, 2020).

CMEs have a number of common structural features, sketched in Figure 2.9. A magnetic cloud forms the core of a CME encased by a leading loop. These regions have stronger magnetic field and higher ion density, making them brighter in images. Between the two, a cavity can be seen. This is the ''classic'' three-part structure of a CME (*Illing and Hundhausen*, 1985). In situations where the CME speed is significantly greater than the solar wind, a faint shock wave can be seen ahead of the leading loop which can generate and drive energetic particles through collision with the solar wind. The region between the shock front and the leading loop is called the sheath where the solar wind conditions are turbulent.

In situ Signatures

Before the launch of *Solar-TErrestrial RElations Observatory* (STEREO) mission in 2006, CMEs were only seen close to the Sun and at Earth 1.50×10^8 km from the Sun (or 1 au). Throughout this distance, CMEs undergo distortion and CME characteristics are observed to be different in near Earth space compared with what was seen as the event left the solar corona (*Deforest et al.*, 2012). As a result, much literature specifies Earth-impacting CMEs as *interplanetary coronal mass ejections* (ICME) for clarity. Since the launch of STEREO, the understanding of the CME trajectory has advanced, as this thesis will go on to discuss, and the ICME term is used less frequently in recent publications.

When a spacecraft encounters a CME, characteristic signatures can be seen in measurements of the in-situ magnetic field, plasma dynamics, and plasma composition. These can be used to confirm the passage of the CME over the spacecraft. An extensive discussion of this is found in the literature (e.g. *Klein and Burlaga*, 1982; *Zurbuchen and Richardson*, 2006), and are summarised here in Table 2.1. These signatures identify a different three-part structure - a shock front, turbulent sheath, and a magnetic cloud - although there are similarities. The most reliable signatures are associated with changes in the magnetic field, indicating the arrival of the

Table 2.1: Summary of the 1 au in-situ signatures that are associated with an interplanetary CME. These signatures are separated into five categories; the Magnetic Field (B), Plasma Dynamics (P), Plasma Composition (C), Plasma Waves (W), and Suprathermal Particles (S). A CME that reaches 1 au will not necessarily have all these signatures, but a combination of these are expected. Sourced from *Zurbuchen and Richardson* (2006).

Signature	**Description**
B1: B Rotation	$\gg 30°$
B2: B Enhancement	$> 10\,\mathrm{nT}$
B3: B Variance Decrease	
B4: Discontinuity at ICME boundaries	
B5: Field line draping around ICME	
B6: Magnetic clouds	B1, B2, and $\beta < 1$
P1: Declining Velocity Profile/Expansion	Monotonic Decrease
P2: Extreme Density Decrease	$\leq 1\,\mathrm{cm}^{-3}$
P3: Proton Temperature Decrease	$T_p < 0.5 T_{exp}$
P4: Electron Temperature Decrease	$T_e < 6 \times 10^4\,\mathrm{K}$
P5: Electron Temperature Increase	$T_e \gg T_p$
P6: Upstream Forward Shock/"Bow Wave"	
C1: Enhanced α/Proton Ratio	
C2: Elevated Oxygen Charge States	
C3: Unusually High Fe Charge States	
C4: Occurrence of He^+	
C5: Enhancements of Fe/O	
C6: Unusually High $^3He/^4He$	
W1: Ion Acoustic Waves	
S1: Bidirectional Strahl Electrons	
S2: Bidirectional ~MeV Ions	
S3: Cosmic Ray Depletions	
S4: Bidirectional Cosmic Rays	

magnetic cloud. These include a large rotation and sudden enhancement to the magnetic field, reduced small-scale variability in the magnetic field measurements, low plasma beta, and a reduction in proton temperatures. When the magnetic field of the CME has a southward component, this can lead to high-intensity geomagnetic activity at Earth, which is discussed in more detail in Section 2.5.1 (*Cane and Richardson*, 2000; *Mundra et al.*, 2021; *Tsurutani and Lakhina*, 1997). However, only a small subset of interplanetary CMEs (around 30 %) show the signature of a magnetic cloud (*Gosling et al.*, 1990; *Owens et al.*, 2017; *Zurbuchen and Richardson*, 2006). Thus, examining in-situ measurements for multiple signatures is best practice (*Zurbuchen and Richardson*, 2006). The shock can be associated with a rapid enhancement in solar wind velocity. Following this, the turbulent sheath corresponds to disturbances in the measurement profiles. In the case where shocks are not formed ahead of the CME, the speed enhancement may correspond to the leading edge instead. The presence of a magnetic cloud in the in-situ data enables confirmation that the enhanced velocity signature is a CME feature and not a localised fast stream in the solar wind.

2.5 Magnetic Interactions with Earth

Earth, like many planets, has a magnetic field that protects the planet from solar wind and energetic particles. The magnetic dipole creates a low-density, high-field cavity within the HMF called the magnetosphere, shown in Figure 2.10. On the dayside, the magnetosphere is compressed as a result of the solar wind pressure. Between the two magnetic fields, a thin current sheet between the solar wind and Earth's magnetic fields, called the magnetopause. If ideal MHD always applied the solar wind would be frozen-in to the HMF and the magnetospheric plasma would be frozen in to the geomagnetic field and the magnetopause would form an impermeable barrier between the two. However, in the situation where there is a large magnetic shear between the two magnetic fields, due to a southward IMF in comparison to Earth's northward IMF, dayside magnetic reconnection will occur (*Koga et al.*, 2019; *Tsurutani and Lakhina*, 1997). Consequently, open field lines between the HMF and Earth's magnetosphere (threaded through the magnetopause) will allow solar wind plasma to flow into the magnetosphere. These open field lines continue to be frozen

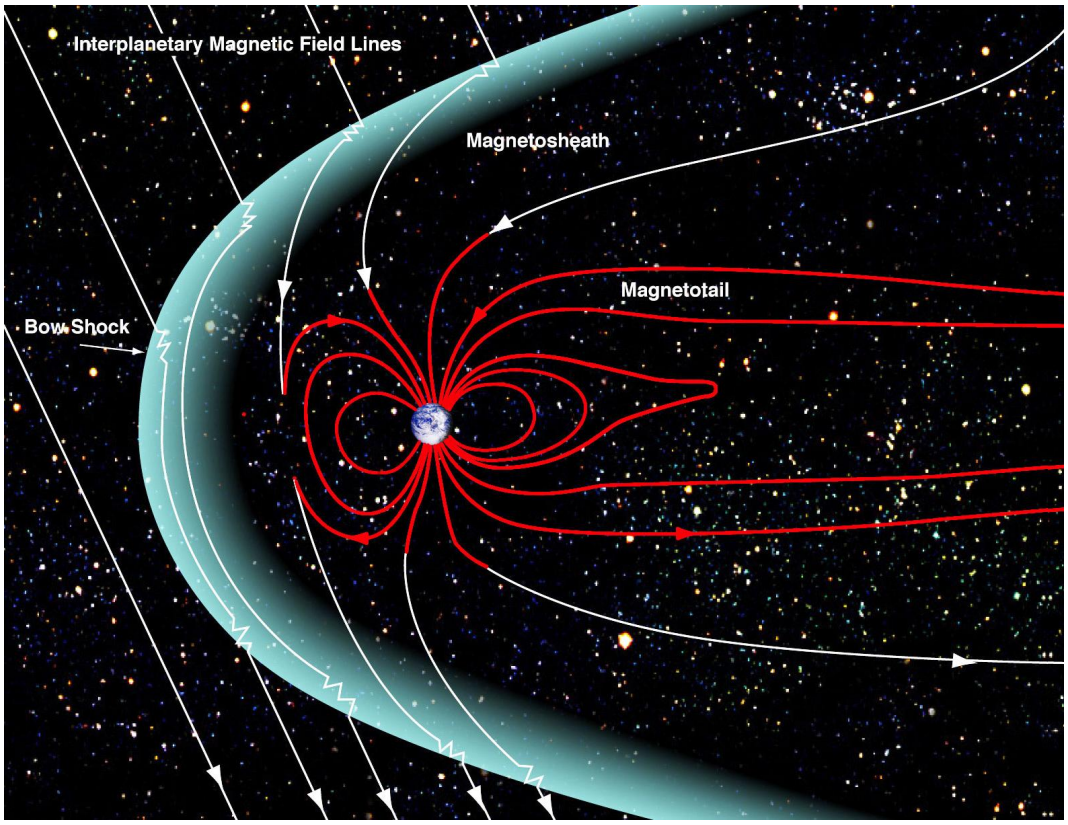

Figure 2.10: Diagram of Earth's magnetic field structure within the Heliospheric Magnetic Field. Sourced from NASA (`https://www.nasa.gov/mission_pages/sunearth/multimedia/magnetosphere.html`, accessed May 2023).

in flux, thus, as the solar wind continues to travel anti-sunward, the open field lines are dragged towards the nightside of the magnetosphere and form the extended tail anti-sunward from Earth. Enhanced energy circulates within the magnetosphere and is stored in the tail. Magnetic (nightside) reconnection then occurs in the tail current sheet (neutral boundary), releasing bursts of energy away from Earth, in events known as sub-storms, and reconnected field lines travel back to the dayside magnetosphere. This cycle is called magnetospheric convection, or the *Dungey Cycle*, and is important for space weather because it is the driver of geomagnetic activity and space weather disturbances in the terrestrial space environment.

When sub-storms are initiated, some of the stored energy in the magnetospheric tail is forced toward Earth where electric currents are induced in the ionosphere at high latitudes. The ionosphere is the ionized upper atmosphere at altitudes between about 80 and 800 km. It is different from the magnetosphere because the ionization

is much lower concentration than neutral atmospheric atoms/molecules at the same height, called the themosphere, and collisions between the ion and electrons and the neutral thermospheric particles generate field-perpendicular conductivties. These allow currents that flow along field lines in the magnetosphere to close and form large scale circuit loops. They also generate magnetic deflections on the ground ("geomagnetic activity") and heat the upper atmosphere. During severe space weather, electric currents are also induced in mid-latitude ionosphere regions. At such times, the aurora can be seen at lower latitudes than normal. In addition, charged particles are injected into the Earth's ring current (an electric current about the Earth's equator). This current induces changes in the surface geomagnetic field and drives Geomagnetically Induced Current (GIC). Prolonged periods of geomagnetic activity are called geomagnetic storms.

2.5.1 Space Weather Hazards

Space weather is the term that describes variations in the near-Earth environment (including the magnetosphere, ionosphere, and thermosphere) which can impact technology and cause a detrimental social-economical impact on Earth (*Cannon*, 2013; *Hapgood and Thomson*, 2018; *Koons et al.*, 1999). Geomagnetic activity is one of the natural impacts of solar activity seen on Earth, driven by CMEs, high-speed streams, and Stream Interaction Regions (SIR). Solar flares and Solar Energetic Particles (SEPs) will also cause an impact on humankind's operational systems on Earth. As a result, reduced performance of satellites, transport (rail and aviation), power grids, as well as radiation exposure are examples of how human lives can be negatively impacted by space weather. Figure 2.11 shows the vast range of topics covered by space weather research. Since the focus of this thesis is CME, some of the space weather impacts associated with CMEs are described below.

1. **Satellites**

   Earth-orbiting satellites are vital for communication and navigation technologies. Due to their orbit high above the Earth's surface, they are susceptible to a high level of space weather effects; for example, surface charging (*Mazur et al.*, 2012), internal charging (*Lohmeyer et al.*, 2015), single event effects (*Sedares et al.*, 2016), and ionising dosage (*Hands et al.*, 2018). As a result, satellites

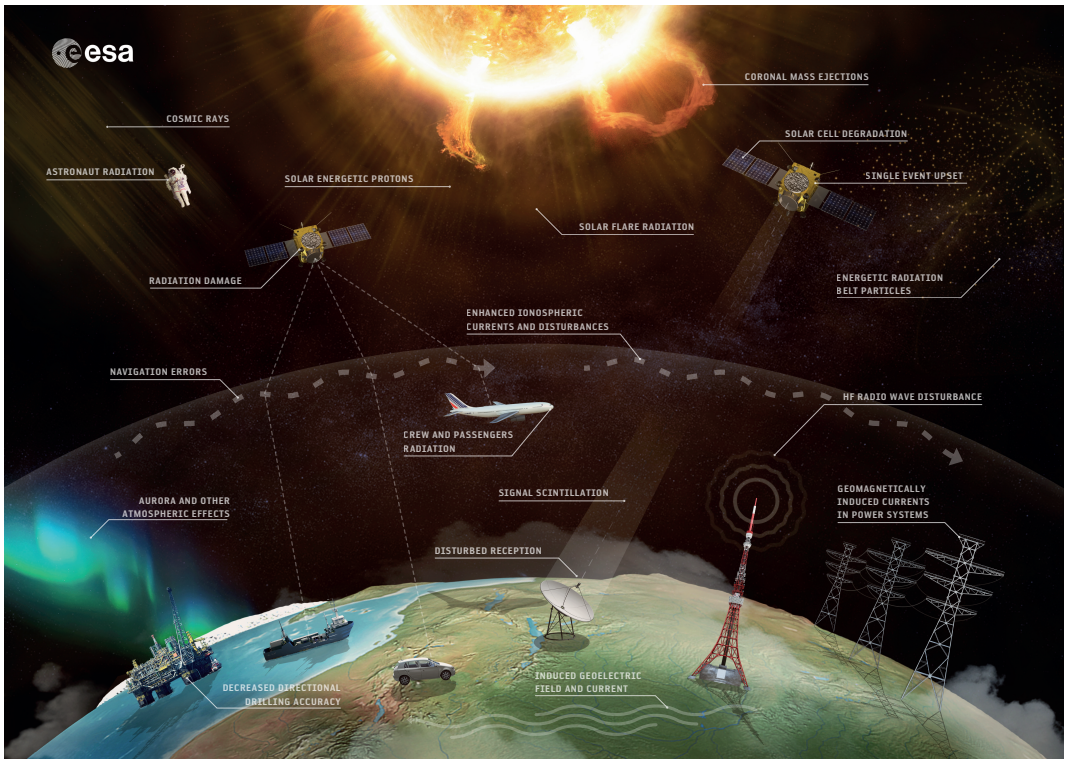

Figure 2.11: Illustration of the broad range of natural phenomena and technologies on Earth that can be impacted by severe space weather events. These impacts occur to technologies over a great height, from ground-based to technologies within the near-Earth environment. Sourced from *European Space Agency* (2018).

can experience high voltages, electrical interference or breakdown, instrument degradation, and hidden damages leading to satellite failure (*Green et al.*, 2017; *Hands et al.*, 2018; *Lohmeyer et al.*, 2015; *Mazur et al.*, 2012; *Sedares et al.*, 2016). Consequently, there can be significant impacts on businesses requiring satellite services, such as communications, broadcast, and navigation. Drilling rigs require a very high level of positional accuracy, thus, errors in navigation can be significant (*Reay et al.*, 2005; *Thomson et al.*, 2011) and temporarily halt operations, as was the case for a Canadian company earlier this year (*Pultarova*, 2023).

2. **Electrical infrastructure**

   Electrical infrastructure is also susceptible to space weather, such as transformer damage and the resulting loss of power from additional strong currents induced

on the power grid. As a result of malfunctioning electrical infrastructure, there would be sequential effects on society as the power supply is reduced/lost. For example, communications, sanitation, and healthcare (*Hapgood and Thomson*, 2018; *Thomson et al.*, 2010). In the geomagnetic storm of 1989, Quebec experienced widespread blackouts for 9 hours due to electric transmission grid failures. It took several months for the transmission grid was back in full operation after $6.5 million of damage to the electrical infrastructure. The reliance on electrical power in society contributed to a minimum net economic impact of $13.2 million as a result of the geomagnetic storm (*Bolduc*, 2002; *Oughton et al.*, 2017). In the event of an extreme CME occurring today, the United Kingdom or the USA alone could face a staggering multi-billion-dollar economic impact *Oughton et al.* (2017, 2019).

3. **Transport**

   On the railway, detrimental effects to the infrastructure and operation systems will occur during space weather events (*Krausmann et al.*, 2015). As a result of GICs, there are increased reports of signal failures which can lead to collision risks (*Boteler*, 2021). Currents in the overhead line equipment can also be significant to electrical train operations as trains can be forced to halt from overheating and railway maintenance is suspended (*Hapgood et al.*, 2021). As a consequence of navigation malfunctions during the space weather event, trains can be significantly delayed due to their reliance on the precision of train positions to maintain safety protocols. Interconnectivity of these issues would be most problematic for railway services (*Hapgood et al.*, 2021)

   There are different issues for aircraft transport. As for spacecraft electronics, avionics systems need to be resilient to energetic particle effects. In addition, the particles pose a potential health hazard for aircraft crew and frequent fliers particular for the latest aircraft that cruise at higher altitudes and for transpolar flight paths.

Space weather has become an acknowledged risk in the last decade. Following the severe disruption of the UK airspace in 2010 caused by an Icelandic volcanic eruption and the consequential socio-economic impacts, the UK Government reassessed their

risk register to better prepare for potential hazards. This was completed by assessing ‘‘reasonable’’ worst-case scenarios (*Department for Business, Innovation and Skills*, 2021; *Hapgood et al.*, 2021). Thus, space weather is now considered a mid-risk and mid-likelihood hazard within the UK (*Department for Business, Innovation and Skills*, 2021) and daily monitoring of the space weather conditions is part of the UK Met Office forecasting routine (*Sharpe and Murray*, 2017).

Chapter 3

Observing Coronal Mass Ejections

3.1 Observational Space Missions

Coronal Mass Ejection (CME) are large-scale eruptions of solar plasma and magnetic field from the solar atmosphere that travel out through the heliosphere. Since the discovery of CMEs (first spacecraft observation reported by *Tousey*, 1973) and their effect on Earth (*Gosling*, 1993), several space missions have been commissioned to advance our knowledge of these transient events. Here, we discuss in greater detail the two missions which provide us with data used to carry out the research in this thesis.

3.1.1 The Advanced Composition Explorer (ACE)

On 25 August 1997, NASA launched their Advanced Composition Explorer (ACE) mission; a single spacecraft mission designed to measure the solar wind, particularly the ion charge state and composition in order to better understand solar wind origins (*Stone et al.*, 1998). With nine instruments on board, solar, interstellar and galactic matter could be studied. With an initial mission span of 2 years, ACE

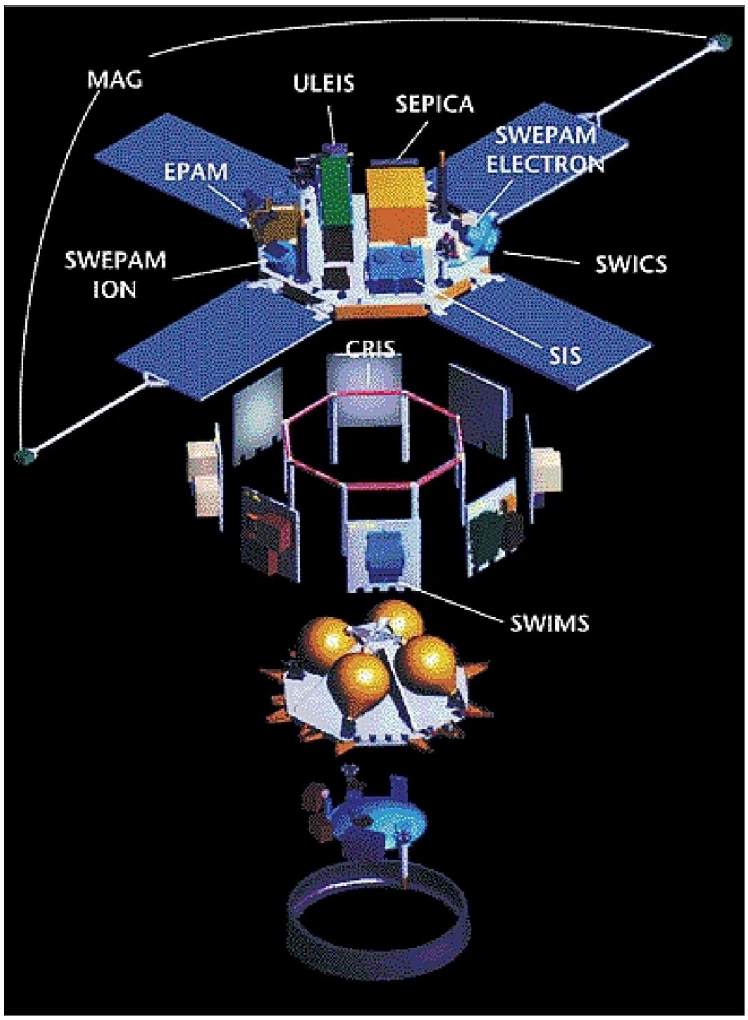

Figure 3.1: Expanded view of NASA's *Advanced Composition Explorer* (ACE) spacecraft structure, with the onboard instruments labelled. The *Solar Wind Electron, Proton, and Alpha Monitor* (SWEPAM) package records solar wind measurements. Sourced from *Stone et al.* (1998).

continues to collect data today. The instruments on ACE are the Solar Wind Ion Mass Spectrometer (SWIMS); Solar Wind Ion Composition Spectrometer (SWICS); Ultra-Low Energy Isotope Spectrometer (ULEIS); Solar Energetic Particle Ionic Charge Analyzer (SEPICA); Solar Isotope Spectrometer (SIS); Cosmic Ray Isotope Spectrometer (CRIS); Solar Wind Electron, Proton, and Alpha Monitor (SWEPAM); Electron, Proton, and Alpha-Particle Monitor (EPAM); MAGnetometer (MAG); and Real Time Solar Wind experiment (RTSW). The structure of the ACE spacecraft is shown in Figure 3.1.

Situated at the L1 Lagrange Point in a halo orbit, ACE is able to observe the composition of the solar wind, CMEs and Solar Energetic Particles (SEPs); a useful data set for space weather monitoring. The SWEPAM experiment records the majority of solar wind measurements in three dimensions, producing characterisation of bulk flow (*Mccomas et al.*, 1998). Near-real-time measurements of solar wind parameters are fed to National Oceanic and Atmospheric Administration (NOAA) to produce space weather forecasts. This data includes solar wind velocity, density, and temperature from SWEPAM; magnetic field vector from MAG; and energetic particle fluxes from EPAM and SIS. Today, 25 years since the operations began, ACE continues to provide us with valuable data about the solar wind.

3.1.2 The Solar-TErrestrial RElations Observatory (STEREO)

On 26 October 2006, NASA launched their *Solar-TErrestrial RElations Observatory* (STEREO) mission which aimed to "*understand the origin and consequence of CMEs*" (*Kaiser et al.*, 2008). The mission is formed of two spacecraft in heliocentric orbits; STEREO-A orbits ahead of Earth at an average radial distance 0.96 au whilst STEREO-B is orbiting behind at 1.03 au. With each full orbit of the Sun, both spacecraft increasingly separate from the Earth by approximately 22° in ecliptic longitude. Thus, throughout its lifetime, it has collected data from a variety of positions relative to the Sun-Earth line from where the true propagation speed of the CME can be estimated with greater accuracy. Previous missions, such as NASA's Solar and Heliospheric Observatory (SOHO), only provided a single point view of the Sun and its transients, as restricted entirely to viewing from the Earth-Sun line. Consequently, the geometry of Earth-directed CME identification was not

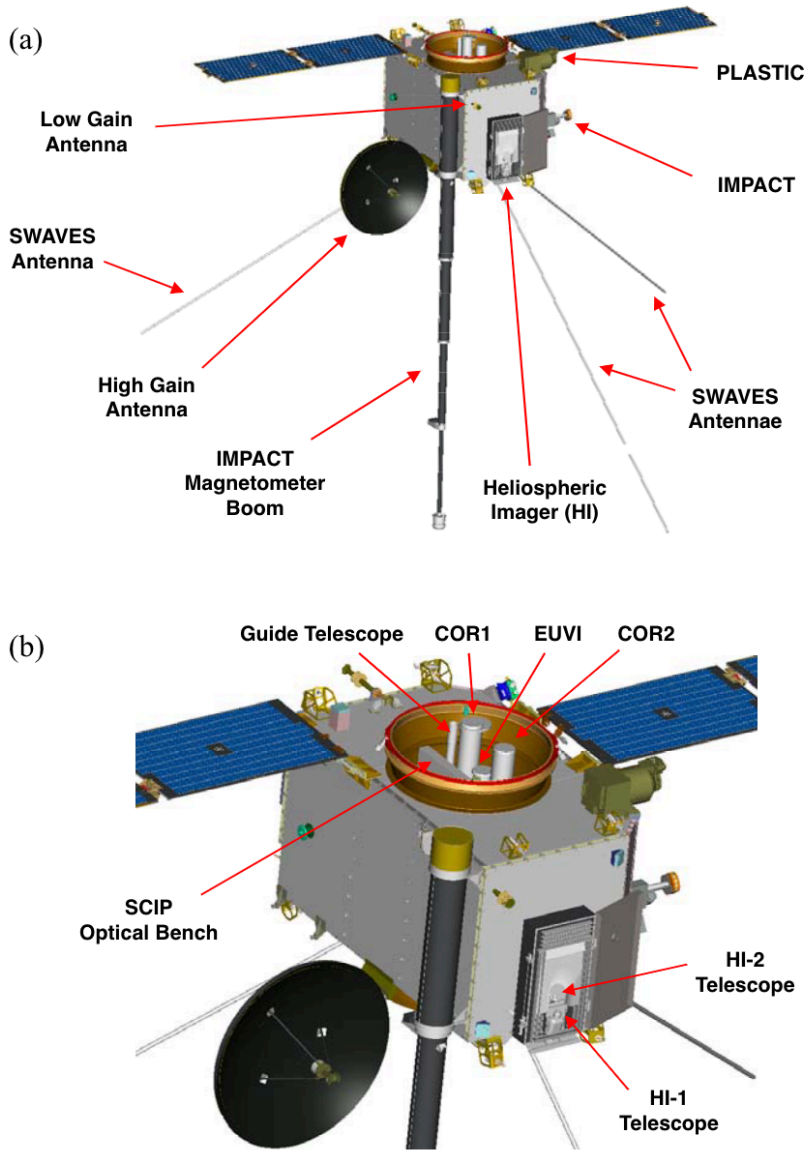

Figure 3.2: Schematic of the *Solar-TErrestrial RElations Observatory* (STEREO) spacecraft. An overview is shown in (a), detailing the position of all the instruments onboard. The *Sun-Earth Connection Coronal and Heliospheric Investigation* (SECCHI) package is shown in more detail in (b). The *Heliospheric Imager* (HI) instrument mounted on the side of one of the STEREO spacecraft is encased within a baffle box. The *Coronagraph* (COR) and *Extreme UltraViolet Imager* (EUVI) instruments are located at the top of the spacecraft. The other instruments of the STEREO satellites' payload are described in the text. Sourced and adapted from *Eyles et al.* (2009).

optimum, either ineffectively measuring the velocity and shape of events or observing the CME as a ''halo'' event (*Eyles et al.*, 2009; *Kaiser et al.*, 2008). It is especially challenging to determine the true speed and direction of a CME due to the nature of the observation which relies on Thomson scatter of sunlight by free electrons in the CME plasma. The STEREO mission was designed to develop our understanding of the causes and mechanisms of CME initiation, characterise the propagation of CMEs through the heliosphere, and discover the mechanisms and sites of solar energetic particle acceleration in the low corona and the interplanetary medium. This information would help improve MHD numerical models of the heliosphere (*Kaiser et al.*, 2008).

Both STEREO spacecraft carry four identical instrument packages which image and make in-situ measurements of plasma and magnetic fields. The *Sun-Earth Connection Coronal and Heliospheric Investigation* (SECCHI) instrument suite contains remote sensing instruments designed to study the evolution of CMEs from the Sun's surface out to Earth's orbit. These instruments are the two white-light *Coronagraph* (COR), *Heliospheric Imager* (HI), and *Extreme UltraViolet Imager* (EUVI), and can be seen labelled on the STEREO schematic in Figure 3.2a. COR1 and COR2 observe plasma from $1.4\,R_\odot$ to $4.0\,R_\odot$ and $2.0\,R_\odot$ to $15.0\,R_\odot$ respectively whilst the HI package cover heliospheric space from $12.0\,R_\odot$ to beyond Earth's orbit at $215.0\,R_\odot$. The EUVI package observes four spectral emission lines (of helium and iron) in the heliosphere and low corona (*Wuelser et al.*, 2004). The *In situ Measurements of PArticles and CME Transients* (IMPACT) instrument measures interplanetary magnetic field, thermal and suprathermal solar wind elections, and energetic electrons and ions. The *PLAsma and SupraThermal Ion Composition* (PLASTIC) instrument produces diagnostic measurements of protons, alpha particles and heavy ions so that the plasma can be characterised as coming from CMEs or from the ambient coronal plasma (*Galvin et al.*, 2008). Finally, *STEREO/WAVES* (S/WAVES) is an interplanetary radio burst tracker, observing radio disturbances from the Sun (*Bougeret et al.*, 2008).

The STEREO mission had a nominal lifetime of two years. This was achieved and STEREO-A remains in working condition at the time of writing. Contact with STEREO-B was lost on 1 October 2014, when it went behind the Sun. During

the initial two-year mission, STEREO was expected to observe at least 150 CMEs. However, the SECCHI instrument recorded more than 60 events during the first 150 days of the mission and many more have been observed since.

3.2 Heliospheric Imager

The HI is part of STEREO's SECCHI instrument package, along with white-light COR and EUVI, designed to study CME evolution in three dimensions. Encased in the HI instrument are two cameras, situated so they can observe the heliosphere from 4.0° – 88.7° angular elongation from the Sun's centre (Figure 3.3). Along the ecliptic, this field of view spans from approximately 15 $R_\odot$ to 330 $R_\odot$ in the plane of the sky, allowing observations of CMEs from near-Sun to beyond the Earth's orbit. Exposing

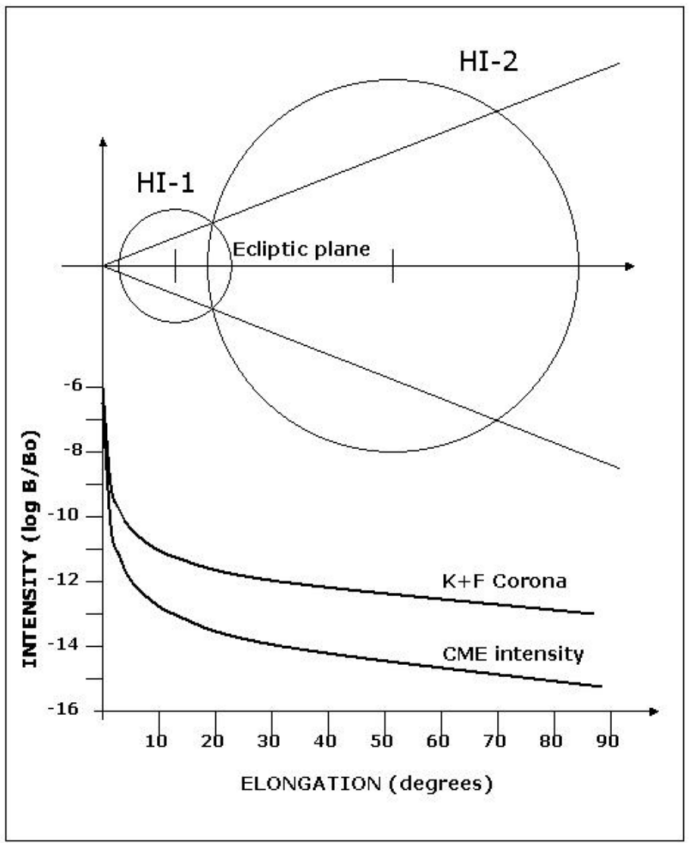

Figure 3.3: The *Heliospheric Imager* (HI) field-of-view as a function of elongation angle. The anticipated intensities of light scattered by the corona and typical CMEs are shown as well. Sourced from *Eyles et al.* (2009).

the detector to too much light can saturate pixels within the detector even to such an extent that entire images appear washed out. HI cameras are also susceptible to this with extremely bright light from the Sun, as well as stray light from planets, stars, and zodiacal lights (*Eyles et al.*, 2009). Housed within a specifically designed baffle box attenuates unwanted light signals, discussed in more detail below (Section 3.2.1). Unlike most cameras, the Heliospheric Imagers are shutter-less, and thus, image pixels are subjected to uneven exposure. This can be compensated for in image post-processing, discussed in more detail below (Section 3.2.2).

3.2.1 Baffle Design

To reduce stray light sources and allow faint solar wind transients to be imaged, the HI cameras are situated within a system designed to scatter and absorb unwanted light with three baffles – forward, internal, and perimeter. These three baffle systems can be seen in Figure 3.4. Since the position and intensity of each source can vary, the baffles are designed to each combat a particular stray light source.

The forward baffle is designed to reject the greatest intensity; light from the solar disc. Using a knife-edge cascade system, seen in Figure 3.5, a series of vanes in descending height casts a shadow on the instrument's detector plane. Light

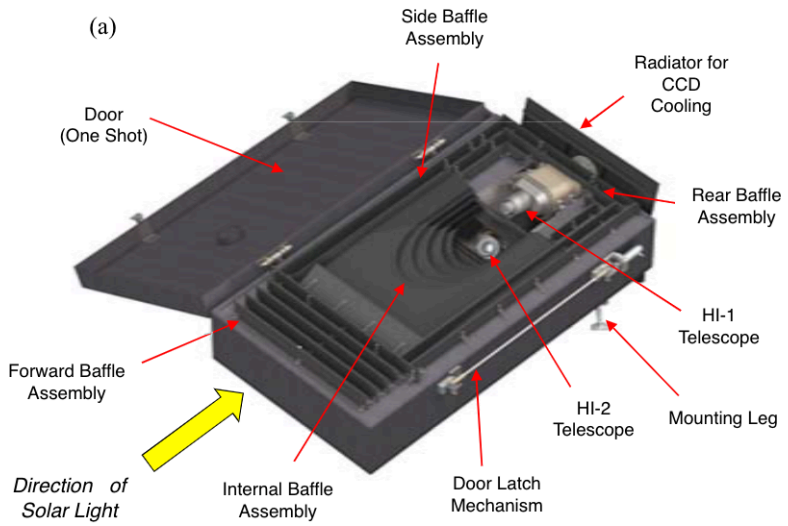

Figure 3.4: The *Heliospheric Imager* (HI) baffle box, detailing the internal structure to diminish unwanted light signal and the position of the two HI cameras. Sourced from *Eyles et al.* (2009).

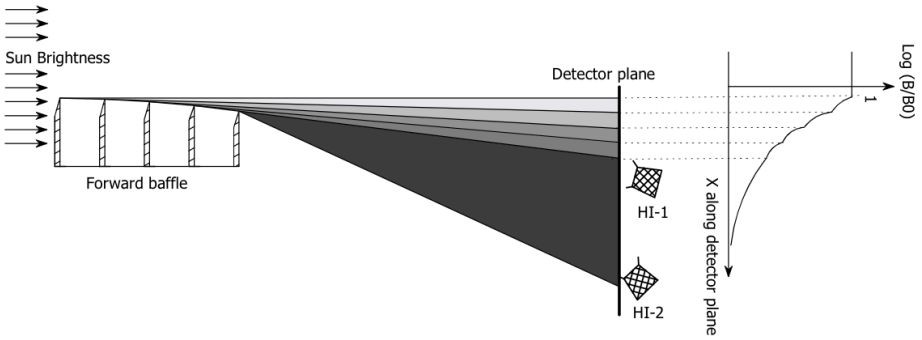

Figure 3.5: A schematic of the forward baffle system within the *Heliospheric Imager* (HI) baffle box. This is a cascade knife-edge diffraction system, resulting in less light entering the HI1 and HI2 cameras. This rejection factor of light is plotted on the right. Sourced from *Eyles et al.* (2009).

entering the forward baffle is diffracted around each vane, reducing the light intensity reaching the successive vane. The light-mitigating contributions of the successive vanes increase the rejection factor of light as you go deeper into the system, where the baffle horizon is the height of the initial shadow cast. Despite the Sun being outside the field of view, five vanes are required to achieve suitable rejection factors for the HI cameras.

The varying position of Earth in relation to the STEREO spacecraft throughout the mission has led to the design of the internal baffle to reduce light intensity through multiple reflections within the system. As a result, stray light intensity from the Earth, other planets, stars, F-corona and the S/WAVES antenna is reduced by a factor $\geq 10^4$.

Light from objects lying below the baffle horizon can also be internally reflected within the instrument from the HI door mechanism for example, despite the light-absorbing black paint which coats the baffles. The perimeter baffle is designed to protect against this source of stray light.

By design of the baffle box, the stray-light level is at least an order of magnitude lower than the intensity of the coronal signal (Figure 3.3), and with image processing the intensity of the CME signal can be determined.

3.2.2 Image Processing

HI images are made available at different ''levels'', depending on the amount of processing they have undergone. Level 0 represents a raw image, in which the signal is dominated by the F-corona (light scattered from dust particles which has a spectrum that includes Fraunhofer absorption lines, hence the letter ''F'') and has not had any calibration applied to the image. A Level 1 image has undergone the ''SECCHI_PREP'' process, mentioned earlier to compensate for HI's shutterless camera. Within this step, several corrections are applied. Firstly, as the pixels of the camera are read row-by-row starting with the base of the image, the top row is subjected to a greater exposure to light. By acknowledging additional time of exposure, a correction is applied to correct this bias. Secondly, the HI camera optics cause vignetting - a variation in the image's brightness whereby the image's outer edge is darker compared to the image center. A flat-field correction is applied based on the known brightness of the star field. This can also correct sensitivity variation between individual pixels. Finally, the accuracy of the camera pointing direction can be improved from the known locations of the star field. In Level 2 images, the F-corona (which makes up $> 99\,\%$ of the image signal) is removed. The F-corona, and the camera's thermal noise, can be characterised by the minimum signal in a pixel over a sequence of images since any passing transients make a temporary signal enhancement. By averaging the minimum signal over a period of time (e.g., 1 day for HI1 and 11 days for HI2 images) and subtracting this from the image, transient events, stars and planetary bodies are easier to identify. (*Eyles et al.*, 2009). For observing transient events, Level 2 image processing removes *blooming* - an over-spill of enhanced light signals from planets. The HI detector has a waffle-like structure with raised dividers that are enhanced in the vertical plane causing the blooming to appear as false bright vertical lines. With the F-corona ''Background'' subtracted, plasma densities associated with CME are seen more easily (*Eyles et al.*, 2009). These stages if image processing can be seen in Figure 3.6.

There is an alternate method to image processing by which subtracting sequential HI images will remove unwanted signals from non-transient sources, a quick and easy method argued to be best for seeing radial movement in transient events. This

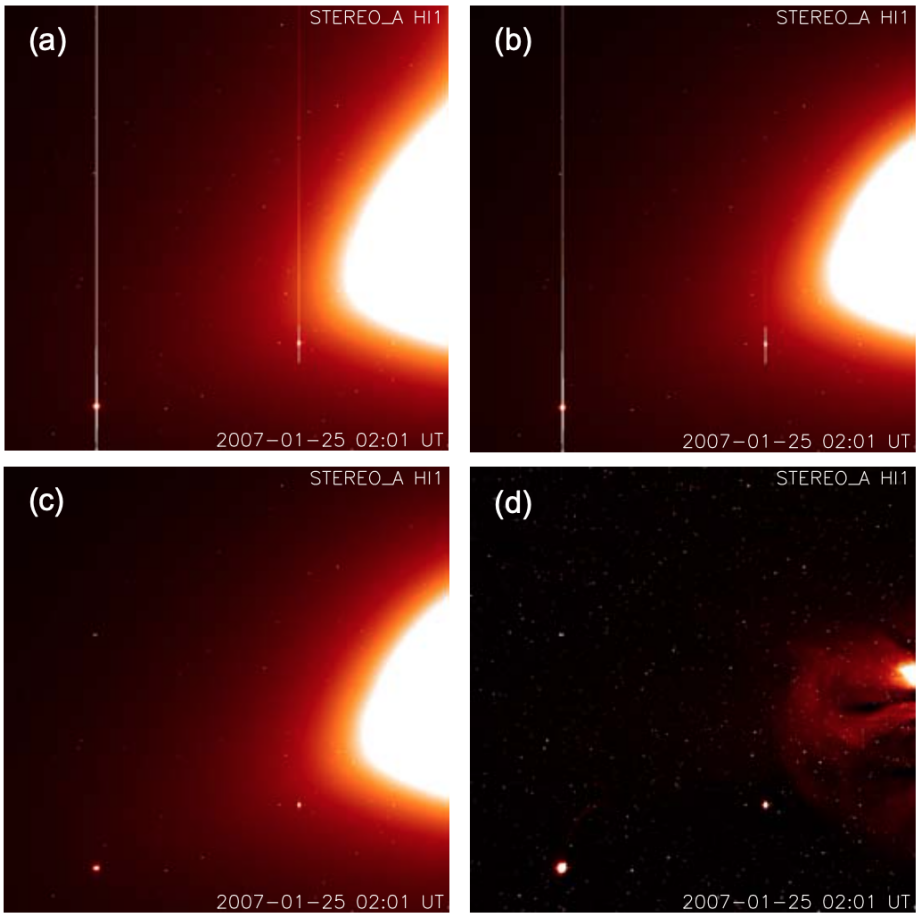

Figure 3.6: An *Heliospheric Imager* image undergoing the stages of image processing to bring out fainter features. This image is from STEREO-A HI1 taken on 25 January 2007. The steps are as followed: (a) the raw image, (b) SECCHI_PREP has been used to apply corrections for shutter-less operation and the flat-field, (c) the ''blooming'' caused by saturation around the planets Venus and Mercury have been removed, and (d) the background has been subtracted to reveal a Coronal Mass Ejection. Sourced from *Eyles et al.* (2009).

is called a running differenced image (*Eyles et al.*, 2009). This method has the advantage of highlighting features that change between images; bright regions show areas of increased plasma density between frames while dark regions shows areas of decreasing plasma density. This technique improves the clarity of CME fronts, although introducing uncertainty into the exact time at which the feature was recorded. Differenced images were used to identify the CME fronts studied in this thesis.

3.2.3 Thomson Scattering

Thomson scattering is the process of sunlight being scattered by free electrons within a plasma, beneficial to understanding the geometry of signals observed. Originally, the theory was developed to explain coronagraph observations, including the detection of CMEs close to the Sun (*Billings*, 1966). Since Thomson scattering has been applied to interpretation of photometric data from HI cameras despite the major difference in field-of-view of the two instruments (*Deforest et al.*, 2013b; *Howard and Deforest*, 2012b; *Howard et al.*, 2013). When using *Heliospheric Imager*, understanding the geometry and signal of observation is essential to infer the plasma properties. A free election has a scattering efficiency which is greatest in the plane of incoming light (0° and 180°) and weakest at right angles (90° and 270°). In a simplified heliosphere that has a spherically symmetrical density distribution of solar wind plasma, the density of free electrons decreases with distance away from the Sun. Observations along a particular line of sight will detect the strongest signal from the point that is closest to the Sun. For an observer away from the Sun, the closest point is at right angles from the light source. Over a range of line-of-sight angles, the point of closest approach to the Sun will have varying longitudinal and elongation angles which together form a spherical locus, known as the Thomson Surface (*Vourlidas and Howard*, 2006). This is shown in Figure 3.7. *Howard and Deforest* (2012b) gives a detailed explanation of the theory of light detection in HI cameras and addresses the important difference between radiance and intensity measurements. A brief summary of this work is given here.

A small scattering site is defined as a unit volume of space with a number density of electrons, $n_e(s, \varepsilon, \xi)$, where n_e is the electron number density positioned along the line-of-sight at distance s from the Thomson Surface with elongation angle ε and angle ξ from the plane of sky (as seen in Figure 3.7). Identification of a single electron is not possible and, therefore, a small scattering site is used alternatively. The scattering site is considered to be at a distance r from the Sun (or distance from the observer, z, however this distance not used in the following notation) with scattering angle χ.

Radiance, B, of the scattering object is given in Equation 3.1 as the product

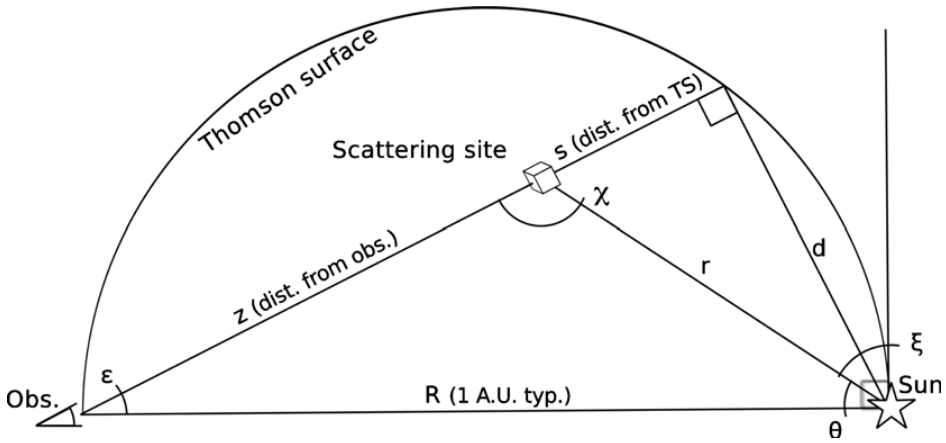

Figure 3.7: The Thomson scattering geometry of a scatter site distance r from the Sun, as would be observed by the *Heliospheric Imager*. The line of sight with elongation ε passes through the scattering site, making an angle of χ with the radial from the Sun. The distance along the line of sight is measured in terms of s when measured from the Thomson surface and z when from the observer. Sourced from *Howard and Deforest* (2012b).

of three functions dependent on Thomson scattering geometry. The full expanded version of this equation can be found in *Howard and Deforest* (2012b).

$$dB = k_{TS}(\varepsilon)G(\chi)n_e(s, \varepsilon, \xi)ds \tag{3.1}$$

Along a line of site, which ε is fixed, the position of the scattering site is dependent of χ and s. The function $k_{TS}(\varepsilon)$ is independent of these two parameters and, therefore, along a line of site can be considered a constant. Surface brightness, $G(\chi)$, is variable along a line of site, but the function reveals a new feature of the theory; for changes in the scattering angle the function has a plateauing maximum of $\Delta\chi = 90°$ symmetrical about the Thomson Surface. This relatively broad region is known as the Thomson Plateau. Near-constant measurements of surface brightness are observed for plasma propagating within the Thomson Plateau. Fortunately, this simplifies the interpretation of photometric data. While $G(\chi) =$ constant, HI sensitivity is only dependent on the electron number density (third function) along a line of sight (*Howard and Deforest*, 2012b).

The HI instrument detects the intensity of light directed towards the camera.

Intensity is determined as the integral of radiance over the apparent feature size, given in Equation 3.2 where Ω is the apparent size of the scattering object. Understanding how solar wind structures are observed via intensity measurements is important.

$$dI = Bd\Omega \tag{3.2}$$

When the scattering site is close to the observer along a line of sight, more light photons will be scattered toward the instrument. Intensity will be greater due to the apparent size being larger. By knowing the location of the scattering site relative to the observer, θ, the apparent size can be inferred. For features in the region of the Thomson Plateau, features furthest from the Thomson Surface are easier to detect.

3.3 Analysis of Bright Features

The aim of processing HI images is to expose the bright features, but what information can we retrieve from this? Some coherent structure of bright pixels are interpreted as fronts of enhanced plasma density, associated with transient events. A shock front, the leading edge, and the magnetic core are some of the CME features that have increased plasma density. A CME event can have some, if not all, of these features and, thus, it is common for multiple bright regions to be visible in processed HI images. Occasionally, multiple CMEs are released in quick succession such that they occupy the HI FOV at the same time, and tracking the events separately becomes challenging.

3.3.1 Multiple Signatures Detection

Confidently linking the observed bright regions to the classic CME structure is not as simple as assuming the expected sequence of shock, leading edge and core (*Lugaz et al.*, 2012). In this next section, we discuss the numerous interpretations of fronts within CMEs imaged by HI.

Shock Fronts

CMEs can drive shocks ahead of the eruption, separated from the leading edge by a region of compressed plasma and magnetic field called the sheath (*Owens et al.*, 2005). Not all CME events have associated shocks. Commonly, fast events drive shocks due to their significant difference in propagation speed or expansion speed

in comparison to the ambient solar wind (*Lugaz et al.*, 2017). When shocks are present, an enhancement of electron density can be observed in in-situ data from the pile-up of material. Some researchers (e.g., *Pant et al.*, 2016) have identified enhanced brightness in HI images that appear to correspond to the position of the shock (in in-situ data) although these observations were made at different stages of the CME evolution.

CME Features

In addition to shock front, of the three-part CME structure (*Illing and Hundhausen*, 1985), the leading edge and the core can have a sufficient electron density to be detectable by the HI instrument (e.g. *Davis et al.*, 2009; *Li et al.*, 2021; *Liu et al.*, 2010a). Between these two bright fronts, a depletion corresponding to the magnetic cloud is observed (*Howard and Deforest*, 2012a).

Ghost Front Theory

A study by *Scott et al.* (2019) noted that the CME event on 12 December 2008 contained two similar fronts in the outer edge of the CME as observed in HI1 images, however, no shock front was identifiable in L1 in-situ data. In this case, the multiple fronts formed a similar latitudinal structure and were separated by only a few degrees of elongation. When a CME structural feature intercepts the Thomson Sphere it is possible for the HI camera to see two enhancements of the same CME feature; one corresponding to the plasma dense region along the feature nose and one from the region in the vicinity of the surface (*Manchester et al.*, 2008). However, for the December 2008 event, the extent of the CME when viewed by the HI1 camera is considerably smaller than the Thomson sphere, and so it was concluded that these similar fronts were produced by two regions of enhanced Thomson scatter. *Scott et al.* (2019) theorised that these fronts were the location of two regions of the CME leading edge; the nose and the flank (the tangent of greatest elongation to the leading edge). At the nose of the CME, where the leading CME front lies along the line of propagation, there is a pile-up of material as the CME sweeps through the heliosphere. This region is likely to appear bright in HI images because of the localised increase in plasma density. Thomson scattering theory tells us that the intensity of scattered light in each pixel of an HI image is proportional to the density

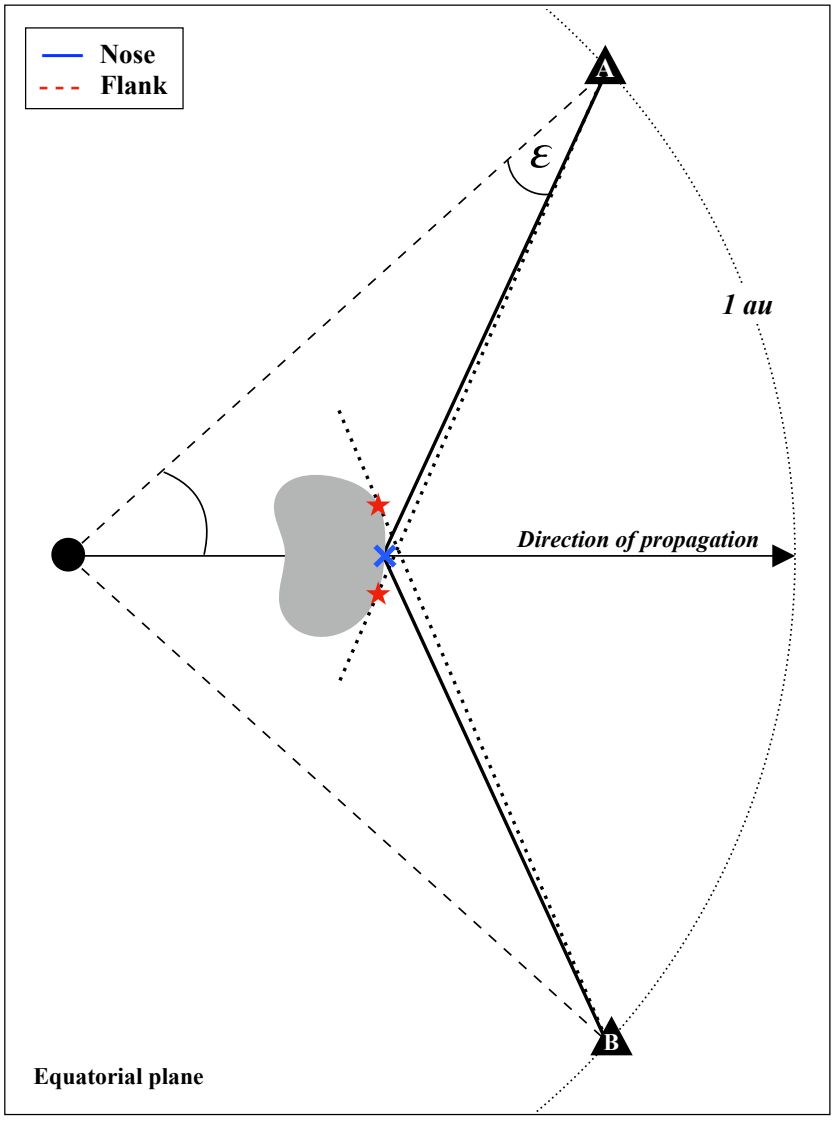

Figure 3.8: Schematic of Ghost Front theory in the equatorial plane. A CME (grey shape) is propagating away from the Sun (black circle) with two spacecraft, labelled A and B, representing the STEREO spacecraft, observing the trajectory. From the point of view of the spacecraft, the Ghost Front theory states enhanced plasma density along the nose of the leading edge (blue plus sign, solid black line of sight) and cumulative dense region along the line of sight of the leading edge flank (red cross, dotted black line of sight). These two features will have different elongation angles, ε, from the point of view of the observer at A or B.

of free elections integrated along that line of sight as a function of distance from the observer. Thus, the tangent to the leading edge can also appear bright due to the cumulative plasma density integrated along the extended line of sight. With the STEREO spacecraft positioned approximately 40° from the Earth during the CME event in 2008, the flank corresponded to the outer front in HI1 images, and the nose resulted in an enhanced signal at slightly lower elongations. It is this secondary front that was denoted as the ‘‘ghost’’ front.

The Ghost Front theory has also been applied in the work of *Chi et al.* (2021) to interpret and simulate bright features within CME images. It was shown to be consistent with observations over a range of latitudes. This suggests that measuring the elongation difference between ghost fronts can help us determine a CME's longitudinal extent and/or width, by using images from a single spacecraft. Further, there has been a suggestion that using both the nose and the flank to optimise HI1 fitting could improve the forecasting abilities of CMEs at L1/ Earth (*Barnard et al.*, 2020; *Hinterreiter et al.*, 2021).

3.3.2 Time-Elongation Profiles

Regardless of the number of features detectable in HI differenced images, there is evidence to suggest value in using HI images to understand the propagation of transient events (*Harrison et al.*, 2017). Such an idea is to use the position of the bright feature to infer the position of transient events in the heliosphere with respect to time. With multiple observations, it is possible to estimate the average speed and direction of CMEs through time-elongation profile analysis. Such time-elongation plots of the solar wind along a given solar latitude have become known as ‘‘J-maps’’.

J-Maps

Time-height maps of coronagraph observations from ESA's *Solar and Heliospheric Observatory* (SOHO), *Large Angle and Spectrometric Coronagraph* (LASCO) were first developed by *Sheeley et al.* (1999). Radial profiles were extracted from images and stacked sequentially to highlight tracks of solar transient events out to the limit of the C3 LASCO field of view: 8° elongation.

Rouillard et al. (2008) and *Sheeley et al.* (2008) applied the technique developed by *Sheeley et al.* (1999) to plots of elongation versus time, interpreting the apparent

change in speed (gradient of slope) as being caused by the direction of propagation with respect to the observer. Events travelling towards the observer appear to accelerate as they cross increasingly larger elongations between frames. Conversely, events travelling away from the observer appear to decelerate (the gradient decreases) as their motion at a distance leads to a smaller increase in elongation. By assuming a transient is travelling at constant speed and direction it is possible to conduct a two parameter fit to the acceleration profile, resulting in an estimate of transient average speed and direction.

If a feature is moving away from the Sun at a constant speed, v_r, and therefore increasing in radial height, r, linearly with time, time can be inferred from the ratio of radial height against observer distance from the Sun, $\rho = r/D$. The rate of change of the elongation angle, ε, can be given by:

$$\frac{d\varepsilon}{d\rho} = \frac{cos(\xi)}{1 - 2\rho sin(\xi) + \rho^2} \tag{3.3}$$

where ξ is the angle from the plane of sky. As a result, the apparent speed of the feature, v_s can be given by

$$v_r \frac{d\varepsilon}{d\rho} = D\frac{d\varepsilon}{dt} = v_s \tag{3.4}$$

This technique inspired *Davies et al.* (2009) to develop a process to use STEREO's HI data to observe transients out to distances of Earth and beyond, where CME impact is of threat. To produce J-maps using HI images, a more complex method is undergone than a simple stacking of images. For an image, each pixel column is represented by the mean of the central 64 rows, producing a single-row data representation of the image. A series of such slices are then stacked horizontally to form a time series. Both HI1 and HI2 data are used to produce one of these maps, where HI1 data is chosen for the overlap between the two fields of view. An example of a J-map is shown in Figure 3.9. Running difference images are used in the process so we find the map in grey scale where the brightness of the pixel continues to represent changes in the plasma density. A CME tracked through a J-map is identifiable by a bright structure (the plasma dense leading edge) followed closely by a dark feature (the less dense cavity) that has increasing elongation angle with time. A key part of these maps is that anti-sunward features that can be seen out to far elongations, where the outer front of CMEs is faint in individual HI images.

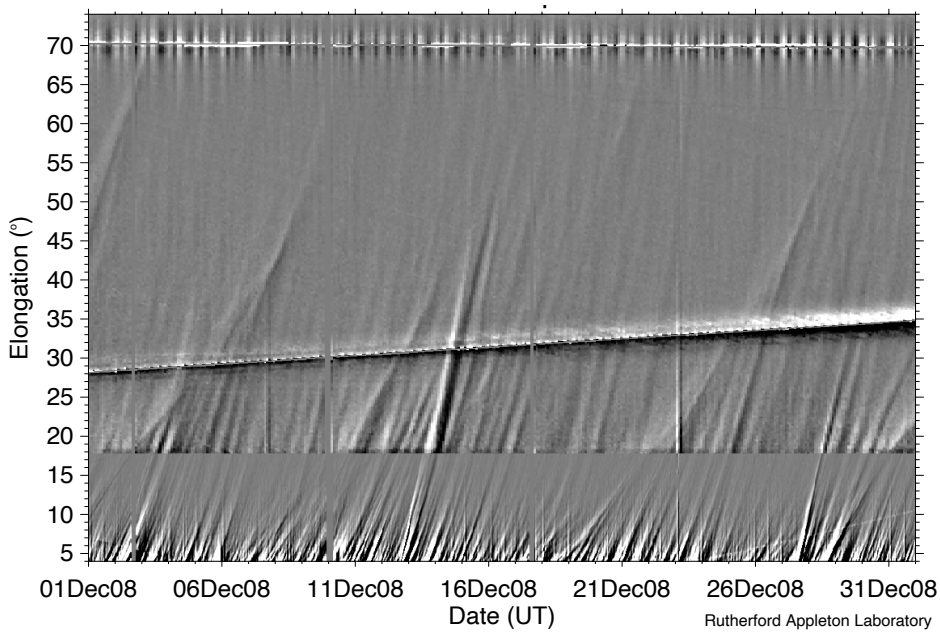

Figure 3.9: A J-map for December 2008, developed from differenced images of HI1 and HI2 onboard STEREO-A. Bight pixels highlight a region of increasing plasma density meanwhile dark regions show regions of decreasing plasma density. A CME can be identified by ''J''-like structures of bright pixels superseded by dark pixels. The sharp horizontal discontinuity at 18° is caused by the sensitivity difference between the two cameras. Faint parallel lines moving sunward (negative gradient) are caused by the remaining signatures of stars in the HI images. A planet can also be seen moving anti-sunward from 28° to 35°. The remaining anti-sunward features are solar transients captured by the HI cameras. Image is sourced from Rutherford Appleton Laboratory.

The clear signal between the black and white boundaries is produced from the core material whilst fainter tracks correspond to the outer loops (*Davies et al.*, 2009).

By fitting an elongation profile to the map, we can infer information about the CME launch direction, radial speed and radial height from which the launch time or Earth-arrival time can be estimated. However, to make these estimates it is assumed that CME speed and direction are constant despite this not being true in many cases (*Gopalswamy et al.*, 2001; *Vršnak*, 2001). Furthermore, through the averaging technique used to produce J-maps, the fine structures of CMEs, such as the leading edge, will become fainter with greater elongations. One study demonstrated that tracking CMEs in J-map can lead to significantly different estimates of CME kinematics as it is not clear what feature is being tracked and there is great uncertainty

of the time coordinates (*Barnard et al.*, 2017). Thus, the use of J-maps to estimate CME speed and direction can have large uncertainties that limit the use of this technique in space weather forecasting (*Barnard et al.*, 2017).

3.4 Modelling a CME

Using observations of the Sun and the heliosphere provides us with means to use these measurements to model CME propagation from near-Sun to Earth's orbit. Solar wind models, such as MHD models, have been developed to simulate the ambient background solar wind and HCS (*Odstrcil*, 2003; *Pomoell and Poedts*, 2018). However, these usually require a full latitude-longitude map of the Sun, taking up to 27 days when viewed from a single viewpoint (*Owens*, 2020; *Vršnak et al.*, 2014). Over this long duration, it is not possible to simulate transient events, like CMEs, unless they are artificially injected by CME models, like the cone model. Methods have been developed to estimate the three-dimensional shape, direction and speed of CME events based on two-dimensional imagery which can then be used as inputs to a solar wind model. This combination of techniques is used to model how a CME propagates through the inner heliosphere, enabling estimates to be made of CME parameters, and providing a forecast of the CME arrival at Earth. Here, we discuss the various models currently used to simulate CMEs.

3.4.1 Cone CME representation

Beyond the first few solar radii, CMEs have been observed to approximately propagate radially and remain at a constant angular width (*Plunkett et al.*, 1997; *Webb et al.*, 1997). A cone model of a CME was developed by *Zhao et al.* (2002) to give a three-dimensional representation of the CME that conforms to these observations. This premise was developed using Halo CMEs expanding towards the LASCO spacecraft at L1; a near-perfect circle of bright light is a characteristic of Halo CMEs and for such formation to occur it was concluded that the angular width throughout the CME's expansion from the source must remain constant and that the origin of the eruption was close to the circle centre. A simple cone shape with the point of the cone at the Sun center could replicate this, as shown in Figure 3.10. Free parameters determine the central axis, Z_c, using the latitude and longitude in the modelled

plane, and the CME angular width, α. In the figure, a cone with coordinate system (x_c,y_c,z_c) is orientated in the heliocentric coordinated system (x_h,y_h,z_h) where the relation between these two planes are determined by the heliographic latitude (λ) measured from the solar equator and the heliographic longitude (ψ) measured from the central meridian (*Michalek*, 2006). These cone parameters are informed from coronagraph observations (*Millward et al.*, 2013; *Zhao et al.*, 2002). With the launch of STEREO, these cone models benefited from the ability to constrain the model using observations from two or more different view points.

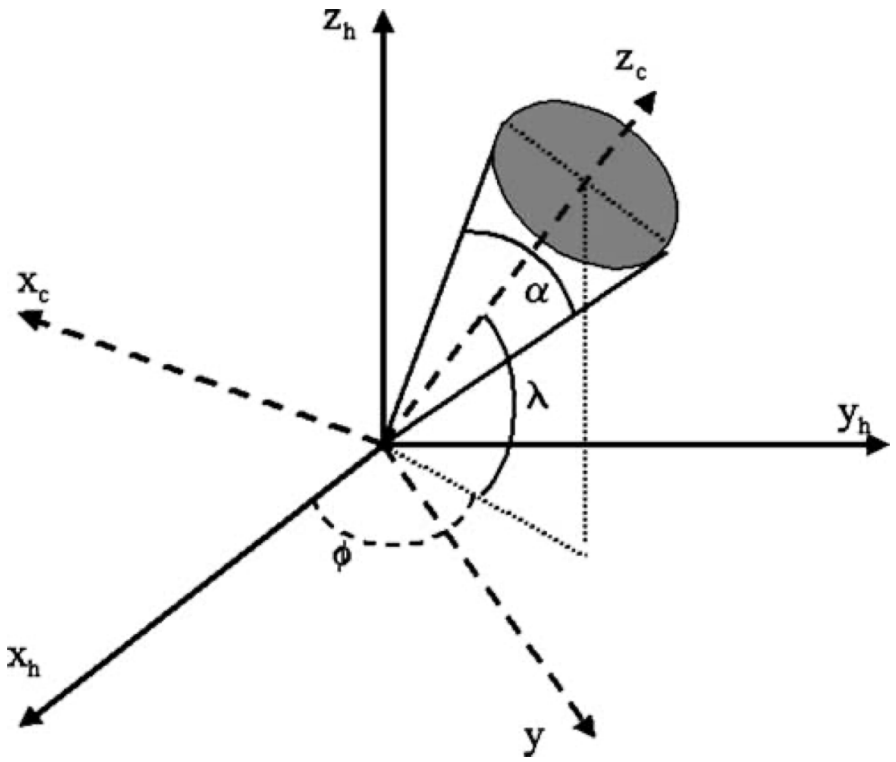

Figure 3.10: Schematic of the cone CME model where the point of the cone is positioned at the center of the Sun. The cone coordinate system is given by (x_c,y_c,z_c), where the central axis of the cone is z_c with angular width α. The cone is shown in the heliographic plane of coordinates (x_h,y_h,z_h) where the relation between the two planes is given by the latitude, λ, and longitude, ψ, measured from the solar equator and central meridian respectively. Sourced from *Michalek* (2006).

3.4.2 CME expansion

Geometric Models

Geometric models are techniques used to fit simple two-dimensional shapes (most often in the ecliptic plane) that best represent the position of the CME outer boundary determined from HI images (most often using J-maps). In this way, estimates of the kinematic evolution of CMEs can be made. Currently, there are four well establish CME geometric models; fixed-phi (*Rouillard et al.*, 2008; *Sheeley et al.*, 1999), harmonic mean (*Lugaz et al.*, 2009), self-similar expansion (*Davies et al.*, 2012), and elliptical conversion model (ELCon; *Möstl et al.*, 2015; *Rollett et al.*, 2016). Each of these is discussed below.

Using elongation measurements between Sun-Observer-Object, the maximum elongation corresponds to the CME flank. The position of this feature is then used to fit the shape from which parameter estimates are derived. From a sequence of HI images, speed-time profiles of the CMEs are produced (*Harrison et al.*, 2012; *Mishra et al.*, 2014; *Rollett et al.*, 2012) and been used to estimate CME arrival (*Amerstorfer et al.*, 2018; *Rollett et al.*, 2016).

Fixed Phi

The Fixed-Phi (FP) fitting assumes the CME outer boundary corresponds to a point source that is radially moving away from the Sun in a constant direction, such that the Observer-Sun-CME apex angle, Phi (Φ), remains constant (*Rouillard et al.*, 2008; *Sheeley et al.*, 1999).

Harmonic-Mean Fitting

The Harmonic Mean (HM) fitting represents a CME as having a circular cross-section. With one point anchored to the Sun centre, the circle expands with time such that the radial distance increases (*Lugaz et al.*, 2009).

Self-similar Expansion

The Self-Similar Expansion (SSE) fitting maintains the assumption that a CME has a circular cross-section, but expansion is constrained by also assuming a constant angular half-width (λ) of the CME, measured from the central axis of

the event (*Davies et al.*, 2012). The technique was further developed to include a CME of elliptical cross-section (ELCon; *Rollett et al.*, 2016).

With all these techniques, as the CME propagates in the heliosphere the radial distance of the CME leading edge, r, will increase with time, t. The elongation angle of the CME front, ε, will also increase with time . By using time-elongation profiles, the radial distance can be calculated for the SSE fitting using

$$r(t) = \frac{r_{obs} sin(\varepsilon(t))(1 + sin(\lambda))}{sin(\lambda) + sin(\Phi + \varepsilon(t))}. \tag{3.5}$$

where λ is the angular half-width and Φ is the Observer-Sun-CME apex angle. If λ =0° then the model represents FP fitting and if λ =90°, then HM fitting is replicated.

Each model has been shown to reproduce the kinematics of some CMEs better than others, based on their characteristics. Narrow eruptions are well represented with the FP fitting, whilst wide events are better simulated using the other techniques. These tools do come with assumptions which give rise to uncertainties (*Barnard et al.*, 2017). Firstly, it is assumed that the ambient solar wind is constant. Thus, CME evolution is not affected. As discussed earlier, CMEs evolve as non-symmetric bodies (*Owens et al.*, 2017). Secondly, the models consider that the direction, angular half-width, and aspect ratio of the CME remains constant. An advantage of these simple models is that they can use observations from a single observer and can produce reasonable results from few observations, making the geometric models easy and computationally cheap to use.

Drag-Based Modelling

If the CME direction can be determined from coronagraph observations, the radial speed profile of the CME can be estimated. Interaction with the ambient solar wind can lead to CME acceleration or deceleration depending on the relative speed of the CME and solar wind. This drag effect is proportional to the square of the speed difference between the two and accounting for this force is known as drag modelling. By including drag-based modelling, comparisons with observations can also lead to an estimate of the CME deceleration, modifying the in-situ properties of a CME at Earth.

The ELipse Evolution model based on Heliospheric Imager (ELEvoHI; *Rollett et al.*, 2016) combines geometric and drag-based modelling of the CME. Using the ELCon representation, an elliptic-front CME evolves with time to produce estimates of arrival at Earth (or any point of interest). An ensemble approach, varying the ELCon parameters inline with HI observation, has also been adopted (*Amerstorfer et al.*, 2018).

CME expansion models have been used to test their forecasting abilities (e.g. *Amerstorfer et al.*, 2018; *Barnard et al.*, 2022; *Braga et al.*, 2020; *Möstl et al.*, 2013; *Riley et al.*, 2018a) but have not been able to reliably improve forecast arrival times over current operational forecasts, in which CME conditions are fed into a physics-based solar wind model such as ENLIL (discussed below).

Kinematic Expanding Flux-Rope Model

Assumptions of a CME maintaining its shape through the heliosphere in geometric models is inconsistent with observations of magnetic clouds. The Kinematic Expanding Flux-Rope model was developed to relax this assumption by allowing a symmetric cross-section at initialisation to deform by self expansion and radial expansion within a uniform solar wind (*Owens et al.*, 2006). This highlighted that changes to a CME shape are not only due to coupling with the solar wind but also the CME's magnetic energy, even in idealised conditions. This technique was extended to explore the propagation of a kinematically distorting flux-rope within non-uniform solar wind conditions (*Owens et al.*, 2006) which has been shown to have reasonable agreement with HI data (*Savani et al.*, 2010).

3.4.3 Heliospheric Models

Based on the Magnetohydrodynamic (MHD) equations, numerical models are able to demonstrate CME interaction with a structured solar wind. These heliospheric models typically can simulate plasma outflow from the Sun in one, two or three spatial dimensions using near-Sun, time-dependent conditions at the inner boundary. A prime example of such a model is ENLIL (*Odstrcil*, 2003), originally developed to provide solar wind conditions at Earth from photospheric magnetograms (*Vršnak et al.*, 2014).

Modelling the corona and the heliosphere separately is sensible due to the vast

differences in the physics of these regions, as was discussed in Chapter 2. Therefore, magnetic field properties from the photosphere are supplied to coronal models to derive solar wind structure at $20\,R_\odot$ to $30\,R_\odot$ from the Sun using physical and empirical relations. For example, Wang-Sheeley Arge (solar wind speed prediction method) (WSA; *Arge et al.*, 2004) feeds magnetograms into the steady-state Potential Field Source Surface model (*Altschuler and Newkirk*, 1969; *Schatten et al.*, 1969). Field lines are extended to simulate coronal loops in the inner corona. An upper boundary of the Potential Field Source Surface model, typically at $2.5\,R_\odot$, determines the open and closed field lines present in the outer corona. This information is fed into the Schatten Current Sheet model (*Schatten*, 1971) which uses an empirical relation, based on magnetic divergence around active regions, to compute the solar wind speed at $21.5\,R_\odot$. Another example is the Magnetohydrodynamic Algorithm outside a Sphere (MAS) coronal model (*Linker et al.*, 1999); a spherical, time-dependent MHD solution of the photospheric magnetic field which generates a solution of plasma and magnetic field at $30\,R_\odot$, assuming constant density at the base and a radial outflow.

Typically, WSA provides solar wind conditions as input to the inner boundary of the ENLIL model (a.k.a., WSA+ENLIL; *Odstrcil et al.*, 2004). Development of the model allowed CME evolution to be simulated as well. Upon observation of a CME in coronagraph images, the CME's initial properties are included in ENLIL as a cone-CME (further abbreviated as WSA+ENLIL+Cone) and defines a perturbation of velocity, density, and temperature in the ambient solar wind structure at the inner boundary (*Odstrcil et al.*, 2004; *Vršnak et al.*, 2014). Through this method, estimates of the CME intensity and arrival at Earth are produced (*Pizzo et al.*, 2011).

There are a number of similar 3D MHD numerical models available to the science community. European Heliospheric Forecasting Information Asset (EUHFORIA) has been designed to combine a coronal model (photosphere to 0.1 au) and a heliospheric model (0.1 au to 2 au) with a cone representation of a CME inserted at the heliospheric inner boundary height (*Pomoell and Poedts*, 2018). The HelioMAS model projects the MAS output of magnetic field, density and temperature at $30\,R_\odot$ out to 1 au (*Riley et al.*, 2001). The Space Weather Modeling Framework (SWMF) is a multiplex of numerical models, allowing simulation of the Sun-Earth system (i.e., solar corona, inner heliosphere, magnetosphere, ionosphere and more), thus, providing a flexible

model for space weather science (*Tóth et al.*, 2005).

Forecasting

Operationally, NOAA's Space Weather Prediction Center (SWPC) and UK Met Office's Space Weather Operation Centre (MOSWOC) use WSA+ENLIL+Cone to produce deterministic and ensemble forecasts of CME arrival at Earth (*Mays et al.*, 2015; *Pizzo et al.*, 2011). A deterministic run is a single-member run of a model that is often initialised with input parameters that are assumed precise to produce a model outcome that is not subject to uncertainty. An ensemble run is comprised of multiple model runs where the input parameters of each run are perturbed slightly to given a range of possible outcomes. The parameter space in which the initial conditions can vary tend to equal the uncertainty of the parameter. To produce an ensemble forecast, the range of outcomes in quantitatively analysed to produce likelihoods of scenarios important for the end user. A single run of the WSA+ENLIL+Cone takes approximately 20 min, plus the additional time to accumulate recent data in near real-time operations (*Zheng et al.*, 2013). Computing an ensemble in a reasonable time, therefore, limits the number of runs in an ensemble forecast (*Cash et al.*, 2015; *Lee et al.*, 2013). For example, the MOSWOC computes 24 runs in their forecast (*Henley and Pope*, 2017).

3.4.4 HUXt: A Simplified-Physics Heliospheric Model

Heliospheric Upwind eXtrapolation with Time dependencies (HUXt; *Owens et al.*, 2020a) is a reduced physics 1-D numerical model used to simulate heliospheric conditions and CME propagation. To do this, the complex magnetic equations that are found in full-physics 3-D models, like ENLIL (*Odstrcil*, 2003), are simplified greatly to the assumption that the plasma is purely radial and behaves as an incompressible and inviscid hydrodynamic flow (more on this below). Modelling in the equatorial plane, the heliosphere is represented by a grid of angular resolution 2.8° and radial resolution 1.5 $R_\odot$, replicating the grid framework of the HelioMAS model (*Riley et al.*, 2001). In the steady-state approximation, this simplified-physics approach was shown to closely match 3D MHD output (*Riley and Lionello*, 2011) and has recently been adapted to allow for time-dependent solar wind structure (*Owens et al.*, 2020a). Even with the high level of physical approximation, HUXt can

replicate the outwards movement of plasma to beyond 1 au within 6.4 % accuracy of the full-physics model, validated against 40 years' worth of data and the HelioMAS model (*Owens et al.*, 2020a; *Riley et al.*, 2001). Due to these simplifications, the time for a single run of HUXt takes a fraction of a second on an average desktop computer, significantly less than the full-physics models. The computational efficiency of this model enables the computation of large many-member ensembles, as has been done by *Barnard et al.* (2020) and is the premise of this thesis.

What is the reduced physics?

From above the mid-corona and out to 1 au the plasma β is large (*Gary*, 2001) and thus the magnetic forces can largely be neglected. In this domain, where heliospheric models are typically run, the fluid momentum equation of MHD can be simplified to

$$\frac{\partial \boldsymbol{V}}{\partial t} + (\boldsymbol{V} \cdot \nabla)\boldsymbol{V} = -\frac{1}{\rho}\nabla P - \frac{GM_{\odot}}{r^2}, \tag{3.6}$$

where $\boldsymbol{V}$ is the solar wind velocity, ρ is the plasma mass density, P is the plasma pressure, G in the universal gravitational constant, $M_{\odot}$ is the solar mass, and r is the radial distance from the Sun. This equation approximates the solar wind as a hydrodynamic flow; the first assumption of the reduced physics model.

The second assumption considers the solar wind as only moving radially out from the Sun. Beyond heliocentric distances of 30 $R_{\odot}$ (default inner boundary height for HUXt), non-radial flows and deflections (*Kay et al.*, 2015; *Owens and Cargill*, 2004) are less influential on CME propagation (*Owens et al.*, 2020a), so the radial outflow of CMEs can be a fair assumption. Furthermore, due to CME expansion speeds exceeding the Alfvén speed, points of the CME evolve independently (*Owens et al.*, 2017). From this approximation, the momentum equation is reduced to the inviscid Burger's equation

$$\frac{\partial V_r}{\partial t} + V_r \frac{\partial V_r}{\partial r} = 0, \tag{3.7}$$

where V_r is the radial velocity.

The final assumption considers the acceleration profile of the solar wind with radial distance. At the typically inner boundary height of 30 $R_{\odot}$, observations indicate that the solar wind is still accelerating (*Manchester et al.*, 2017; *Temmer et al.*, 2011; *Vršnak et al.*, 2008). With the simplification to only consider the solar

wind speed, this acceleration can only be addressed through an additional velocity function, $accV(r)$. *Riley and Lionello* (2011) state this function as

$$accV(r) = \alpha V_0 \left[1 - exp\left(\frac{-(r - r_0)}{r_H}\right)\right] \tag{3.8}$$

where the acceleration factor, $\alpha = 0.15$ and the scale height, r_H, of acceleration is $50\,R_\odot$. These values are in agreement with the HelioMAS results (*Riley and Lionello*, 2011). Therefore, at a given radial height, the solar wind velocity is found using

$$V(r_0) = V_0 + accV(r_0), \tag{3.9}$$

where V_0 is the solar wind speed at the model inner boundary height, r_0.

CME representation

Within HUXt, CMEs are introduced as a velocity pulse at the inner boundary with no magnetic field properties, meaning they are hydrodynamic structures. The shape of the CME is composed of two hemispheres connected by a cylinder and the size of the CME is determined from information about the source latitude and longitude, full width, speed, and radial thickness derived from cone-model fits to coronagraph images (*Barnard et al.*, 2022; *Millward et al.*, 2013; *Owens et al.*, 2020a). The length of the cylindrical portion of the CME is given by the thickness parameter, where a thickness of zero creates a purely spherical velocity perturbation and a thickness greater than zero produces a ‘‘sausage’’ shape velocity perturbation. By altering the thickness parameter and, thus, the size of the velocity pulse, the deceleration of the CME can be changed by effectively altering the CME momentum (*Owens et al.*, 2020a). In the version of HUXt used in this research (Version 1.0.0), the CME shape is set by multiple grid cells adjacent to each other, with the shape of the boundary being restricted by the grid resolution. In order to track the CME disturbance through the model, the boundary of a CME is defined as where the velocity difference per grid-cell is greater than $20\,\mathrm{km\,s^{-1}}$ compared with the ambient (i.e. no CME) solar wind solution.

Chapter 4

Application of ghost-front modelling to a CME event

This chapter discusses the method of modelling a CME ghost-front (*Scott et al.*, 2019) with the reduced-physics Heliospheric Upwind eXtrapolation with Time dependencies (HUXt; *Owens et al.*, 2020a) model using the case study event from 12 December 2008. By evaluation of time-elongation profiles of the CME leading front, the position of the nose and flank are compared with the position of bright fronts in *Heliospheric Imager* (HI) images. Hence this chapter is, essentially, investigating if longitudinal distortion can be inferred from HI observations. An ensemble approach is introduced and applied, relating the uncertainty of the model's inner boundary conditions to CME arrival estimates. This chapter is part one of a peer-reviewed publication (*James et al.*, 2023).

4.1 The 12 December 2008 CME event

The first Earth-directed CME to be studied in detail from the twin viewpoints of the STEREO spacecraft occurred on 12 December 2008. The Heliocentric Earth Equatorial (HEEQ) position of STEREO-A was 42.1° longitude and −5.4° latitude

at 0.97 au from the Sun meanwhile STEREO-B was positioned at −44.2° longitude and 4.9° latitude at 1.04 au, shown in Figure 4.1. The CME was first observed by COR2 at 10:37 UTC, when the CME had reached a radial distance of 7.9 $R_\odot$. Later the same day, at 20:49 UTC, the CME was observed by HI-1 at a radial distance of 34 $R_\odot$.

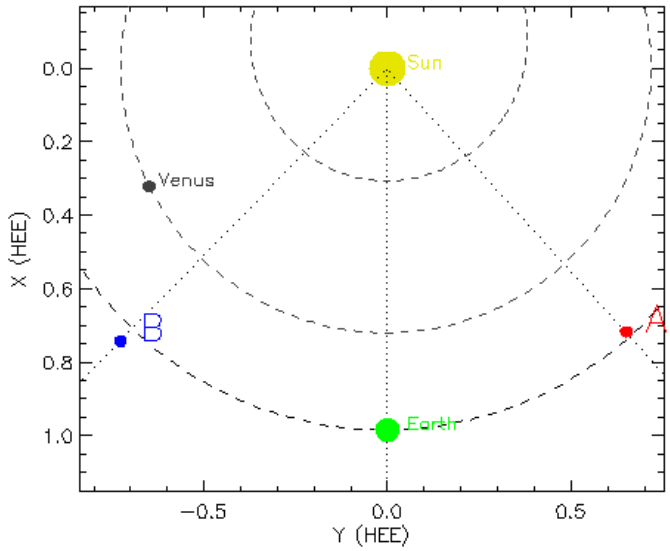

Figure 4.1: Position of STEREO and Earth at 12 December 2008, 10:37 UT. Sourced online (`https://stereo-ssc.nascom.nasa.gov/cgi-bin/make_where_gif`, accessed May 2023).

Analysis by *Scott et al.* (2019) of this event evaluated the near-Sun conditions of the CME from coronagraph data. The CME was reconstructed using the CME Analysis Tool (CAT) model (*Millward et al.*, 2013), geometric localisation (*Koning et al.*, 2009), and equal masses techniques (*Colaninno and Vourlidas*, 2009). CAT is a visual comparison technique that uses a three-dimensional teardrop-shaped grid to visually match the outer edge of CMEs in multiple white-light images simultaneously, typically from coronagraphs. The shape of the geometric grid can determine the latitude, longitude, width, and radial speed of the CME. It is assumed the CME will have a spherical front and does not accelerate between different observations used to determine the radial speed (*Millward et al.*, 2013). It is used in operation by NOAA's Space Weather Prediction Center and UK Met Office's Space Weather Operation Centre. Variations to CAT include an elliptical cross-section and a variable curvature

Table 4.1: Parameter estimates for the 12 December 2008 CME based on the Heliospheric Imager field of view.

Parameter	Value
Solar Longitude	$10° \pm 4°$
Solar Latitude	$9° \pm 2°$
Width	$42° \pm 6°$
Radial Speed	$497\,\mathrm{km\,s^{-1}} \pm 63\,\mathrm{km\,s^{-1}}$

to the grid such that the CME front could be either spherical, flat, or somewhere in between. When fitting to the 12 December 2008 CME, both of these variations were included in the CAT reconstruction (*Scott et al.*, 2019). Geometric localisation uses multiple viewpoints to triangulate on a quadrilateral region containing the CME to infer the latitude and longitude and map the CME trajectory to determine its radial speed (*Koning et al.*, 2009). The equal masses techniques acknowledges that the intensity of plasma will be viewed different due to the effects of Thomson scattering and the CMEs position relative the the plane of sky when observed by multi-viewpoint, such as that from STEREO. By calculating the electron density and mass along an integrated line-of-sight the direction (primarily, the longitude) and true mass of a CME can be concluded (*Colaninno and Vourlidas*, 2009). By averaging the parameters found through these three reconstruction methods performed on coronagraph data, it was concluded that the CME propagated along a solar longitude of $10° \pm 4°$ and solar latitude of $9° \pm 2°$ (HEEQ coordinates). The event was estimated to be travelling at $380\,\mathrm{km\,s^{-1}} \pm 1\,\mathrm{km\,s^{-1}}$. Reconstruction of the CME using HI-1 data was also carried out and the results suggested the radial speed of the CME had increased to $497\,\mathrm{km\,s^{-1}} \pm 63\,\mathrm{km\,s^{-1}}$ at the greater distances seen in these cameras. These speeds are in agreement with the CME's speed profile calculated by *Manchester et al.* (2017). These parameters, summarised in Table 4.1, are used in this work to simulate a CME event in the HUXt model.

This CME was tracked through the HI1 field of view using the same interface as used with Solar StormWatch (*Barnard et al.*, 2017). By identifying bright fronts within an HI image and taking the radial distance of these features where they

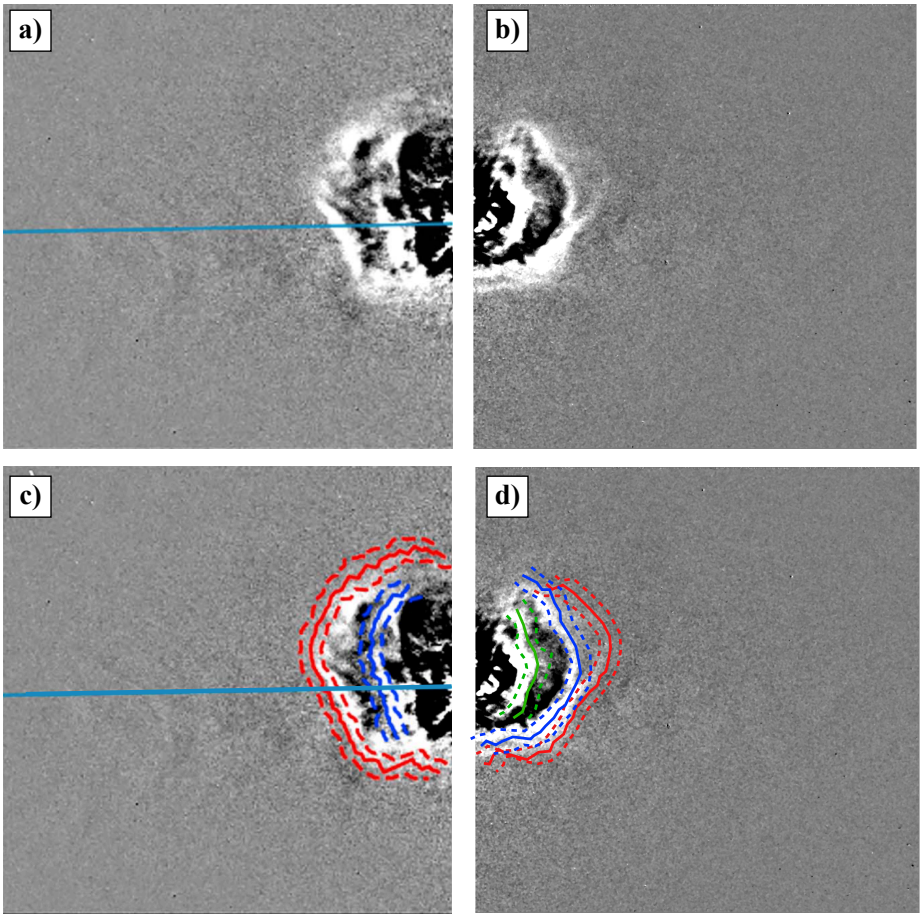

Figure 4.2: Running difference images from the Heliospheric Imager 1 instrument onboard STEREO spacecraft, taken on 12 December 2008, 22:49 UT. The bottom row shows the same image as the top row and includes the overlay of the bright front position (solid line) and one standard deviation (dashed line). Left = STEREO-A, right = STEREO-B. Fronts: red = outer, blue = inner, green = third (STEREO-B only).

cross a particular latitudinal plane, the elongation angle of each feature is measured. Under this process, with successive HI images, time-elongation profiles for the CME front can be produced along the particular latitude. To gather the data used in this research, the process of locating bright fronts in HI images was repeated by multiple scientist independently to produce a sample of elongation angle data along Earth's latitudinal plane. At a single time step and for a particular spacecraft, the sample of data was analysed using kernel density analysis to find the average and standard error of the elongation angle for each bright front identified. The evolution of the elongation angle data for a bright front as seen from a single spacecraft forms the time-elongation profile. For the 12 December 2008 case study, Figure 4.2 shows an example of front tracking in HI1 where two fronts were identified in STEREO-A data and three fronts from STEREO-B. These profiles were also included in the work by *Scott et al.* (2019), however, only two features were identified within STEREO-B's HI images. In the tracking tool, users were asked to track the position of ghost fronts and hence were limited to identifying two features in HI-1. In a case where more than two front features were present, such as the 12 December 2008 case, then it was possible for inconsistency between the fronts being tracked between users. The images were processed to allow the data to be categorised into more than two fronts. Figure 4.3 shows the revised time-elongation profiles of the fronts along the Sun-Earth line. We find STEREO-B's ''inner front'' to have a less-noisy profile, similar to the profiles seen by STEREO-A, and the third feature profile (shown in green) at a lower elongation. The third front can be associated with the highly dense core of the CME which has been discussed in previous studies of this event (*Byrne et al.*, 2010; *Davies et al.*, 2009). Hence, here in this work of ghost front theory, we exclude the time-elongation profile of the third front in our analysis.

It is worth noting that HI data from STEREO-B is considered to be noisier than STEREO-A due to a minor instrument fault. The HI images are not as sharp which complicates the post-processing of the data, such as aligning the star-fields between images. Bright fronts are still visible in STEREO-B's difference HI images, but the uncertainty of an elongation angle may not reflect the instrumental source of error. We continue to use the elongation profile from STEREO-B that is detailed above, but note that it is likely to obtain model results of greater error when compared to

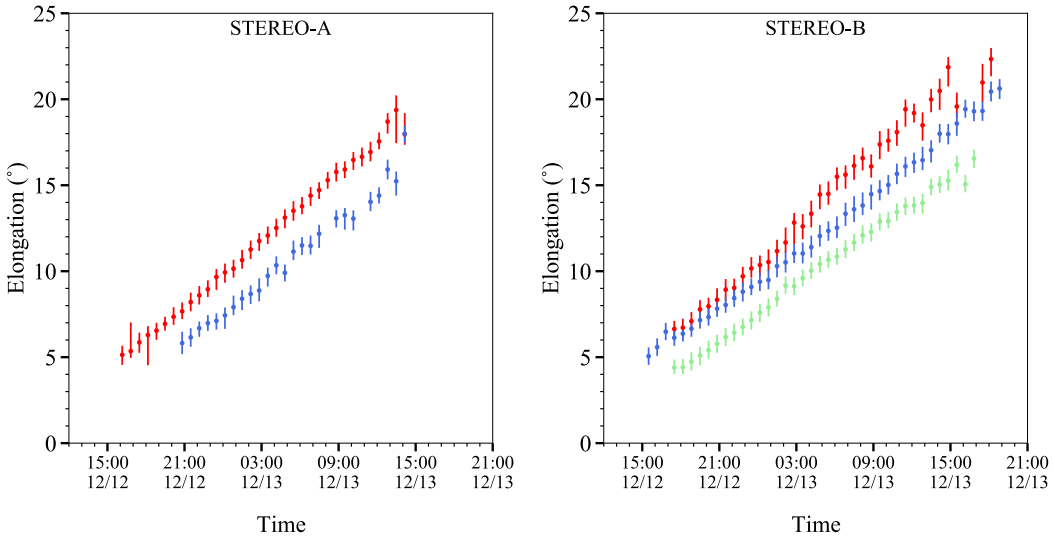

Figure 4.3: Time-elongation profiles for the 12 December 2008 CME event, taken along Earth's latitudinal plane, as identified using the Solar Stormwatch interface. Fronts are classified as either "outer" (blue), "inner" (red), or "third" (green). Only the outer and inner fronts are used in the analysis of ghost front features. The third front is likely to correspond to a density enhancement within the magnetic cloud.

the observations.

Traditionally, J-maps created from differenced images were used to extrapolate the trajectory profile of CMEs by identifying sharp changes in white-black boundaries of features that extended throughout the HI1 and HI2 field of view (*Davies et al.*, 2009). By obtaining the direction and speed of the CME, the CME's arrival at Earth could be estimated. This method can lead to considerable uncertainties since J-maps use an average position angle used to construct the maps, resulting in CME features appearing fainter at greater elongations (*Barnard et al.*, 2017). For this reason, we do not use the J-map method to produce the time-elongation profile. Instead, we demonstrate how the profiles obtained from the Solar Stormwatch technique correspond to J-map features in Figure 4.4.

From ACE data, seen in Figure 4.5, the enhancement in solar wind speed at 07:00 UTC ±1 h on 16 December 2008 is interpreted as the arrival of the compressed solar wind ahead of the CME, just under four days from the first COR observation. The solar wind speed increases from approximately 330 $\mathrm{km\,s^{-1}}$ at arrival to 370 $\mathrm{km\,s^{-1}}$ several hours later, along with an associated enhancement in ion density. It becomes

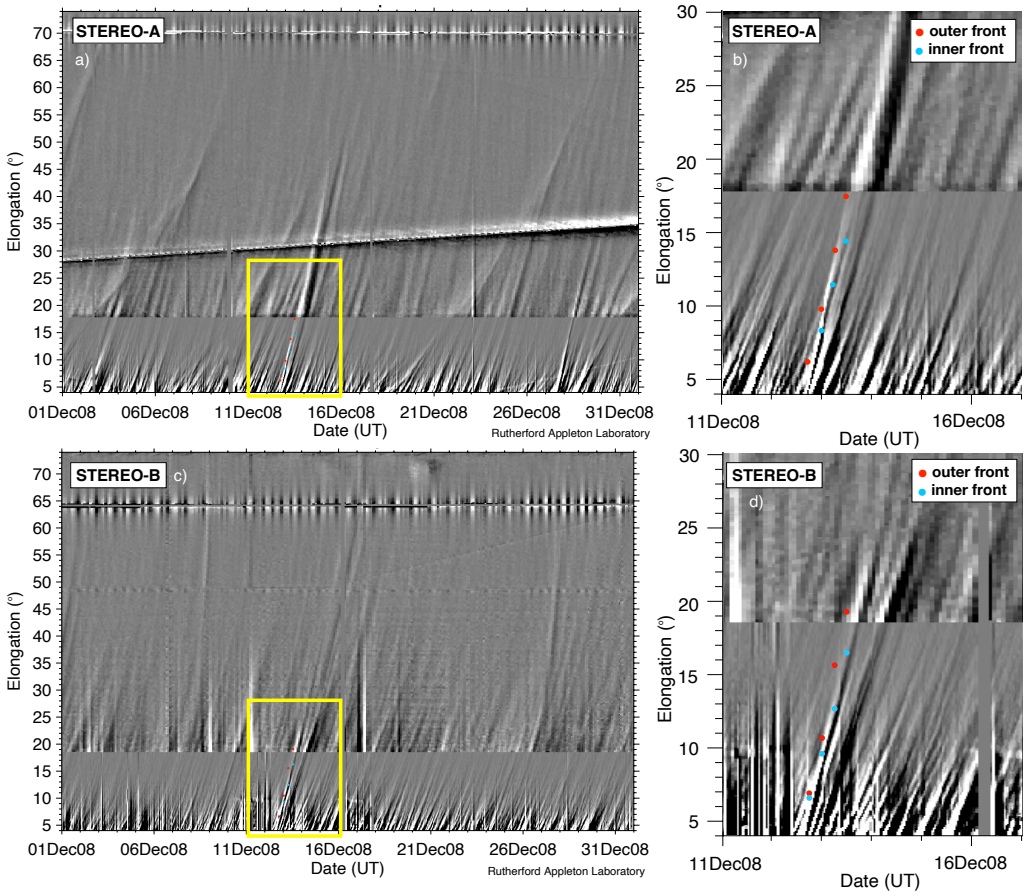

Figure 4.4: J-maps of the Heliospheric Imager field of view from the view of STEREO-A (top row) and STEREO-B (bottom row). December 2008 data is displayed in a) and c) with the time period corresponding to the CME event encased in the yellow outlined box. This time period is zoomed in for b) and d). For a number of observational time periods six hours apart, we overlay the elongation angle that was determined by the Solar Stormwatch front tracking technique for the outer front (blue dot) and inner front (red dot). J-maps were obtained from Rutherford Appleton Laboratory (`https://www.stereo.rl.ac.uk/cgi-bin/movies.pl`, accessed May 2023).

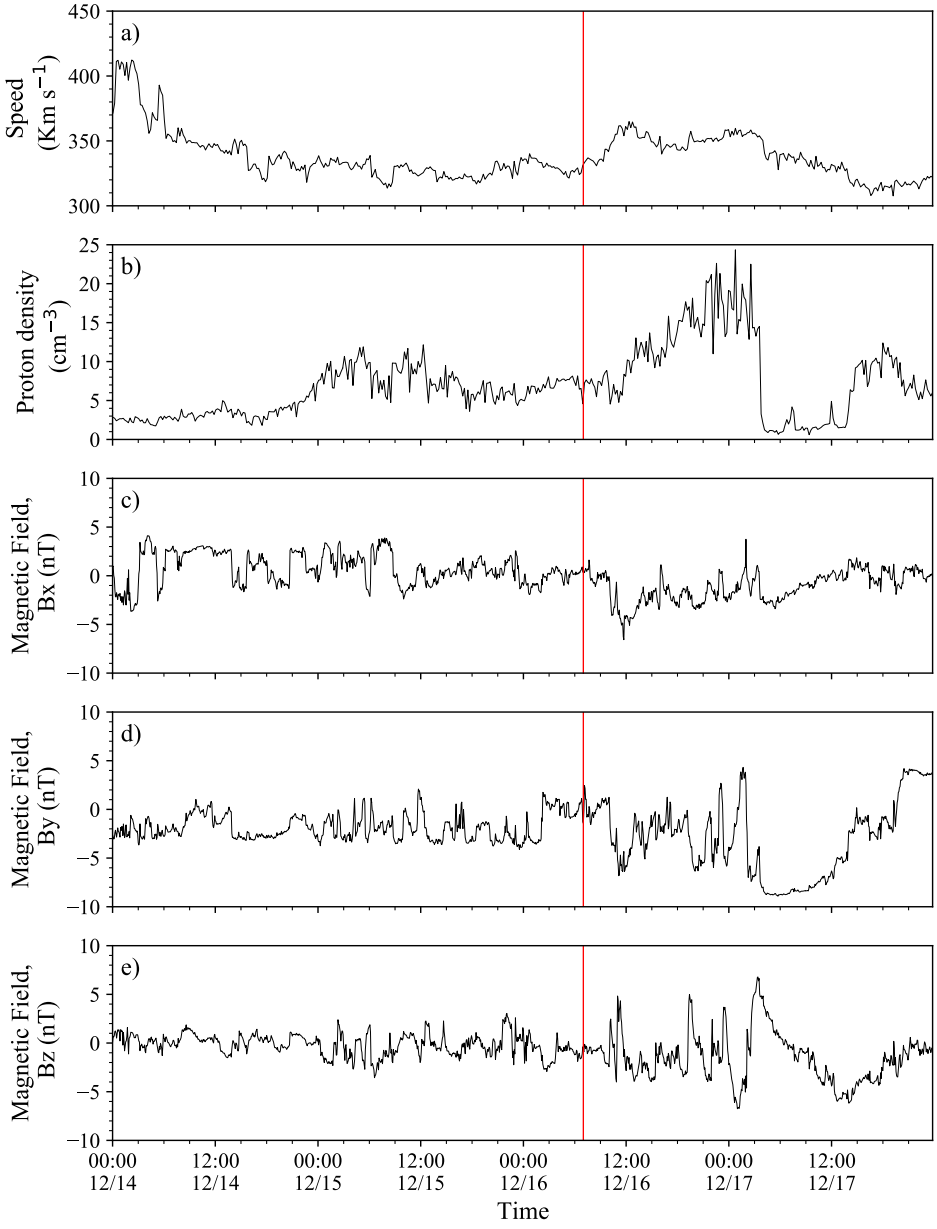

Figure 4.5: Solar wind data from NASA's ACE spacecraft from 12 - 18 December 2008. Panel a) shows the solar wind bulk speed, b) shows the proton density, and c), d) and e) shows the magnetic field in GSE coordinates. The red line indicates the arrival time of the coronal mass ejection.

clear that these features are indeed associated with a CME when, a few hours later, the magnetic field rotates - in this case southwards - indicating the arrival of the magnetic structure. This observed arrival time is consistent with other studies (*Davis et al.*, 2009; *Deforest et al.*, 2013a; *Zhang et al.*, 2019).

4.2 Method

The ghost front CME case study from December 12 2008 is simulated in the HUXt solar wind model. The CME is initialised with parameter estimates produced from analysis of COR data by *Scott et al.* (2019), listed in Table 4.1, at the inner boundary height of 30 $R_\odot$ from the Sun centre. Simulating the CME propagation through the heliosphere for six days, interactions between the varying speed from the CME and solar wind structure in the Earth's latitudinal plane are modelled from the inner boundary out to 236 $R_\odot$ / 1.1 au (i.e., beyond Earth's orbit). A plane plot from HUXt is shown in Figure 4.6.

4.2.1 Identifying leading structure

The HUXt model (Version 1.0.0) has been adapted from its community release to identify multiple features of the CME leading edge, in line with the ghost-front theory of *Scott et al.* (2019). In the projected plane, a CME body is identified as any region difference of $\geq 20\,\mathrm{km\,s^{-1}}$ when compared to the local ambient solar wind velocity. The boundary of this region is recorded at each model time step. Using the known position of the STEREO spacecraft, the elongation angle of the boundary points can be calculated using

$$\varepsilon = \arccos\left(\frac{r_o^2 + S^2 - r_f^2}{2r_o^2 \cdot S}\right), \tag{4.1}$$

where r_o is the radial distance of the spacecraft, r_f is the radial distance of the CME feature, and S is the distance between the spacecraft and CME feature.

For the ''ghost front'' theory, we are interested in tracking the flank and nose of the leading edge, where the leading edge is the outermost boundary of the region in terms of the radial distance from the Sun. In the projected plane, the point at which the leading edge intercepts the radial line of propagation is classified as the nose position. The radial line of propagation in Earth's latitudinal plane is equal to the source longitude of the CME. As we use a solar wind speed model, we are unable

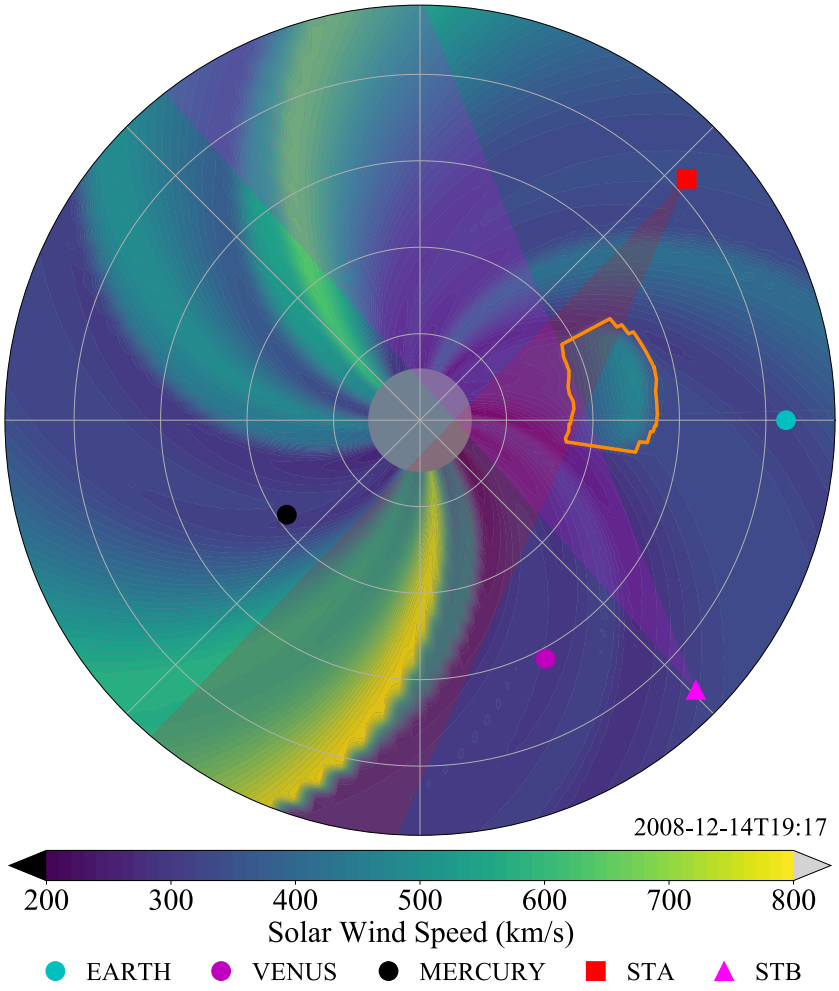

Figure 4.6: HUXt simulation in Earth's latitudinal plane, simulating the 12 December 2008 CME propagating towards Earth (cyan dot). The CME outer boundary, shown in yellow, is restricted to the grid resolution of the model. The HI1 fields of view is shown by the shaded regions extending from the two spacecraft (triangles).

to specifically identify the position of the dense plasma region in the vicinity of the CME nose which would cause the bright front in HI images, and hence use the nose position as an approximation. However, it should be noted that this could lead to a small difference in the time-elongation profile compared with tracking a dense region close to the nose. The tangent of the leading edge along the line of sight from the observer is described as the flank of the CME. Therefore, through the HUXt model, time-elongation profiles for these CME features are produced, where the elongation angle is the Sun-observer-feature angle.

Throughout the propagation, the position of the tangent will approach the nose from the far flank before switching to the flank closest to the observer at large elongations, assuming there is no extreme distortion to the CME shape. As a result, the time-elongation profiles of the nose and flank would be expected to merge at some point, and then separate again.

The modelled time-elongation profiles are compared to the position of the bright fronts in HI1 observations taken along the Sun-Earth line. By using the HI1 field of view, the maximum elongation of the CME is approximately 23°, thus, the merger of the nose and flank time-elongation profiles is not included within the considered viewing geometry. Therefore, we are confident the flank time-elongation profile identified corresponds with the furthest flank from the observer. It is worth noting a limitation of this technique; for an extreme viewing geometry where the CME is propagating away from the observer, the furthest flank is not clearly identifiable and the merger point may occur in the HI1 field of view. This is not the case for the December 2008 event considered here. To quantify the model's ability to simulate the HI1 data, the Root-Mean-Square-Error (RMSE) of each elongation profile is measured between the model and observations for each feature as a function of time. Errors for the flank and nose from both STEREO spacecraft are combined as a single error measurement to represent the total error between observations and the model run.

4.2.2 Computing ensembles of CME propagation

With HUXt's ability to compute model runs very quickly, we are able to explore the parameter uncertainties using an ensemble approach. The first study to do this, by *Barnard et al.* (2020), tracked the flank feature and compared the modelled time-elongation profiles to those in HI1 observations for four different CME events. By computing ensembles whereby the CME parameters were perturbed uniformly, since the distribution of the parameter uncertainty was unknown and for a proof-of-concept study assumed a uniform distribution, they weighted members by their skill and improved the hindcast arrival and uncertainty by a mean of $20.1\,\% \pm 4.1\,\%$ and $15.0\,\% \pm 7.2\,\%$ respectively.

A deterministic run is a single run of a model where the initial conditions are

informed by estimates of the parameter, based on observations, and ignoring the value uncertainty. It is one possible outcome of the model, but with confidence that this set of initial conditions is credible. In ensemble modelling, the parameter space of initial conditions is centralised around the deterministic run. Whilst a likely outcome, the deterministic run does not explore the sensitivity of the model to the uncertainty and accuracy of the initial conditions. In our case, the CME initial parameters have an associated uncertainty that we can explore through an ensemble which perturbs these conditions.

In the work discussed here, an ensemble comprises of 201-model runs (i.e., members); 1 deterministic member and 200 randomly perturbed members. The initial conditions varying between each member are the longitude, latitude, width, speed, and thickness of the cone CME, each varying with a random, uniform distribution from the deterministic values where the parameter space of the initial condition uncertainties are informed from coronagraph observations. Each ensemble member undergoes the above procedure to create time-elongation profiles of the flank and nose and quantifies the accuracy through comparison with HI1 observations. Thus, the ensemble members can be ranked according to RMSE to seek which members perform best. The arrival time and in-situ speed of the leading edge at L1 are also recorded for each ensemble member.

By determining the relation between RMSE and Arrival Time Error (ATE), we can determine whether the HI observations contain any information that can be used to improve the estimated arrival time at Earth. To detect if there is a gain to using the ‘‘ghost front’’ theory, we repeat the analysis of ensemble results using the flank time-elongation profiles only, similar to the work of *Barnard et al.* (2020). For this, the model performance is quantified by considering the sum of the flank RMSE from both spacecraft only.

4.2.3 Data Assimilated Solar Wind Speed

In recent years, data assimilation techniques have been developed for improving simulations of the solar wind speed. The Burger Radial Variational Data Assimilation (BRaVDA) solar wind scheme (*Lang and Owens*, 2019; *Lang et al.*, 2021) calculates an optimal inner boundary condition for a steady state simulation of the equatorial

solar wind speed, through the assimilation of in-situ solar wind observations. A perturbation of the MAS model solar wind speed solution for a single Carrington rotation is defined as the prior (initial) state at the scheme's 30 $R_\odot$ inner boundary and allowed to propagate out into the simulated heliosphere using the HUX model (*Riley and Lionello*, 2011, ; N.B. not to be confused with the time-dependent version, HUXt which we use to demonstrate CME propagation and distortion in the research). At 1 au, the solar wind speed error, in units km s^{-1}, is calculated between the model and in-situ measurements from spacecraft (e.g. ACE, STEREO). There is inherent uncertainty in the prior conditions and the observational data, assumed to be Gaussian distribution. A cost function is found for the scheme by weighting the solar wind speed error by the relative inherent uncertainty. The cost function is minimised which equates to finding the modal posterior (after assimilation) conditions. This is used to inform the ''optimum'' solar wind speed, called the posterior state, to use as inner boundary conditions. The output from BRaVDA can then be used to define a solar wind speed structure at 30 $R_\odot$ in a heliospheric model, such as HUXt (*Owens et al.*, 2020a). Use of the data assimilated scheme has been shown to reduce error in solar wind speed forecasts by 34% (*Lang et al.*, 2021). The effectiveness of using the BRaVDA scheme for CME distortion with the solar wind has been explored in this thesis.

4.2.4 Experiments

In this study, we investigate two inner boundary conditions that can be altered in HUXt which could significantly impact the outputs: the solar wind speed structure implemented at the inner boundary and the magnitude of the assumed uncertainties in the initial CME observations. By taking combinations of these inner boundary alterations, a total of three ensembles (hereafter we refer to these as experiments) are presented here:

1. CME initialised with the parameter and uncertainties estimated by observations, interacting with BRaVDA solar wind solution.

2. CME initialised with the parameter and double the uncertainties estimated by observations, interacting with BRaVDA solar wind solution.

3. CME initialised with the parameter and uncertainties estimated by observations, interacting with MAS solar wind solution.

In Table 4.2 we summarise the initial conditions of the cone CME, inner boundary solar wind scheme, and starting Carrington longitude for each experiment.

To test whether the quoted uncertainties of the coronagraph fit were adequate for capturing the breadth of potential outcomes, the cone CME initial conditions were allowed to randomly perturb with uniform distribution (1) among the estimated parameter uncertainty and (2) among twice the estimated parameter uncertainty.

Table 4.2: Overview of initial conditions variables used for each experiment. Value and uncertainty (if applicable) of the inner boundary radial distance, CME speed, CME source location, CME full width, CME thickness, Earth's Carrington longitude at the start of the experiment and the solar wind scheme are displayed.

Experiment	**Inner Boundary** ($R_\odot$)	**Speed** ($\mathrm{km\,s^{-1}}$)	**Longitude** (°)	**Latitude** (°)	**Width** (°)	**Thickness** ($R_\odot$)	**Earth's Carrington Longitude**	**Solar Wind solution**
1	30	497 ± 63	10 ± 4	9 ± 2	42 ± 6	5 ± 2	67.966	BRaVDA
2	30	497 ± 126	10 ± 8	9 ± 4	42 ± 12	5 ± 4	67.966	BRaVDA
3	30	497 ± 63	10 ± 4	9 ± 2	42 ± 6	5 ± 2	67.966	MAS

4.3 Reproducing HI-1 time-elongation profiles

Firstly, we assess the plausibility of multiple enhanced, similarly shaped plasma regions being explained by ghost front theory by analysing how the time-elongation profiles of the nose and flank, as seen from both STEREO spacecraft, compare with the model. In Figure 4.7 we show the model outcomes for the deterministic run with the elongation profile of the CME nose being shown as a solid line and that of the flank being shown as a dashed line. The simulated STEREO-A time-elongation profiles are in good agreement with the observations, especially the nose feature which traces the observations within the uncertainties of most data points. This pair of features has an RMSE of 0.68°. The simulated STEREO-B time-elongation profiles do not trace the observations as well. Instead, the nose and flank profiles are close together, separated by approximately 0.5°, and both fall between the elongation profiles of the inner and outer fronts seen in HI images. Early in the model run,

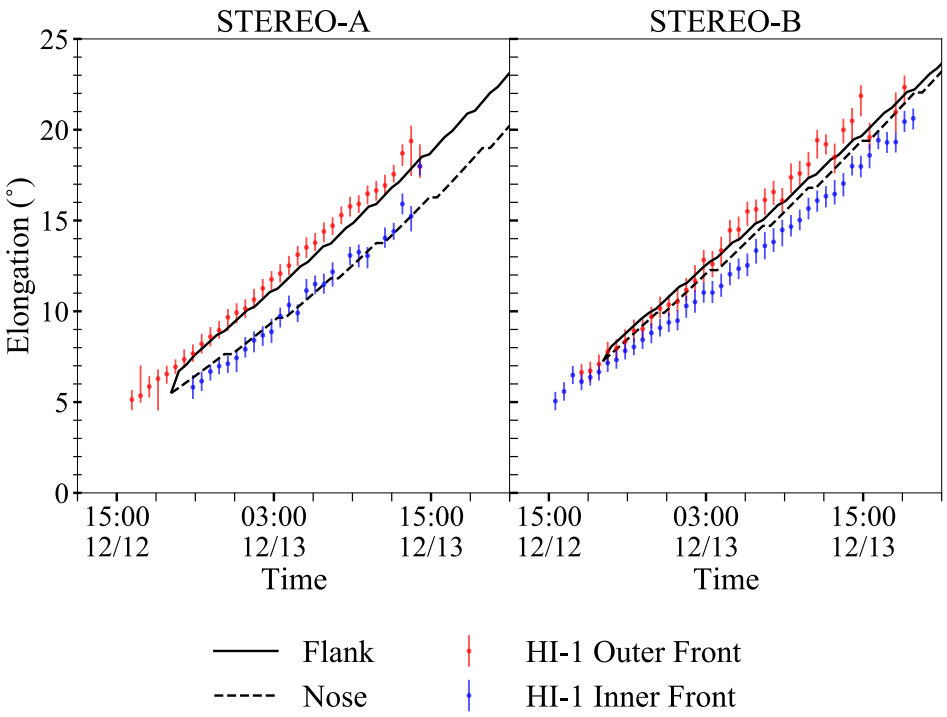

Figure 4.7: The modelled time-elongation profiles of the leading edge nose (solid line) and flank (dashed line) from the deterministic run. Features are tracked from the perspective of STEREO-A on the left and STEREO-B on the right. Elongations gained from STEREO HI-1 observations are shown by coloured error bars, replicated from Figure 4.3.

where the uncertainty of the observed nose and flank positions converge, we can see a reasonable model performance. But with time this worsens, with the exception of a few coincident data points. The RMSE error for the STEREO-B profiles is 0.92°. For both STEREO spacecraft, the deterministic run has an RMSE value of 0.83°.

We know that the initial parameters have uncertainties. By modelling as an ensemble, and taking these uncertainties into account, the observations can be better represented. By ranking the RMSE values of each member in order to find the lowest RMSE, we show the best-fit to the observation in Figure 4.8. We can only see small adjustments to the time-elongation profiles. From the STEREO-A perspective, both features continue to agree with the observations, producing an RMSE of 0.60°. The flank profile tracks the observation data within the majority of the uncertainties. Meanwhile, the nose traces the gradient of the observation and coincides with the upper range of uncertainties from about 03:00 UTC on 13 December 2008. Whilst marginally less well-fit than the deterministic run, the difference is not detrimental

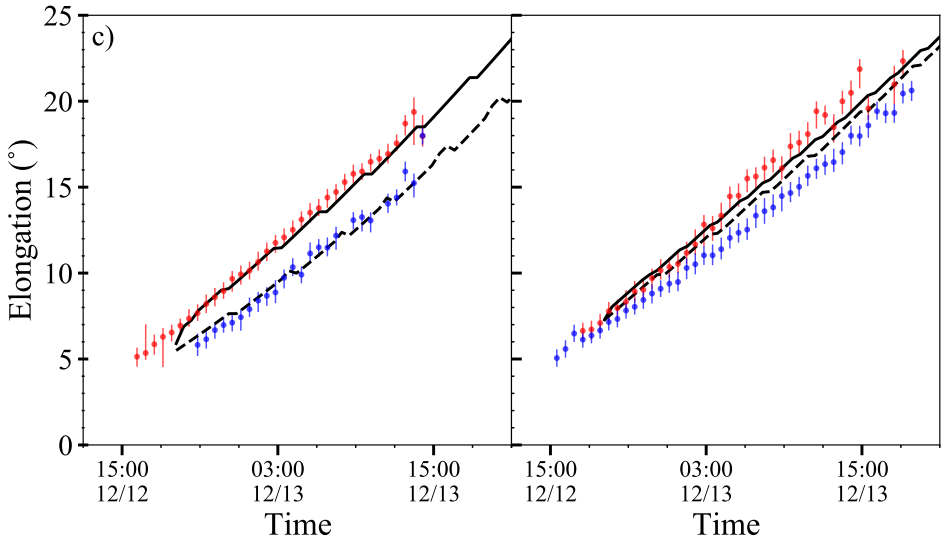

Figure 4.8: The modelled time-elongation profiles of the leading edge nose (solid line) and flank (dashed line) that produce the lowest root-mean-square-error in Ensemble 1. Features are tracked from the perspective of STEREO-A on the left and STEREO-B on the right. Observations from STEREO HI-1 camera are shown by coloured error bar, replicated from figure 4.3

to the model performance. On the other hand, from the STEREO-B perspective, the separation between the nose and flank is greater than the previous profiles, now approximately 1.0°, as the nose profile follows the upper limit uncertainty of the observations. As a result, we get an RMSE of 0.75° for this pair of features. By taking both spacecraft perspectives into account, the model member has an RMSE of 0.69° which is the lowest error value produced from Experiment 1.

Despite the best-fit model run agreeing with the HI observations better than the deterministic run, we find that we obtain an arrival time that is 2 hours 18 minutes earlier and hence falls outside the observed arrival uncertainty of 1 hour. Such a result demonstrates the limitation of using HI time-elongation profiles to constrain a CME's evolution as they are essentially degenerate for many combinations of initial CME parameters. The ''best fit'' time-elongation profile might correspond to a simulation that poorly reflects the arrival time at Earth. Further, due to the random nature of the sampling, identifying the experiment member that produces the lowest RMSE may not be representative of the entire ensemble, and as such it is not sufficient to use this to draw conclusions on the benefit of using ghost fronts to constrain propagation modelling. However, we have shown that the position of

the leading edge flank and nose compare well with the location of the bright, dense plasma regions captured in the HI observations. This highlights that a measure of model performance can be used to infer the longitudinal distortion of a CME.

The narrow separation between the modelled nose and flank time-elongation profiles from STEREO-B's perspective suggests that the HUXt model is not accurately capturing the CME distortion. The radius of the curvature of the CME front is too small such that the flank cannot be modelled at the elongation required to match the observations. This could be a limitation of the CME cone model, in particular the half-width parameter, or the solar wind speed in the vicinity of the flank is not great enough to cause significant distortion to the modelled CME boundary. Another explanation is that the parameter uncertainties produced from the reconstruction of COR data covers an insufficient range over which the initial parameters of the CME were allowed to vary in the ensemble. We test the latter in Experiment 2 by doubling the range over which the CME initial conditions are allowed to vary.

4.4 Representing structured solar wind: BRaVDA or MAS?

Before exploring how we can use the HI observations, model RMSE values and the arrival estimates of the CME, we first investigate how the use of data assimilated solar wind structure within the HUXt model influences the results. Below we discuss how estimates of the solar wind for CR2077 were produced, then compare the speed profiles at L1 with those from the non-data assimilated solar wind model and real observations. We then use the deterministic CME conditions to evaluate the difference in model outcomes.

4.4.1 Solar wind structure

Data assimilation requires observational data to train the model to find ''optimal'' solutions. In this study, *Advanced Composition Explorer* (ACE) is used to provide solar wind speed observations. Whilst multi-spacecraft observations are generally desirable to improve the accuracy of BRaVDA's data assimilation (*Turner et al.*, 2021), in this scenario, STEREO-A and STEREO-B observations were not used due to notable differences in the solar wind structures that are likely the result of differences

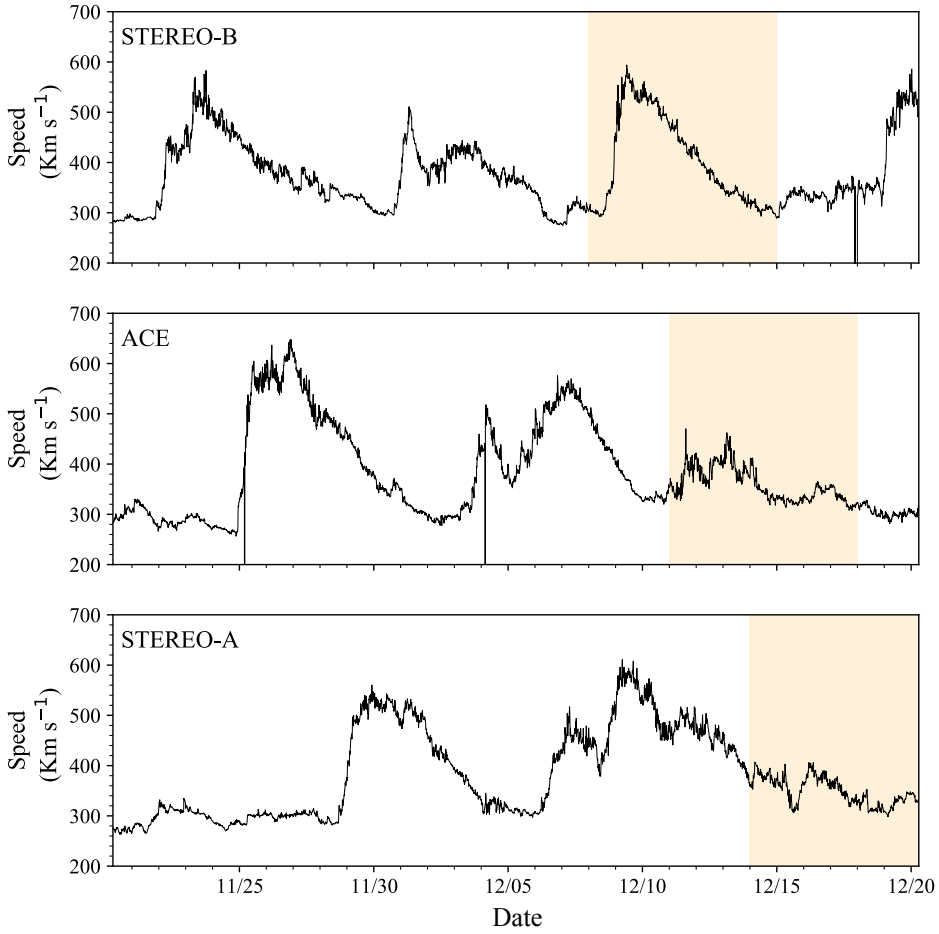

Figure 4.9: Time series of solar wind speed measured in-situ at STEREO-A, ACE and STEREO-B for a month beginning with the start of CR2077 (20 November 2008 07:00 UTC) and ending on 20 December 2008 07:00 UTC. Shaded orange regions indicate the period of the relatively high-latitude local structure observed by STEREO-B (approximately 4.9° latitude, compared to 0.7° and −5.4° latitude for ACE and STEREO-A respectively) and the corresponding time period with solar rotation lag for the other spacecraft.

between the heliographic latitudes of the three spacecraft. Throughout the time frame of this CME event, the latitudinal position of ACE is near the helio-equator (0.7°), whilst STEREO-A was below (−5.4°) and STEREO-B is above (4.9°). A fast stream was measured by STEREO-B but no evidence of this structure is present in ACE or STEREO-A data, as shown in Figure 4.9. Thus, this local structure suggests large differences in solar wind structure over relatively small latitudinal ranges about the helio-equator, an issue common during solar minimum (*Owens et al.*, 2020b). Instead, in-situ data from ACE between 360° and 90° Carrington longitude (i.e., a

full Carrington rotation excluding the time at which the CME interacted with the spacecraft) was used in the assimilation. Figure 4.10 shows the time-series of solar wind speeds at L1 produced by HUXt initialised with the non-data assimilated MAS solar wind conditions (MAS-HUXt) and the data assimilated solar wind conditions (BRaVDA-HUXt), compared with real observations from the ACE spacecraft. Both model outputs produce peaks at the same periods seen in the observation, however, BRaVDA is shown to be better at not overestimating the speed or creating extra peaks. This is most noticeable on 3 December 2008. In the MAS-informed HUXt run we note the overestimated peak in speed on 13 December 2008 corresponding to the high-latitude fast steam structure that was identified to only occur in STEREO-B data.

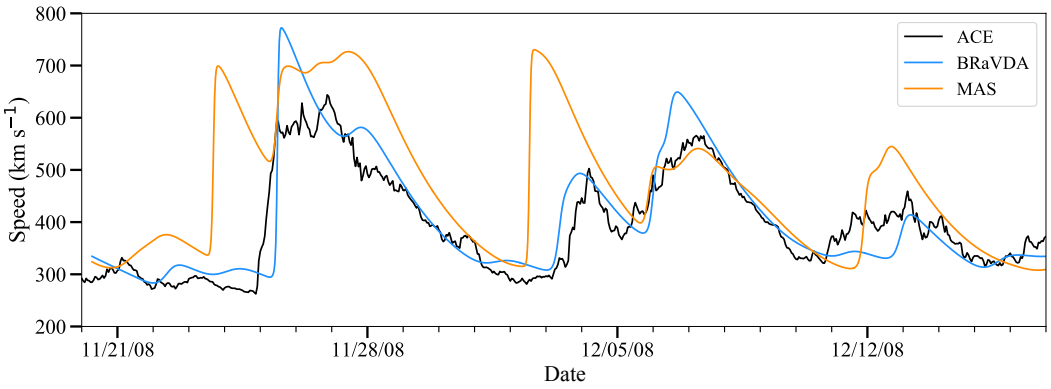

Figure 4.10: Time series of solar wind speed at L1 for real ACE data (black) and HUXt model output initialised at 30 $R_\odot$ with a non-data assimilated solar wind scheme (MAS; orange) and a data assimilated solar wind scheme (BRaVDA; blue). Date ticks correspond to 00:00 UTC.

4.4.2 Comparison of CME distortion

By comparison of the deterministic MAS-HUXt and BRaVDA-HUXt runs, the analysis is expanded to explore the impact the solar wind speed schemes have on a CME distortion. From the 30 $R_\odot$ inner boundary, the CME interacts with the solar wind streams continuously throughout the simulation. Figure 4.11 shows the CME after it has undergone 24 h of distortions in Earth's latitudinal plane along with the modelled time-elongation profiles of the nose and flank features compared with observations through the HI1 field of view.

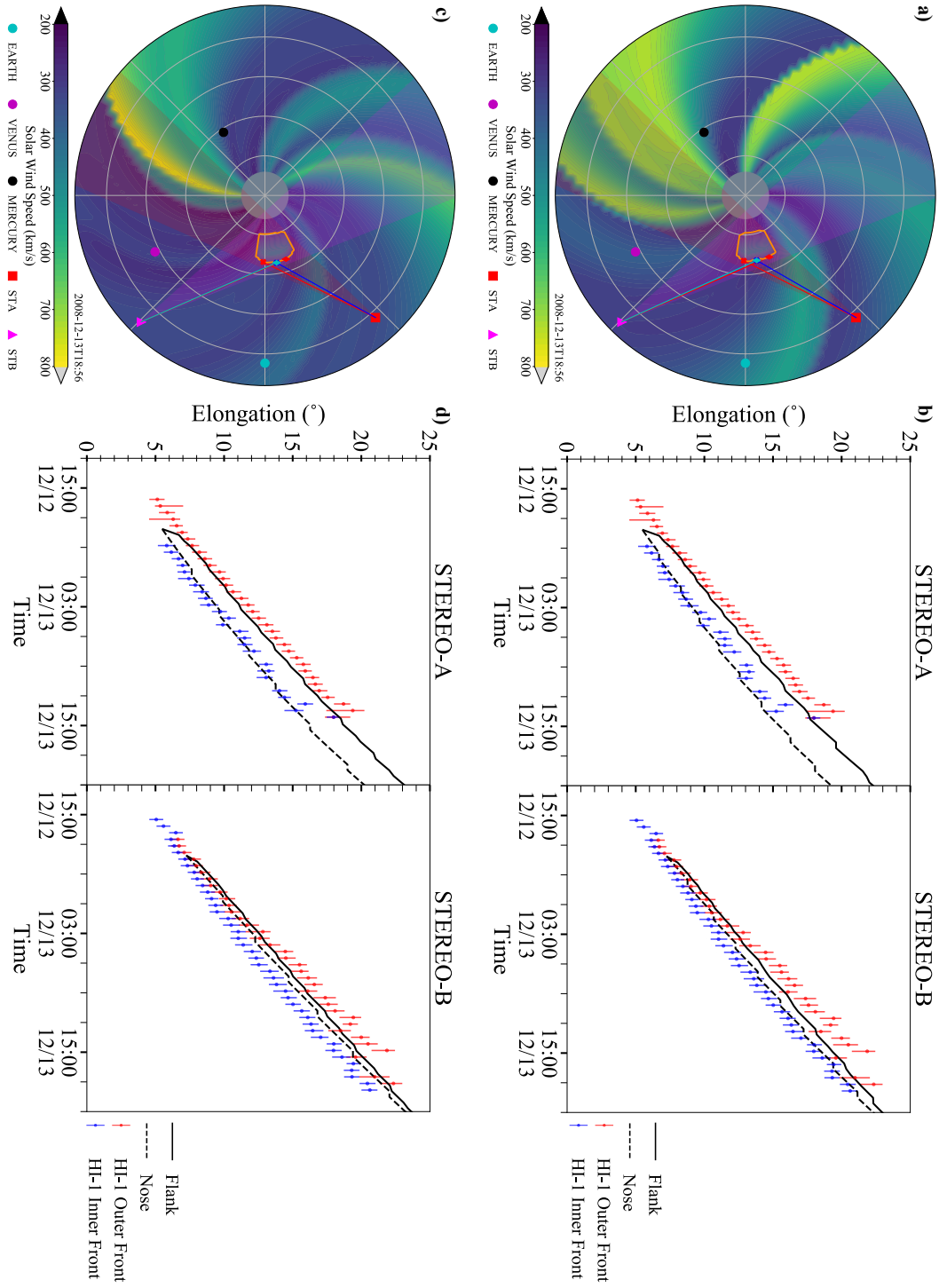
a)
b)
c)
d)
Solar Wind Speed (km/s)
200
300
400
500
600
700
800
2008-12-13T18:56
EARTH
VENUS
MERCURY
STA
STB
STEREO-A
STEREO-B
Elongation (°)
Time
15:00
12/12
03:00
12/13
15:00
12/13
Flank
Nose
HI-1 Outer Front
HI-1 Inner Front

Figure 4.11: Comparison of HUXt output when run with different inner boundary solar wind conditions. The top panel shows the MAS non-data assimilated solar wind scheme results. The bottom panel shows the BRaVDA data assimilated solar wind scheme results. The 24-hour solution in Earth's latitudinal plane is displayed in a) and c), showing the CME interaction with the solar wind structure. The structured solar wind is shown by the background colour, whilst the CME edge is identified by the orange-outlined shape. The HI1 field of view is marked as a translucent, triangular-shaded region expanding from the spacecraft. For this timestamp, the nose position is indicated by the blue cross/cyan diamond whilst the flank position is marked by the red cross/ red diamond along the CME leading edge. Markers for Earth, STEREO, Venus, and Mercury positions are also included. b) and d) show time-elongation plots measured from the position of STEREO-A and STEREO-B for the leading edge nose (black dashed) and flank (black solid) throughout the HI1 field of view. HI1 observations are shown by coloured error bars.

In the top row, we see the MAS-HUXt case. For this non-data assimilated solution, we find that the time-elongation profile of the nose and flank throughout the HI1 field of view agree well with STEREO-A and STEREO-B observations, obtaining an RMSE of 0.91° and 0.81° respectively. The combined RMSE from both spacecraft is 0.86°. In the bottom row, we show the BRaVDA-HUXt case, and similarly, the time-elongation profiles also fit well with the observations. For this case, we obtain an RMSE value of 0.68° for STEREO-A (25 % lower), 0.93° for STEREO-B (14 % higher), and 0.83° or both spacecraft (3 % lower). The improvement in recreating STEREO-A observations but not STEREO-B in the latter case can be explained by the leading edge distortion seen in the HUXt plane plots. Both model runs were initialised with the same CME parameters from a $30\,R_\odot$ inner boundary, therefore, these variations are due to the differences in solar wind speed.

In the BRaVDA-HUXt run we find the CME has maintained a similar curved leading edge structure to its initialised state. The ambient solar wind on the eastern side of the CME is distorting the CME with a slightly faster stream than its non-DA counterpart and, as a result, we see the nose at a greater radial distance at this given time. Therefore, from the viewpoint of both STEREO spacecraft, we measure greater elongations at each time step, producing a profile series with a greater gradient. This is visible in Figure 4.11e and f as the nose profiles agree with more data points in the STEREO-A HI1 field of view and produces a lower RMSE, whilst STEREO-B

agrees less well. Accordingly, we find this large difference in the quantified error.

In contrast, the MAS-HUXt run causes the western flank of the CME to be dragged forward with the fast stream creating a flatter leading edge. This impacts the time-elongation profiles seen from STEREO-B whereby the flank will obtain greater elongation measurements than the nose, especially later in the time series, as seen in Figure 4.11b. This improves the fit to the observations, resulting in a lower RMSE for STEREO-B. However, earlier we noted that this fast stream seen in the MAS solar wind speed solution is due to a high-latitude fast stream which was not measured by ACE and, therefore, likely less representative of the case study when we are modelling in Earth's latitudinal plane. Despite this, it highlights the importance of understanding CME distortion caused by interaction with solar wind streams for accurately reproducing HI1 observations.

From these results, we choose to only use the BRaVDA scheme to inform the HUXt model inner boundary speed conditions for the ensemble experiments. To support this, we find the hindcast arrival at L1 for the CME in both model runs. For the MAS-HUXt, the CME arrives at 12:30 UTC $\pm$ 34 min on 16 December 2008 (5.5 h after observed arrival) with a speed of 328 km s^{-1}. Meanwhile, for BRaVDA-HUXt the CME arrives at 07:53 UTC $\pm$ 34 min on 16 December 2008 with a speed of 353 km s^{-1}. Only the data assimilated scheme produces a hindcast that falls within the observation uncertainty of the CME arrival time (07:00 UTC $\pm$ 1 hour) and approximate arrival speed of 370 km s^{-1} as seen in Figure 4.5

4.5 HI-1 fitting and CME arrival predictions

Earlier we discussed that identifying a single member from the ensemble was not a useful method to analyse our CME hindcast performance since time-elongation profiles were degenerate for many combinations of initial CME parameters. In fact, due to the random nature of the sampling, identifying the experiment member that produces the lowest RMSE may not be representative of the entire ensemble, and as such it is not sufficient to use this to draw conclusions on the benefit of using ghost fronts to constrain propagation modelling. Hence, we now explore if there is a relationship between the RMSE of time-elongation profiles and the L1 arrival predictions.

Arrival time error (ATE) is measured as the difference between the observed CME arrival time and the model run's hindcast such that a negative time error corresponds with an early CME arrival and a positive time error corresponds with a late CME arrival. To ensure we investigate the impact of using multiple fronts to constrain the model, we identify a subset of data to represent the members that agree best with the HI1 observations across the range of arrival time. To do this, we bin the members by their ATE with 34-minute resolution (HUXt's output time-step in the configuration of this study) and the lowest 25 % of data points per bin are identified and fitted with a quadratic curve of best fit. This percentage appears adequate at identifying the ensemble runs which best represent the observations in each bin, whilst ensuring low-populated bins are still represented. As a result, we identify the relationship between RMSE and ATE over the whole data range. An example of the fitting technique is shown in Figure 4.12, with a red dashed line indicating the best fit to the subset of data. The results of this plot are discussed in the next section. The ATE that corresponds to the curve minimum is assigned as the ensemble arrival time estimate. The uncertainty of the ensemble ATE is defined as the bin range that lies below a threshold RMSE that is significantly different from the RMSE at the local minima. This threshold is calculated by finding the standard error of the the quadratic coefficients, by using a coefficient correlation matrix, and including the uncertainty in the curve equation to find the maximum "y-value" (i.e., RMSE value) obtained from the curve minimum (i.e., ensemble ATE). The range in RMSE values corresponding to every ATE bin value is also calculated and the full RMSE range must be greater than the threshold to not be considered in the ensemble ATE uncertainty. In such a way, curves with a sharply defined minimum will have a low uncertainty whilst curves with shallower minima have greater uncertainty. This method does not quantify the error associated with each ensemble member model run as a single value like the mean absolute error (*Verbeke et al.*, 2019), but it allows us to evaluate if constraining the model using HI1 data produces a viable estimate. In this way, we can explore the variation of best-fit RMSE as a function of arrival time while accounting for the noise generated by random sampling of the CME initial conditions. Upon calculating the minimum value of the curve we can analyse the relationship between the quality of fit and the arrival time at L1.

4.5.1 Arrival time

We note the appearance of vertical separation between two data ‘‘clusters’’ for Experiment 1 (Figure 4.12a), one which is highlighted by the subset of data and the other by the excluded ensemble data. This is only a visual identification, therefore we use the term ‘‘cluster’’ loosely to describe an apparent subset of data. It is considered future work to explore if there is a cause to the vertical separation. A likely explanation is that there is a common sensitivity to one of the initial CME values between these model runs. For example, a wider (or narrower) CME can produce flank time-elongation profiles that are offset from the observations by a few degrees and increasing the RMSE evaluation. Both clusters have similar RMSE vs ATE curves and appear to form a local minimum at similar arrival time error. In the scenario detailed above, a wide CME would not necessarily alter the elongation profile of the nose and, hence, still produces an plausible L1 arrival time. Furthermore, it is possible the cluster would be apparent in Experiment 2 if the resolution of the parameter space was consistent with Experiment 1 rather than it being doubled. By

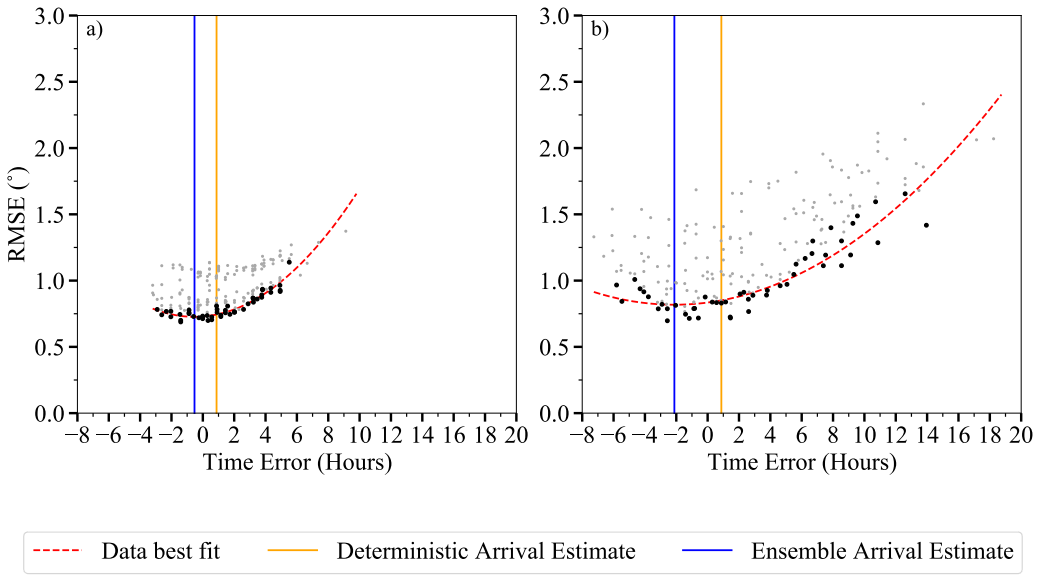

Figure 4.12: Scatter plots of time-elongation profile RMSE values against arrival time error for each model member. In these experiments, HUXt is configured with an inner boundary of 30 $R_\odot$ with initial conditions allowed to vary with (a) the coronagraph estimated uncertainty and (b) twice the estimated uncertainty. A quadratic line of best fit (red, dashed) is fit to the lowest 25 % of data per time error bin (black dots).

finding a subset of ensemble members which identify the members with the lowest RMSE value, we can ensure that we only consider those ensemble members that best match with the HI1 data.

For Experiment 1, the scatter produces a curve minimising at $-0.5\,\mathrm{h} \pm 0.2\,\mathrm{h}$ which equates to an arrival time before the observed arrival. This is within the observed arrival uncertainty of $\pm 1.0\,\mathrm{h}$. The result is 1.5 h before the deterministic hindcast, but since this is only a difference of three model resolution time-steps we cannot say that this is a strong improvement on the deterministic hindcast. The RMSE value associated with the curve minimum is 0.73°.

We next carry out the same analysis for Experiment 2, where the ensemble of CME parameters is generated by randomly sampling from uniform distributions with twice the spread of Experiment 1. We find that the RMSE variation minimises at $-2.1\,\mathrm{h} \pm 0.5\,\mathrm{h}$. This result produces a less accurate arrival time than both the deterministic and Experiment 1 model runs, which is corroborated by an increased RMSE value of 0.82° at the minima. From increasing the initial parameter range and maintaining the ensemble size, we note that there is a reduced resolution within the parameter space which may increase the variation in RMSE values between ensemble members. If an ensemble size was large enough, it could be said that Experiments 1 and 2 would find the same local minima. In application, this can be tricky to do as more model runs equate to additional computing time and resources. In a simplified physics model, such as HUXt, then adding more members is feasible if the computer allows it. With complex models then large member ensembles are not feasible and, hence, we see operational forecasts use a small number of runs in their ensemble models. As such, we do not desire to increase the number of models runs to ensure the conclusions are the same. We conclude that there is no evidence to support doubling the coronagraph uncertainty estimates in the ensemble initial conditions.

Tracking only the flank position

If only the flank time-elongation profile (i.e. the outermost CME front detected in HI) is considered, as was done in the work by *Barnard et al.* (2020), we find that the quadratic curve minimises at $-4.4\,\mathrm{h} \pm 1.1\,\mathrm{h}$ with RMSE of 0.90° for Experiment 1 and $-11.1\,\mathrm{h} \pm 4.9\,\mathrm{h}$ with RMSE of 0.70° for Experiment 2, as seen in Figure 4.13.

An early CME arrival time is inline with the results obtained when using both ghost front features to assess the model performance, but it is noted that the ATE values gained when tracking the flank only fall outside of the range of values obtained by all the ensemble members (the minimum ATE for Experiment 1 is 03:48 UTC 16 December 2008 and the minimum ATE for Experiment 2 is 23:44 UTC 15 December 2008 respectively), highlighting that the outcomes are unreliable estimates. Thus far in the case study, an early CME arrival is estimated when launched from an initial height of 30 $R_{\odot}$, but the accuracy of the ATE estimate is improved when including CME nose tracking in ensemble modelling. By the method developed, the arrival time of a CME launched from an initial height of 30 $R_{\odot}$ can only be estimated when using the ghost front features to constrain the model .

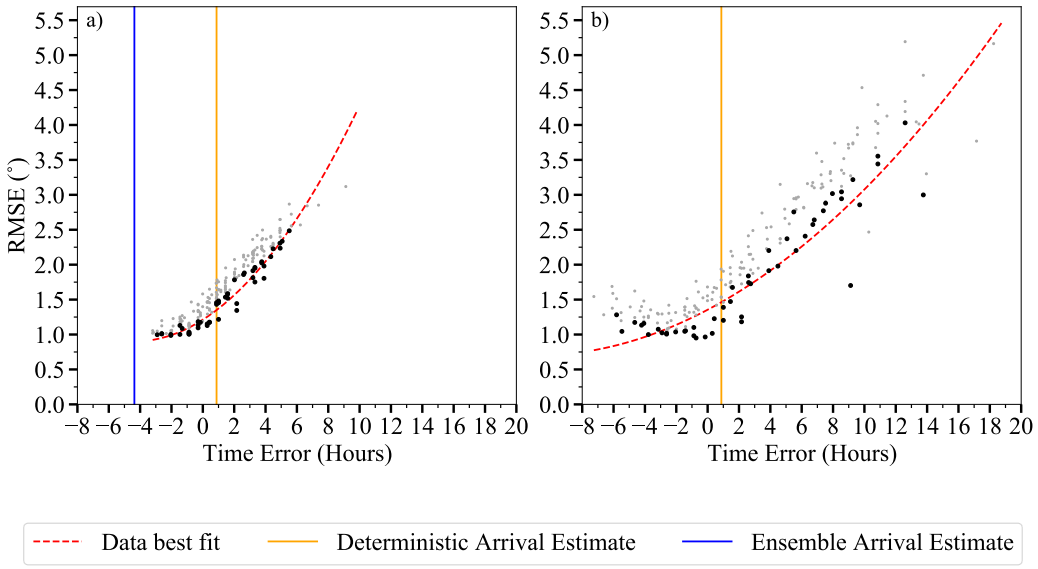

Figure 4.13: Root-Mean-Square-Error of the flank only in HI1 field of view against the Arrival Time Error (ATE) of the CME leading edge at L1, using BRaVDA-HUXt initialised from 30 $R_{\odot}$. Scatter plots of the flank time-elongation profile RMSE values against arrival time error for each model member. In these experiments, HUXt is configured with an inner boundary of 30 $R_{\odot}$ with initial conditions allowed to vary with (a) the coronagraph estimated uncertainty and (b) twice the estimated uncertainty. A quadratic line of best fit (red, dashed) is fit to the lowest 25 % of data per time error bin (black dots).

4.5.2 Arrival speed

The analysis is repeated for the arrival speed of the CME at L1. From in-situ measurements, the arrival speed of the CME at Earth was $333\,\mathrm{km\,s^{-1}} \pm 15\,\mathrm{km\,s^{-1}}$, corresponding to the estimated arrival of 07:00 UT on 16 December 2008. The error of each ensemble member's estimated speed at L1 is found, and labelled as the Arrival Speed Error (ASE). A positive ASE value indicates the speed is faster than observed, whilst a negative ASE value indicates a slower speed than observed. The ASE values are compared to the RMSE of HI1 time-elongation profiles. A quadratic curve of best fit is found for the lowest 25 % of binned data and the ASE corresponding to the position of the curve minimum is allocated as the ensemble ASE. In Figure 4.14, the results are shown for Experiments 1 and 2.

Experiment 1 estimates an ensemble ASE of $5.9\,\mathrm{km\,s^{-1}} \pm 3.0\,\mathrm{km\,s^{-1}}$, performing better than the arrival speed produced by the deterministic run by $14.1\,\mathrm{km\,s^{-1}}$. The ensemble ASE is close to the speed range minimum of $5.0\,\mathrm{km\,s^{-1}} \pm 5.3\,\mathrm{km\,s^{-1}}$. An ensemble resulting in a wider range of arrival speeds would enable better charac-

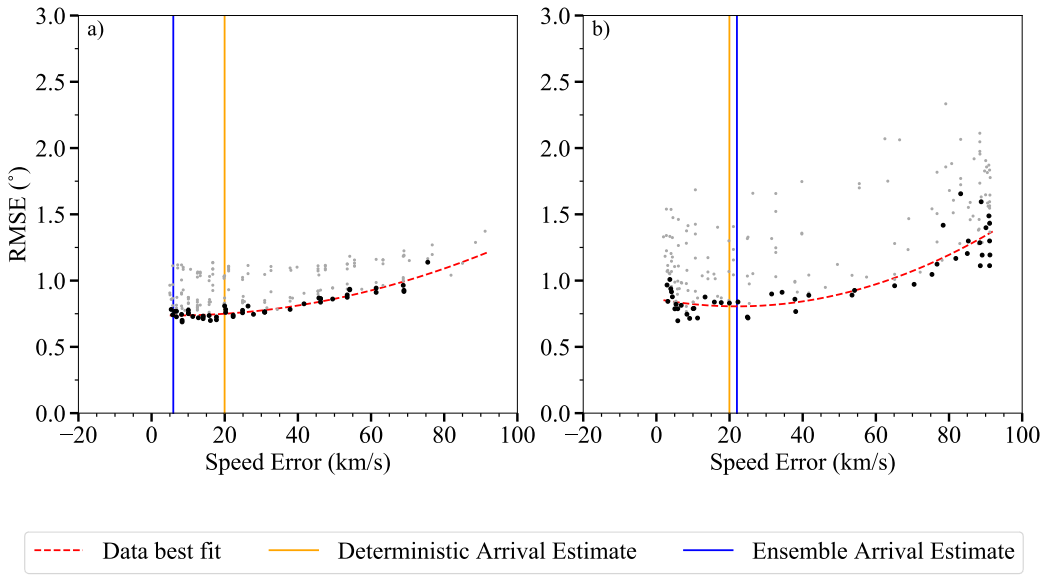

Figure 4.14: Scatter plots of time-elongation profile RMSE values against arrival speed error for each model member. In these experiments, HUXt is configured with an inner boundary of $30\,R_\odot$ with initial conditions allowed to vary with (a) the coronagraph estimated uncertainty and (b) twice the estimated uncertainty. A quadratic line of best fit (red, dashed) is fit to the lowest 25 % of data per bin (black dots).

terisation of the uncertainty of the quantity. Meanwhile, for Experiment 2, the fit minimises at $22.0\,\mathrm{km\,s^{-1}} \pm 8.5\,\mathrm{km\,s^{-1}}$ which is very similar to the deterministic value. With respect to the high speeds of CMEs, an error of this magnitude is not significant. Since the CME was estimated to have a radial speed similar to the ambient solar wind, it is unsurprising that the results are close to the in-situ speed observed by ACE.

Despite the increase in parameter space for which the cone CME initial conditions can vary, the range of L1 speed for the model members is similar for both experiments. All members estimate an arrival speed greater than observed, suggesting a bias in the BRaVDA-HUXt model or that the observed arrival speed obtained from spacecraft measurements may not be associated with the CME event.

Tracking only the flank position

This analysis was also applied to the HI1 time elongation profiles of the flank only. This is shown in Figure 4.15. In Experiment 1, a negative quadratic curve is found to fit the data whereby the lowest RMSE values correspond to ASE values between $5\,\mathrm{km\,s^{-1}}$ to $10\,\mathrm{km\,s^{-1}}$ and as the ASE value increase then so does the RMSE value at a decreasing rate. This trend finds a maximum point at $350\,\mathrm{km\,s^{-1}}$, but since

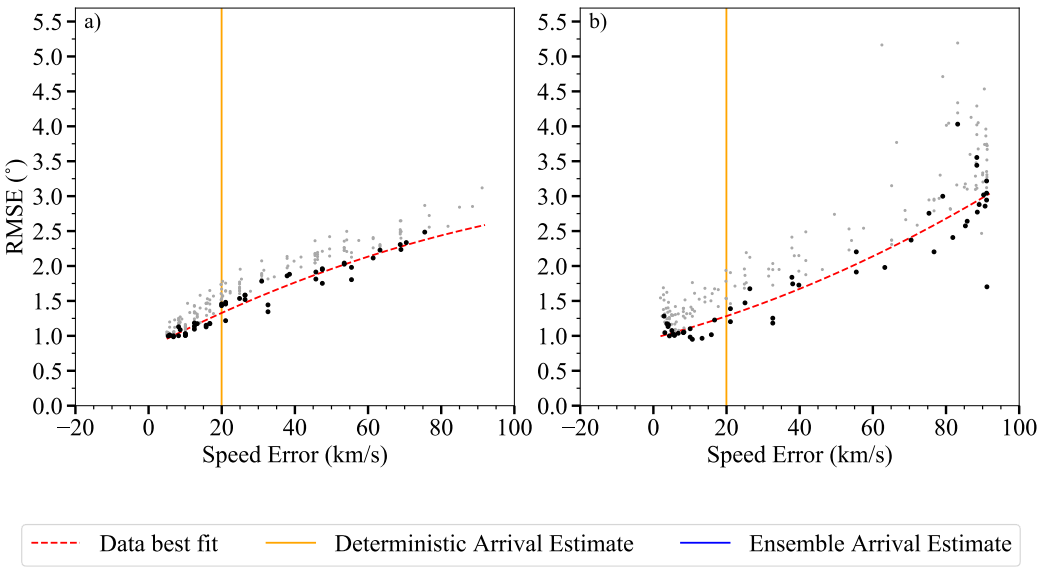

Figure 4.15: Root-Mean-Square-Error of the flank only in HI1 field of view against the Arrival Speed Error (ASE) of the CME leading edge at L1, using BRaVDA-HUXt initialised from $30\,R_\odot$.

this estimate is outside the ensemble range it is considered an invalid estimate. In Experiment 2, a positive quadratic gradient best describes the data but continued to show that the RMSE value increased with an increase in ASE. As such, a minimum to the quadratic fit is found at $-74.2\,\mathrm{km\,s^{-1}} \pm 72.1\,\mathrm{km\,s^{-1}}$. Although with the consideration of the estimate uncertainty a near-true arrival speed is possible for the case study, the estimate falls outside the ensemble range and consequently is an invalid estimate. Based on these results, it cannot be suggested that tracking the flank alone is suitable for the method. Estimating arrival speed based on the trajectory of the CME flank in HI1 observations from ensemble modelling requires further work to understand the plausibility of extending this technique.

Table 4.3: Summary of the estimated arrival time error and arrival speed error from minimising the correlation between ensemble RMSE and arrival errors. Values in italics are noted as estimates that fall outside the ensemble range. An uncertainty of *NaN* means that it is not applicable. This is because the deterministic run produces one value and there is no finite resolution of the measurement.

Experiment	**Arrival Time Error** (hours)			**Arrival Speed Error** ($\mathrm{km\,s^{-1}}$)		
	Deterministic	Ghost Front Features	Flank only	Deterministic	Ghost Front Features	Flank only
1	0.9 ± 0.6	- 0.5 ± 0.2	*-4.4 ± 1.1*	20 ± NaN	5.9 ± 3.0	*350.7 ± NaN*
2	0.9 ± 0.6	-2.1 ± 0.5	*-11.1 ± 4.9*	20 ± NaN	22.0 ± 8.5	-74.2 ± 72.1
5	5.5 ± 0.6	*-1.9 ± 2.7*	*-5.6 ± 6.4*	-5 ± NaN	*227.3 ± 226.5*	*180.4 ± NaN*

4.6 Summary

In this chapter, the HUXt solar wind model has been used to simulate time-elongation profiles of the CME nose and flank from the observing position of spacecraft away from the Sun-Earth line. Using the 12 December 2008 CME as a case study, the STEREO spacecraft captured the CME propagating Earth-wards through the HI cameras. Analysis of the running-difference HI images shows two bright fronts similar in latitudinal structure but separated by a few degrees in elongation. These, if interpreted using the ghost front theory (*Scott et al.*, 2019), corresponded to the position of the CME nose and the CME flank furthest from the observer in the HI1

field of view.

In the work, the HUXt model simulates the radial outflow of solar wind speed in Earth's latitudinal plane driven by the solar wind structure at the inner boundary. Data assimilated solar wind speed, computed with the BRaVDA scheme, significantly improve estimates of the transit time of the CME from the inner boundary to L1 in comparison to the MAS solution. The BRaVDA scheme has the flexibility to use specific spacecraft and time periods such that the influence of non-helioequator fast streams on the solar wind speed solution can be limited, as has been done here.

Despite a single run producing a model outcome that is in fair agreement with HI1 and L1 in-situ observations, the result is degenerate and provides no estimate of uncertainties of CME arrival time and speed at Earth. Thus, ensemble modelling is used to explore the parameter uncertainty in inner boundary cone CME conditions. An additional 200 model runs, with CME initial conditions varying with a uniform, random distribution from the deterministic values, create the ensemble. Three ensembles were carried out: two BRaVDA-HUXt experiments (one that allowed initial CME conditions to vary within the uncertainty of the coronagraph CME reconstruction parameters and another that allowed double the uncertainty) and one MAS-HUXt experiment (using the coronagraph CME reconstruction parameter uncertainties). By assuming there is value in quantifying model performance through comparison with HI observations, as was concluded in this chapter and in other literature (*Barnard et al.*, 2020; *Chi et al.*, 2021; *Harrison et al.*, 2017), a quadratic correlation between the root-mean-square-error fit is found between the HI1 time-elongation profiles and the L1 arrival time error of each member. From this, an estimated ensemble arrival time error is produced for the hindcast. By using the time-elongation profile of the CME nose and flank, the ensemble produced an arrival time $0.5\,\mathrm{h} \pm 0.2\,\mathrm{h}$ before the observed arrival time - this is within the model's time resolution. When doubling the initial condition uncertainty ranges, this arrival time error increased to $2.1\,\mathrm{h} \pm 0.5\,\mathrm{h}$ before that determined from in-situ observations. Inconsistency between these results suggests an ensemble size of 201 members may be too small despite operational forecasts using much fewer members in their ensemble. Further investigation is required to determine if there is value in doubling the parameter space of the CME initial conditions. Furthermore, when only the time-

elongation profile of the flank was used to estimate the arrival time and speed error of the CME, all estimates were beyond the range of values obtained by the individual members. This made these estimates unviable. In the case of a MAS-HUXt ensemble, both the ghost front and the flank only techniques generated unviable arrival times estimates for the same reason.

The same method was applied to the hindcast of solar wind speed at L1 to produce an ensemble estimate of L1 solar wind speed. The only successful experiment used BRaVDA-HUXt and the ghost front time-elongation profiles, estimating the speed to be no greater than $22.0\,\mathrm{km\,s^{-1}} \pm 8.5\,\mathrm{km\,s^{-1}}$ than was observed. However, the range of L1 speed produced by all ensemble members was biased towards overestimating the speed by a maximum of $100\,\mathrm{km\,s^{-1}}$.

Since using time-elongations profiles of ghost-fronts appears to contain information about the longitudinal distortion of a CME, then using all the HI1 data available would be beneficial. Currently, when modelling the heliosphere and, thus, CME propagation from $30\,R_\odot$ not all HI1 observations are used. The time-elongation profiles of the leading edge features start a few hours later than the first HI1 elongation measurement during which time the CME may undergo significant changes from the coronagraph observations that inform the CME parameterisation. In the next step, we look to see if the model is improved by accounting for CME distortion between initial observations in the coronagraph data and the model's inner boundary.

Chapter 5

Modelling CME distortion from a lower inner boundary

By use of a reduced-physics heliospheric model, this chapter discusses the plausibility of lowering the inner boundary and initiating a CME closer to the Sun. Therefore, by simulating the propagation of the CME for longer, the impact of CME distortion through interaction with solar wind structure closer to the Sun can be assessed. Furthermore, the modelled CME can be compared with observations throughout the entire *Heliospheric Imager*-1 field of view, and used to quantify model performance. The modifications to HUXt required for this are introduced here. A comparison is made with the results found in Chapter 4. This chapter is part two of a peer-reviewed publication (*James et al.*, 2023).

5.1 Discussion on model inner boundaries

Heliospheric models typically set the inner boundary at a height beyond the Alfvén critical point, between 21.5 $R_\odot$ (e.g. ENLIL) and 30 $R_\odot$ (e.g. HelioMAS). This means that the solar wind modelled is super-alfvénic and that the kinetic energy of plasma is dominant over magnetic pressure, thus, outflows of the solar wind are anti-sunward

and no information propagates back to the boundary from the heliosphere (*Merkin et al.*, 2016). Below the critical point, CME kinematics are complex as non-radial flows and deflections affect the CME trajectory, likely distorting the shape of the CME from that observed in coronagraphs (*Kay et al.*, 2015; *Owens and Cargill*, 2004). Initialising CMEs as simple geometric shapes at the inner boundary based on coronagraph observation is therefore an idealised case, but give rise to an unaccounted error in the model.

Until recent years, the height of the critical point could only be estimated from theory and remote-sensing to be below $30\,R_\odot$. Now, with the near-Sun passes by of NASA's *Parker Solar Probe* (PSP), this mission has recorded the first periods of sub-alfvénic speeds at approximately $16\,R_\odot$ (*Bandyopadhyay et al.*, 2022). Sub-alfvénic conditions mean the magnetic pressure dominates over kinetic energy and shows the critical point has been passed in terms of approaching the Sun. This suggests that the inner boundary of the HUXt model can be lowered from $30\,R_\odot$ while still maintaining the assumption that the solar wind is purely radial.

In addition to the solar wind conditions influencing CME trajectory away from the Sun, CME energy has been shown to drive the event through the heliosphere (*Subramanian and Vourlidas*, 2007; *Temmer et al.*, 2011; *Vourlidas et al.*, 2000; *Vršnak et al.*, 2004). Speed profiles of CMEs show acceleration in the initial stages of the propagation up to distances greater than $30\,R_\odot$ (*Manchester et al.*, 2017). In the HUXt model, this is taken into account as a residual acceleration parameter which was discussed in more detail in Section 3.4.4. Studies suggest the internal energy of the CME's magnetic flux-rope is the driver of this near-Sun acceleration up to a radial distance of approximately $20\,R_\odot$ (*Subramanian and Vourlidas*, 2007; *Vourlidas et al.*, 2000; *Vršnak et al.*, 2014). Beyond radial distances greater than $80\,R_\odot$, the solar wind interaction influences the CME propagation (*Manchester et al.*, 2017; *Vršnak*, 2006). In light of this, a limitation of some models is the missing internal-magnetic (driving) force of a CME that could improve understanding and forecasting ability (*Luhmann et al.*, 2020).

The work of this chapter proposes that by injecting a geometrically simple CME at a lower inner boundary and allowing the solar wind structure to influence the propagation from distances closer to the Sun then some of the previously unaccounted

uncertainty in CME modelling can be reduced. Unfortunately, including the driving force from the CME itself is beyond the capabilities of HUXt's one-dimensional solar wind outflow simulation. However, adjusting the inner boundary height is an adaptation that can be explored with appropriate extension of the acceleration factor to below $30\,R_\odot$.

Coronagraph observations, where the CME often appears to have a more regular structure, are used to estimate the initial parameters of CMEs. For the CME event of 12 December 2008, the first coronagraph observation was made at a radial distance of $8\,R_\odot$. Therefore, this work will assess the variation in model outcome from lowering the inner boundary of the HUXt model to this radial height.

5.2 Physics of reducing the lower boundary in HUXt

Within the reduced-physics HUXt model, the solar wind is modelled as a purely radial outflow and CMEs are initiated as pulses of solar wind speed different from the ambient solution. As such, the HUXt model cannot replicate the near-Sun acceleration of CMEs that are commonly featured in the speed profiles, resulting in the large range of CME speeds that are observed in the heliosphere (*Manchester et al.*, 2017). But as the default inner boundary height is taken to be $30\,R_\odot$, as is the case with the MAS model as well, this is not a major issue. In HUXt, any residual acceleration that is seen beyond this inner boundary height is taken into consideration using an additional velocity function (Equation 3.8).

However, injecting a CME with a geometrically simple shape into the model at $30\,R_\odot$ does not account for any distortion the CME may have undergone while propagating out from the initial coronagraph observations (at $8\,R_\odot$ where the CME appears to have a more regular structure). The internal magnetic field of the CME is the main driver of the CME kinematics when close to the Sun, but since HUXt does not model magnetic field it is important to ensure the kinematics of a CME in the earlier stages of propagation are represented by other means when using a lower inner boundary to $8\,R_\odot$. Adjustments to the solar wind speed structure, cone CME thickness parameter, and the CME initial speed at onset are applied.

5.2.1 Back-mapping solar wind structure

Firstly, in order to initialise the ambient solar wind at $8\,R_\odot$, the solar wind must be back-mapped to this location from $30\,R_\odot$. We must consider changes in solar wind acceleration and solar longitude, resulting from solar rotation during the transit time, T, taken for this radial movement to occur between the two boundaries. *Riley and Lionello* (2011) stated a solar wind acceleration term based on MHD simulations as

$$accV(r) = \alpha V_0 \left[1 - exp\left(\frac{-(r - r_0)}{r_H}\right)\right], \tag{5.1}$$

where an acceleration term $\alpha = 0.15$ and the scale height $r_H = 50\,R_\odot$ produced results in agreement with the HelioMAS model. This equation is used to compute V($8\,R_\odot$) from V($30\,R_\odot$). T is then given by

$$T = \int_{8R_\odot}^{30R_\odot} \frac{1}{V} dr, \tag{5.2}$$

where:

$$V(r) = V_0 + accV(r). \tag{5.3}$$

Using the information derived from these above equations, the change of solar longitude, $\Delta\phi$, can be calculated by

$$\Delta\phi = 2\pi \frac{T}{T_{syn}}, \tag{5.4}$$

where T_{syn} is the sidereal rotation period of the Sun. Since a structured solar wind is used, there is a range of different transit times and hence longitudinal changes between $30\,R_\odot$ and $8\,R_\odot$. This back-mapping method ignores any stream interaction that may take place. The final step in the process interpolates the output onto the HUXt's longitudinal grid spacing. The back-mapped solar wind solution is compared with the original BRaVDA output in Figure 5.1 and Figure 5.2. The technique described above is very good for maintaining the solar wind structure as the two solutions are indistinguishable at $30\,R_\odot$ and by 1 au the back-mapped solution is about $10\,\mathrm{km\,s^{-1}}$ to $30\,\mathrm{km\,s^{-1}}$ slower throughout Carrington Rotation 2077 but still shows fast streams where expected. By visual inspection, the scheme remains a good fit for the in-situ solar wind speed.

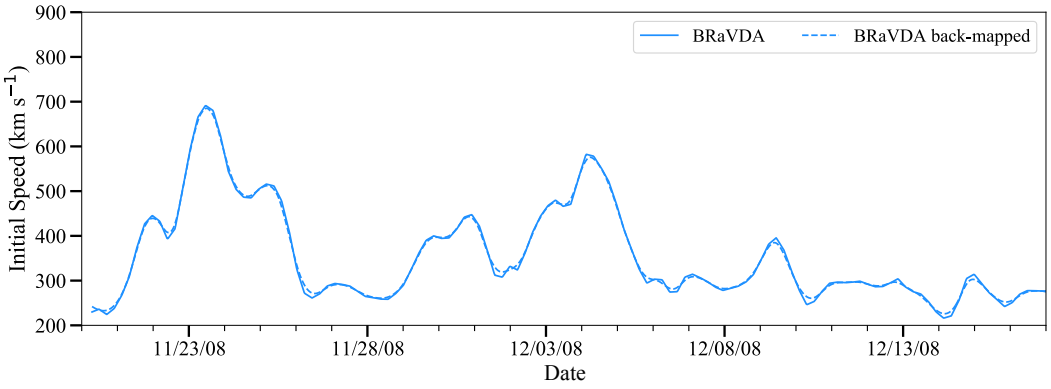

Figure 5.1: The solar wind speed in Earth's latitudinal plane at 30 $R_\odot$ for BRaVDA initialised at this height, and BRaVDA back-mapped to 8 $R_\odot$.

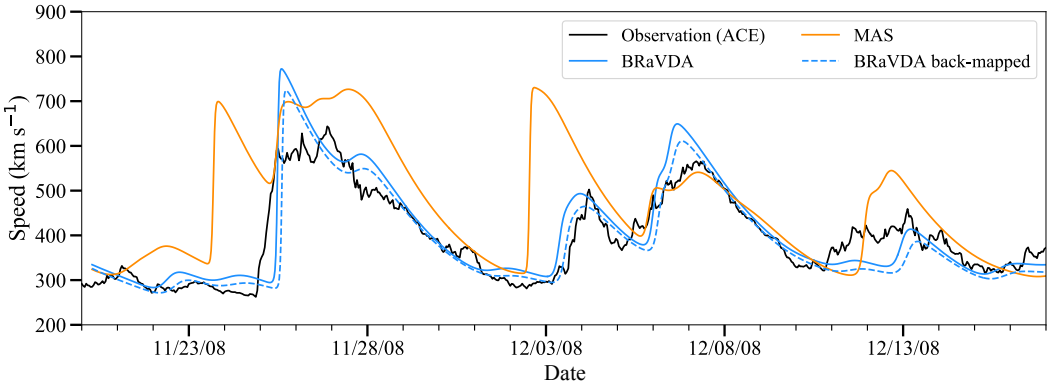

Figure 5.2: Solar wind speed in Earth's latitudinal plane at 1 au for BRaVDA back-mapped to a radial distance of 8 $R_\odot$ in comparison with other solar wind schemes and in-situ ACE data. Similar to Figure 4.10.

5.2.2 Altering CME thickness parameter

A CME will alter in size significantly between 8 and 30 $R_\odot$ as the event expands throughout its propagation. A CME injected in HUXt takes on a elliptical shape of two semi-circles and a radial thickness. The radius of the semi-circles are derived from the cone CME parameterisation, where a smaller inner boundary height will reduce the radius. As a result of the CME radius being smaller at 8 $R_\odot$, we must conserve the momentum of the event which can be done through the thickness parameter. Ultimately, we aim to simulate a CME from 8 $R_\odot$ that will retain similar parameters at 30 $R_\odot$ to those that were used to initialise the HUXt model at 30 $R_\odot$ in Experiment 1, for example. To ensure the total radial length, i.e, the distance

between the leading edge and the trailing edge, is kept constant then the following equation must be true

$$2R_{30} + \tau_{30} = 2R_8 + \tau_8 \tag{5.5}$$

where R is the CME radius of the spherical ends and τ is the thickness, together making the initial ''sausage'' shape of the CME, with the subscript representing the initial height of the CME. With a reduced CME radius at $8\,R_\odot$, we require a greater initial thickness than seen at $30\,R_\odot$ to compensate. The radius of the spherical ends can be calculated using

$$R_{\rm cme} = r_0 tan(\lambda) \tag{5.6}$$

where r_0 is the initial height of the CME and λ is the half-width angle of the CME. As the CME is initialised using cone CME parameters, λ is consistent. By substitution, we can find the equivalent thickness of the CME at the lower inner boundary using

$$\tau_8 = 2 \times 30 tan(\lambda) + \tau_{30} - 2 \times 8 tan(\lambda). \tag{5.7}$$

For the 12 December 2008 event, we calculate that for a CME launching from $8\,R_\odot$ with a half-width of 21° a thickness of $16.9\,R_\odot$ is required. As the thickness of a CME is not directly derived from coronagraph observations, its uncertainty is maintained at $\pm\ 2\,R_\odot$, consistent with the work in *Barnard et al.* (2020). It is noteworthy that the thickness plays a relatively minor role in influencing the distortion of the leading front compared to other CME parameters (*Barnard et al.*, 2023). Given that the primary focus of this research is on the position of the leading edge, this assumption is deemed acceptable. However, for comprehensive future studies, it is recommended to thoroughly evaluate and quantify the uncertainties associated with the thickness parameter. All other parameters used to define the CME remain unchanged, especially since an initial height of $8\,R_\odot$ is more representative of the height at which the CME was estimated from the chronograph data.

Although the boundary has been lowered to $8\,R_\odot$ here, in consideration of the radial distance of the first COR observation, any inner boundary height below $30\,R_\odot$ can be assigned to the equations above and this convention will remain true.

5.2.3 Estimating CME initial speed

Since we cannot model the initial CME acceleration with HUXt, we simulate this CME acceleration by initialising the model with a speed greater than observed at $30\,R_\odot$ when using a lower inner boundary. Using CME parameters estimated from COR observations, a small set of runs was carried out in which only the initial CME speed is changed between runs. After exploring a large range of initial speeds ($300\,\mathrm{km\,s^{-1}}$ to $1200\,\mathrm{km\,s^{-1}}$), a local minimum in RMSE for HI-1 measurements is found to occur at approximately $600\,\mathrm{km\,s^{-1}} \pm 100\,\mathrm{km\,s^{-1}}$ for all features tracked, shown in Figure 5.3. Hence, we use this value to define the CME initial speed at the $8\,R_\odot$ boundary. It could be expected that CMEs travelling at velocities greater than the ambient conditions will induce a shock front ahead of the CME. However, this does not happen in HUXt as it is a hydrodynamic model and the CME propagation is not impacted beyond the intended means. This is justified since no secondary region is identified as having a speed $\geq 20\,\mathrm{km}$ more than the ambient solar wind speed. The model runs continue to use COR observations made at the radial distance of this lower boundary to describe the source location and longitudinal width of the CME.

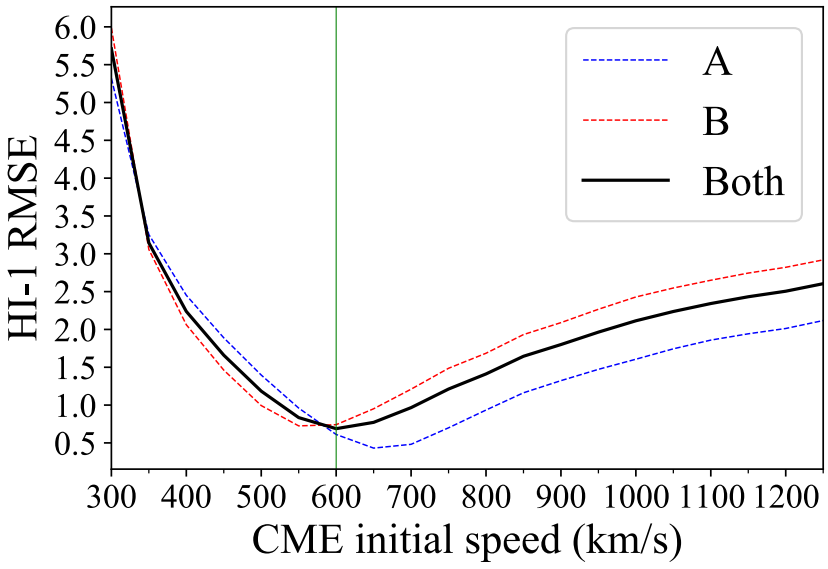

Figure 5.3: Variation in Root-Mean-Square-Error of time-elongation fit of the nose and flank between the HUXt model and HI1 observations for a range of initial speed of a cone CME initialised from a $8\,R_\odot$ inner boundary. The minimum RMSE as seen from both STEREO spacecraft is indicated by the green vertical line.

5.3 How does CME distortion change

By allowing the CME to be initiated from a $8\,R_\odot$ inner boundary, the CME shape can begin to distort and upon reaching $30\,R_\odot$ radial distance the lead edge shape is expected to be different from a CME initialised at the same height. In the top row of Figure 5.4, the CME boundary in Earth's longitudinal plane is shown at 1 hour and 12 hours since the HUXt model initialisation from the original inner boundary height. The leading front is a smooth curve, expected at the beginning of the initialisation. Within half a day some solar wind speed interaction has influenced the boundary. In the figure's bottom row, the comparative time is shown for HUXt initialised from the lower boundary. Since in both cases a CME is defined using the cone model analysis, the variation between the sub-figures is due to the radial distance travelled by the CME. In this case, the leading edge has become jagged by the influence of the solar wind structure and/or model resolution at the earlier time before resembling a smoother curved edge again later. Although the leading boundary resembles the curved edge of the CME during the latter time, there are marginal variations in the CME body. The back-mapped solar wind structure will not have the exact same solar wind speed structure as the original structure, thus, is expected to be the cause of the edge variations. As a result of the small radial distance travelled by the CME, it is tricky to infer how lowering the inner boundary impacts the simulation. In Figure 5.5, HUXt plane plots from a range of times throughout the propagation to Earth are shown for both model set-ups. Again, there are only small variations in the CME leading edges through the simulation that are arguably indistinguishable by visual comparison. Because the CME shape is limited to the model grid resolution, then in some cases the flank regions are smoother than the comparative plane plot, especially towards the end of the simulation when the grid box sizes are spatially bigger. Variation in the radial distance of the leading edge is undetectable here. However, these results do show that the faster solar wind stream on the westward flank continues to not impact the CME distortion significantly, as was the case in the MAS-HUXt experiment in Chapter 4. As a result, lowering the inner boundary to $8\,R_\odot$ reproduced the CME case study suitably, thus, it is possible to apply the ensemble technique and analysis method of the previous chapter to this experiment.

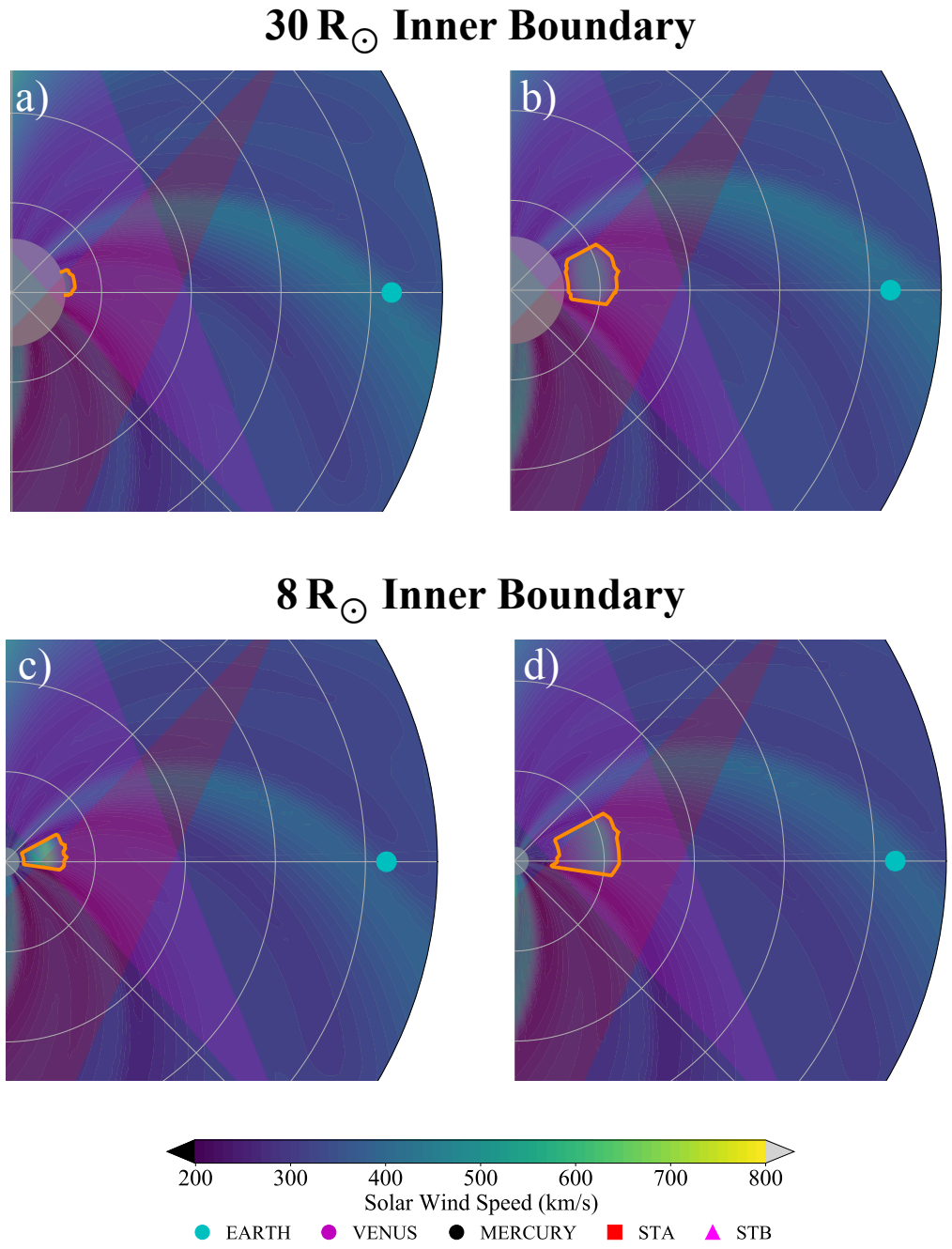

Figure 5.4: Zoomed in BRaVDA-HUXt plots in Earth's latitudinal plane showing the propagation of a CME initialised from a $30\,R_\odot$ inner boundary (top row) and $8\,R_\odot$ inner boundary (bottom row). Two times are shown; approximately 20:10 on 12 December ((a) and (c)) and 07:10 on 13 December ((b) and (d)).

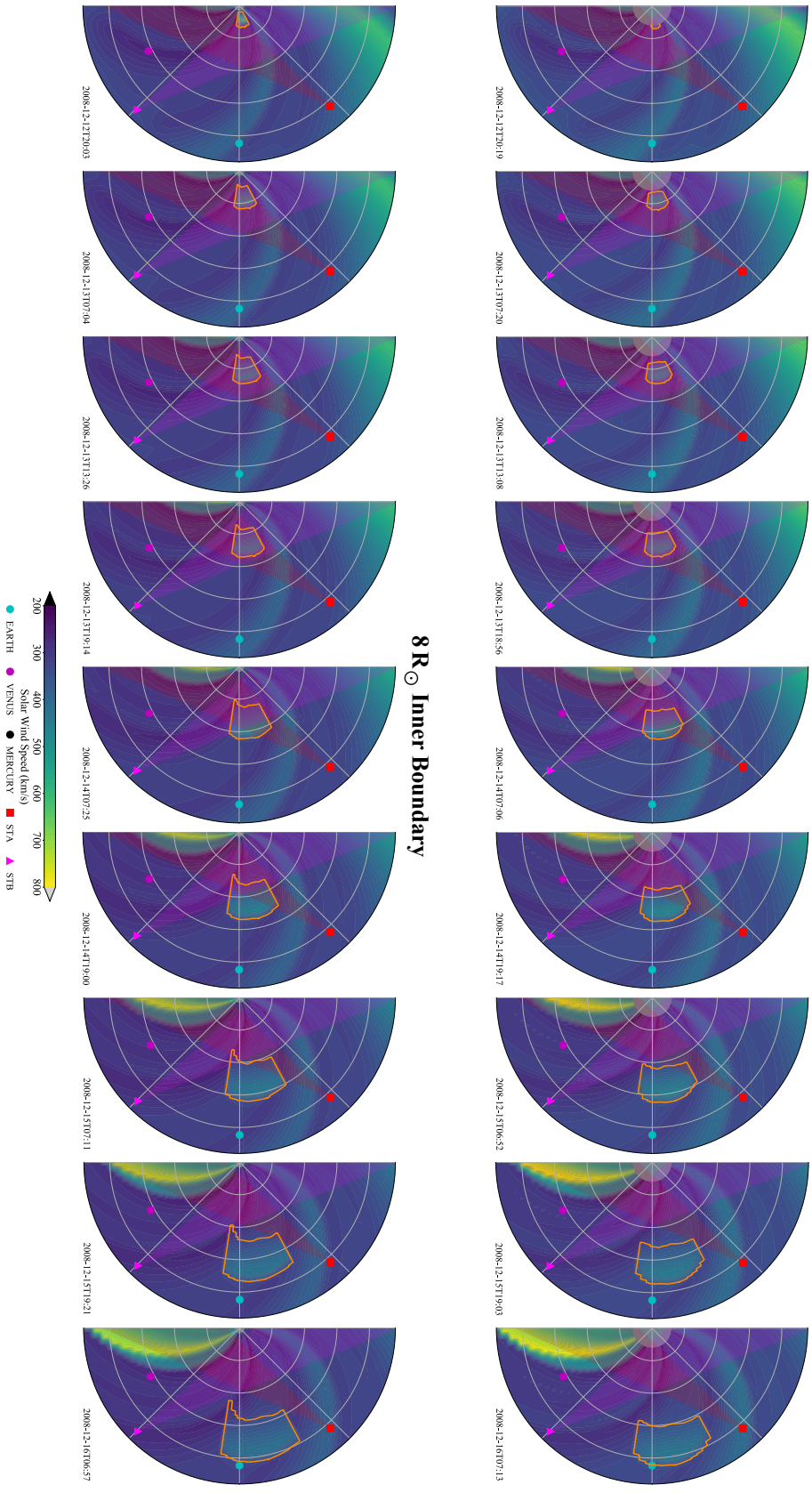
30 R⊙ Inner Boundary
8 R⊙ Inner Boundary
2008-12-12T20:19
2008-12-13T07:20
2008-12-13T13:08
2008-12-13T18:56
2008-12-14T07:06
2008-12-14T19:17
2008-12-15T06:52
2008-12-15T19:03
2008-12-16T07:13
2008-12-12T20:03
2008-12-13T07:04
2008-12-13T13:26
2008-12-13T19:14
2008-12-14T07:25
2008-12-14T19:00
2008-12-15T07:11
2008-12-15T19:21
2008-12-16T06:57
200
300
400
500
600
700
800
Solar Wind Speed (km/s)
EARTH
VENUS
MERCURY
STA
STB

Figure 5.5: HUXt plane plot showing the development of CME evolution in Earth's latitudinal plane throughout the simulation. Two experiments are shown: a CME initialised from a $30\,R_\odot$ inner boundary (top row) and a $8\,R_\odot$ inner boundary (bottom row). Model times range over four days, from 07:03 12 December to 07:13 16 December, from left to right. The HI1 field of view from the observer is shown as translucent red/pink regions extending from the position of the STEREO spacecraft.

Experiments

For continuity, two further experiments are shown here [N.B. the numbered list continues from Section 4.2.4 and corresponds to the experiment number used throughout this chapter]:

4. CME initialised at $8\,R_\odot$ with the parameter and uncertainty estimated by observations, interacting with BRaVDA back-mapped solar wind solution.

5. CME initialised at $8\,R_\odot$ with the parameter and double the uncertainty estimated by observations, interacting with BRaVDA back-mapped solar wind solution.

A MAS-HUXt ensemble is not computed from the lower inner boundary as this experiment is only used as a benchmark for comparison to current operational techniques to forecast CMEs.

Deterministic results

The deterministic run of the back-mapped BRaVDA-HUXt run produces an L1 arrival at 10:17 UTC ± 34 minutes on 16 December 2008, with a speed of $334\,\mathrm{km\,s^{-1}}$. This outcome falls between the two deterministic arrival times produced by the model runs from the default inner boundary height. BRaVDA-HUXt arrival is 2.4 h earlier whilst MAS-HUXt arrival is 2.2 h later. Since the back-mapped BRaVDA solar wind speed at 1 au is a marginally slower profile, it is expected that the arrival time of the CME is later than BRaVDA-HUXt from $30\,R_\odot$.

Comparing the time-elongation profiles of the nose and flank with the fronts observed in HI1 in Figure 5.6, the RMSE values for STEREO-A, STEREO-B, and both spacecraft combined are 0.61°, 0.74°, and 0.69° respectively. This equates to an improvement in the RMSE compared with the $30\,R_\odot$ deterministic run by at

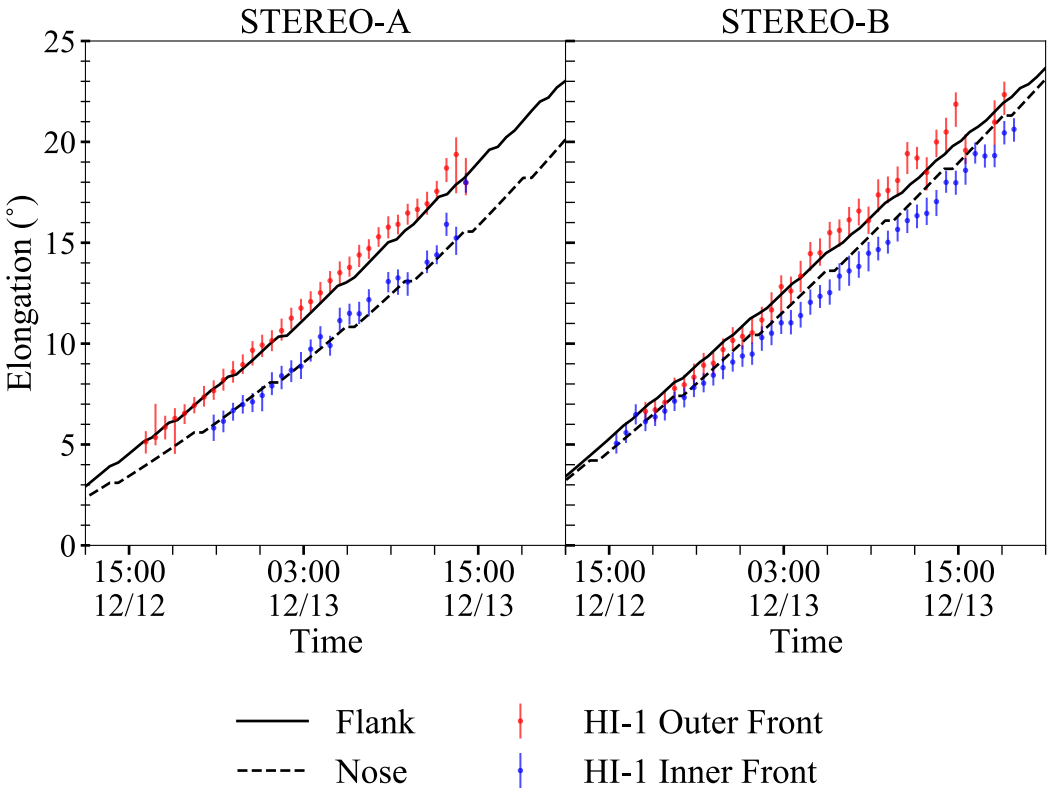

Figure 5.6: Time-elongation profiles for the deterministic CME using back mapped BRaVDA-HUXt. The nose and flank profiles throughout the HI1 field of view as seen from STEREO-A (left) and STEREO-B (right). SECCHI HI1 observations of bright fronts in Earth's latitudinal plane are displayed as error bars.

least 10 %. However, caution should be applied before concluding that lowering the inner boundary is the best technique because the HI1 fitting was used to infer the required initial speed of the deterministic CME. Thus, a good fit is likely a result of this optimised speed. By using an ensemble approach, the parameter space can be explored for a fairer comparison.

5.4 Impact on ensemble results

Analysis of the ensemble results from Experiments 4 and 5 have followed the method carried out in the previous chapter. A quadratic relationship between the arrival time/speed estimates at L1 and the RMSE error of time-elongation profiles in the HI1 field of view is computed using the lowest 25 % of binned data. The trough of this relationship identifies the ensemble estimate of the arrival time/speed error. For

the back mapped BRaVDA-HUXt experiments, a quadratic fit to the data remains a suitable description, displaying a similar data scatter to the previous Experiments 1 and 2.

Arrival time error results for both back-mapped BRaVDA-HUXt ensembles are displayed in Figure 5.7. Using the COR estimated parameter uncertainties (Experiment 4), the ensemble spread of ATE values is within 9 h. This is similar to the average CME arrival time uncertainty obtained through current forecasting methods (*Iwai et al.*, 2021; *Mays et al.*, 2015; *Riley et al.*, 2018a; *Vršnak et al.*, 2014). The curve minimises at 2.8 h ± 0.5 h, therefore, estimating a later-than-observed arrival. The arrival time of the CME is observed at 07:00 UT on 16 December 2008, based on a sudden enchantment of speed in the ACE data (Section 4.1). The ensemble result is 0.5 h earlier than the deterministic run, however, since the CME initial speed of the deterministic run was inferred from HI1 fitting the comparison of these two values is insignificant. When the parameter space of the initial conditions is doubled (Experiment 5), the ensemble spread it greater producing ATE values up to 18 h from observation. The ensemble's curve minimum is found at 2.9 h ± 0.6 h, an almost identical ATE to Experiment 4. This outcome was not found between

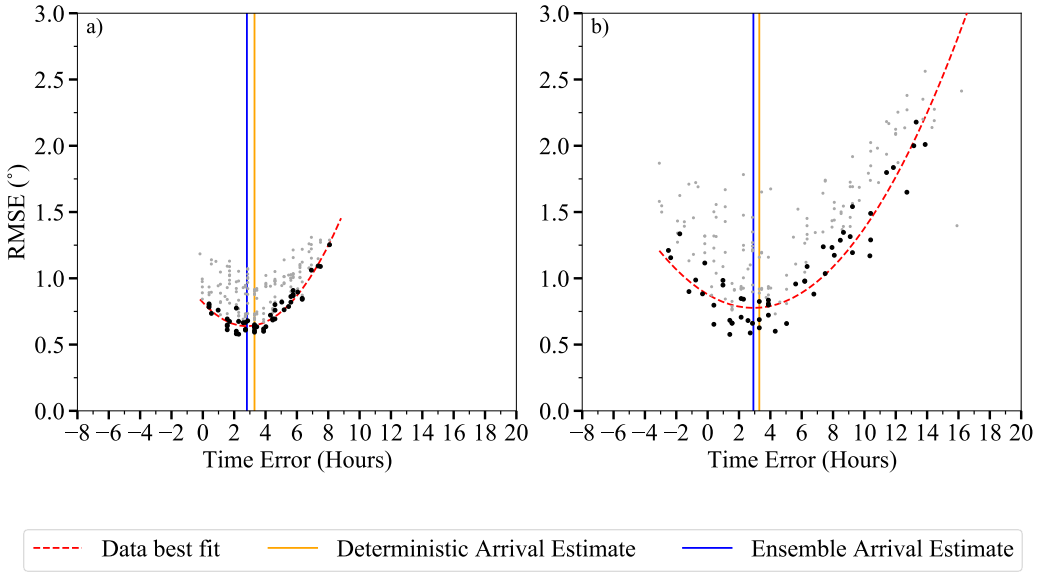

Figure 5.7: Scatter plots of the time-elongation profile RMSE values and the arrival time error for each model member in (a) experiment 4 and (b) experiment 5. A quadratic line of best fit (red, dashed) is fit to the lowest 25% of data per bin (black dots).

Experiment 1 and 2 in Chapter 4 in which these ensemble estimates varied by 1.6 h. The shared lower boundary height of experiments 4 and 5 allowed the model simulations to extend over a longer duration. This prolonged simulation time, in turn, enabled the CME to undergo more pronounced distortion, making the evaluation of errors more uniquely influenced by the initial conditions of each ensemble member. As a result, the convergence of outcomes in Experiments 4 and 5 can be attributed to the specific influence of the lower boundary height on the CME propagation dynamics. We see this demonstrated in Figure 5.7 by steeper best-fit curve fitting to the data than compared with their counterpart experiment for $30\,R_\odot$, meaning there is a greater rate in change in RMSE value with variation in ATE value. Further, it highlights that the parameter uncertainties based on coronagraph observations are sufficient. The curve minima of ATE from the $8\,R_\odot$ BRaVDA-HUXt ensembles are associated with a lower RMSE value than their $30\,R_\odot$ counterpart; 0.73° drops to 0.64° when using the estimated coronagraph parameter uncertainty (Experiment 4), and 0.82° drops to 0.78° when using twice the estimated uncertainties (Experiment 5). These results highlight again that by allowing the CME to distort before reaching the field of view covered by HI1 then the model can simulate the real data with better accuracy. Whilst this idea is expected of a real CME propagation through the heliosphere, it is important to remember that the simplified HUXt model is replicating the kinematics only and that replicating this in an MHD model may find different outcomes since magnetic fields close to the Sun impact the CME's shape and motion.

Using the same method on the arrival speed, Experiments 4 and 5 estimate an Arrival Speed Error of $-4.0\,\mathrm{km\,s^{-1}} \pm 3.4\,\mathrm{km\,s^{-1}}$ and $11.9\,\mathrm{km\,s^{-1}} \pm 4.9\,\mathrm{km\,s^{-1}}$ respectively from the observed $333\,\mathrm{km\,s^{-1}}$ measured by ACE. This can be seen in Figure 5.8. The ensemble estimates do not exhibit an improvement over the deterministic results, which is expected given that the initial speed for the deterministic run is derived from HI1 observations. The advantage of ensemble modeling, designed to capture a spectrum of plausible outcomes, is outweighed by the specific method used to determine the initial speed at $8\,R_\odot$. Assessing the error in arrival speed for these experiments is challenging without introducing bias. In comparison to the BRaVDA-HUXt ensembles initiated at $30\,R_\odot$, these results produce a more accurate estimate

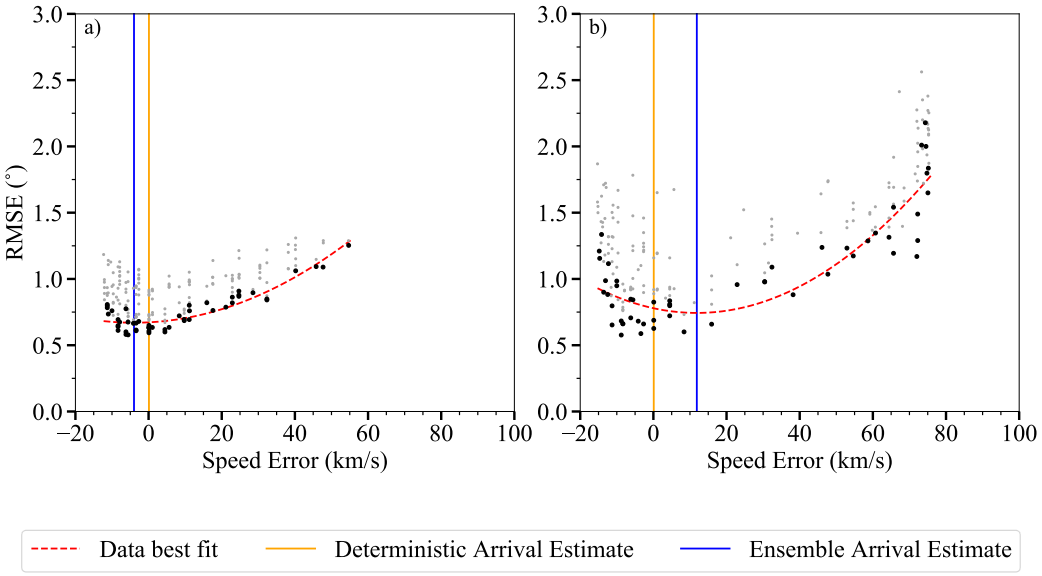

Figure 5.8: Scatter plots of the time-elongation profile RMSE values and the arrival speed error for each model member in (a) experiment 4 and (b) experiment 5. A quadratic line of best fit (red, dashed) is fit to the lowest 25% of data per bin (black dots).

of the CME leading edge speed at L1, with a significant increase in magnitude: an improvement of $1.9\,\mathrm{km\,s^{-1}}$ for Experiment 4 and $10.1\,\mathrm{km\,s^{-1}}$ for Experiment 5. These values are tiny in comparison with the CME speed ($\leq 0.1\,\%$) and possibly insignificant. Therefore, in this hindcast analysis of a single case study, it cannot be said that altering the inner boundary height is influential in estimating the CME speed at 1 au. If this technique was applied in a real-time forecast, the arrival speed estimate would be a very good estimate regardless of the initial boundary height.

Tracking only the flank position

The analysis of these two experiments is repeated using the time-elongation profiles of the flank only. The relation of RMSE against arrival time error is seen in Figure 5.9 and RMSE against arrival time speed is seen in Figure 5.10.

Looking at the arrive time error (Figure 5.9), the curve minimises at $0.7\,\mathrm{h} \pm 0.8\,\mathrm{h}$ for Experiment 4 and $1.6\,\mathrm{h} \pm 1.0\,\mathrm{h}$ for Experiment 5, therefore producing a better estimate of the arrival than using both the nose and flank features. Whilst previous results highlight that the elongation of multiple fronts detected in HI1 data can be replicated using the nose and flank of a CME leading edge, these results suggest that

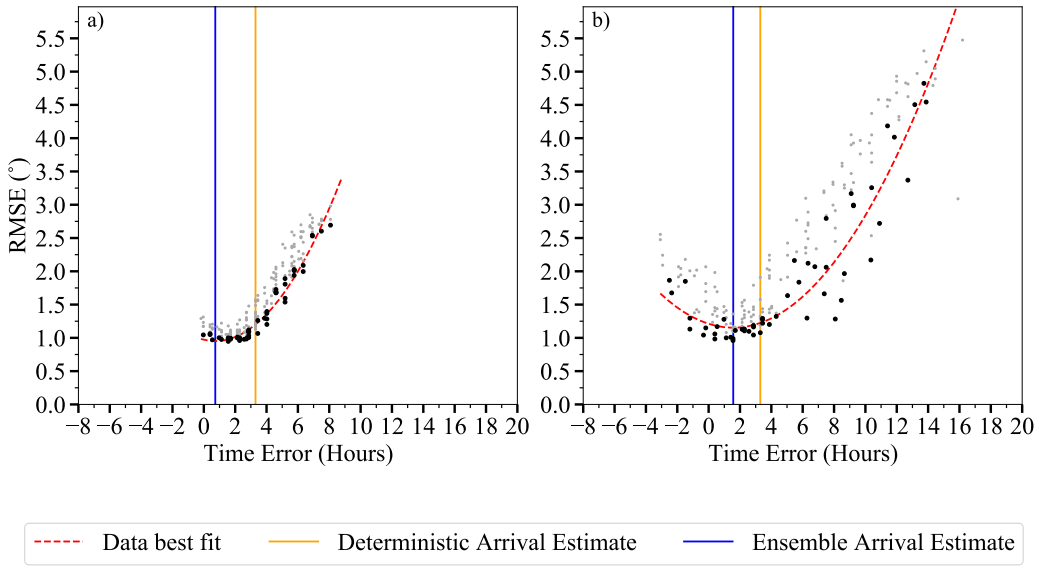

Figure 5.9: Root-Mean-Square-Error of the flank only in HI1 field of view against the Arrival Time Error (ATE) of the CME leading edge at L1, using BRaVDA-HUXt initialised from 8 $R_\odot$.

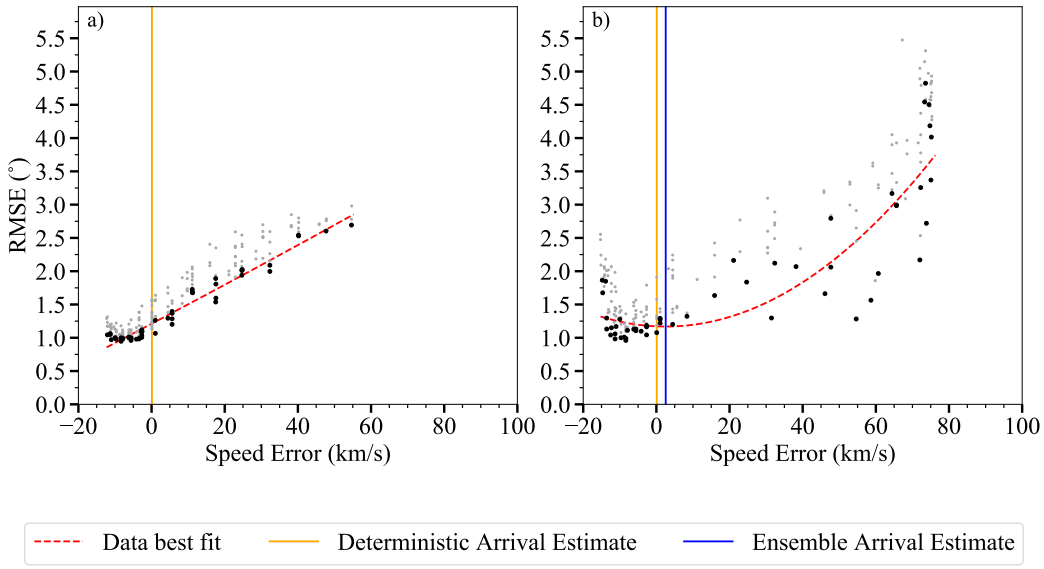

Figure 5.10: Root-Mean-Square-Error of the flank only in HI1 field of view against the Arrival Speed Error (ASE) of the CME leading edge at L1, using BRaVDA-HUXt initialised from 8 $R_\odot$.

tracking a single feature may also be sufficient in producing arrival predictions as long as we account for early CME distortion by lowering the inner boundary of the model. The accuracy with which the flank's time-elongation profile evolves from the lower inner boundary may be unique to this case study in which HUXt accurately captures the distortion of a relatively slow-moving event. It would be of interest to find if this outcome is replicated in other CME case studies.

However, when we only consider the flank for estimating arrival speed in Experiment 4 (Figure 5.10), the ensemble doesn't effectively minimise an arrival speed within its range. The data spread doesn't clearly show a quadratic trend but rather a positive linear one. Hence, it seems that the ensemble data analysis technique might not be the best fit for this data set. This could be extended to Experiment 5 data, which has a large cluster of data at ASE < 0. Whilst the data has been fitted with a quadratic fit, there is weak correlation to this with ASE > 0. Despite this, the ensemble speed estimate is near accurate but not an improvement to the deterministic results for reasons stated earlier.

Table 5.1: Summary of the estimated arrival time error and arrival speed error from minimising the correlation between ensemble RMSE and arrival errors. Values in italics are noted as estimates that fall outside the ensemble range. This is an extended version of Table 4.2, now including the two experiments (4 and 5) from an inner boundary height of $8\,R_\odot$. An uncertainty of *NaN* means that it is not applicable. This is because the deterministic run produces one value and there is no finite resolution of the measurement.

Experiment	**Arrival Time Error** (hours)			**Arrival Speed Error** ($\mathrm{km\,s^{-1}}$)		
	Deterministic	Ghost-front Features	Flank only	Deterministic	Ghost-front Features	Flank only
1	0.9 ± 0.6	- 0.5 ± 0.2	*-4.4 ± 1.1*	20 ± NaN	5.9 ± 3.0	*350.7 ± NaN*
2	0.9 ± 0.6	-2.1 ± 0.5	*-11.1 ± 4.9*	20 ± NaN	22.0 ± 8.5	-74.2 ± 72.1
3	5.5 ± 0.6	*-1.9 ± 2.7*	*-5.6 ± 6.4*	-5 ± NaN	*227.3 ± 226.5*	*180.4 ± NaN*
4	3.3 ± 0.6	2.8 ± 0.5	0.7 ± 0.8	1 ± NaN	- 4.0 ± 3.4	*-2235.9 ± NaN*
5	3.3 ± 0.6	2.9 ± 0.6	1.6 ± 1.0	1 ± NaN	11.9 ± 4.9	2.6 ± 6.1

5.5 Practicality of lowering model boundaries in further work

In order to accurately simulate the CME, the initial radial speed has to be artificially enhanced to counteract the missing acceleration that drives the plasma away from the Sun. As acceleration continues beyond the radial height of COR observations, estimating the initial radial speed required for the CME injected at a lower boundary in HUXt cannot be from COR data. In this chapter, a technique using HI observation has been proposed using the fitting accuracy of time-elongation profiles to estimate a suitable initial speed. By then using an ensemble approach to simulate CME propagation, the uncertainty in the initial speed estimate is acknowledged. Using HI data to infer the initial speed is not practical in real-time forecasting as this would reduce the lead-time of the forecast, which is one benefit of lowering the inner boundary and using observations closer to the Sun. Further work is required to develop a technique to calculate the initial speed in order to optimise the lead time of the model runs. This technique would be better if it were independent of HI1 observations, especially if time-elongation profiles are used to measure model performance.

Coronal models currently output solar wind speed structure at the original inner boundary height, therefore, the solar wind speed input at a lower boundary should be considered. Back-mapping of the BRaVDA solar wind solution has been presented here. The method can be extended to any coronal model solution, although further work would be required to prove the technique continues to provide accurate results. However, must back-mapping be the only method for defining ambient wind at this height? Recent work from *Bunting and Morgan* (2022) demonstrates the use of tomography maps to infer solar wind speed at a radial height of $4\,R_\odot$ to $8\,R_\odot$ from coronal plasma density observations and this may provide an alternative approach.

5.6 Summary

This chapter has used the reduced physics assumptions of the HUXt solar wind model to lower the inner boundary in which the solar wind speed and CME are initialised. The boundary has been lowered from the default height of $30\,R_\odot$ to

$8\,R_\odot$, inline with the radial height of the first coronagraph observation for the 12 December 2008, CME. Initial conditions of the CME were estimated from these COR observations. This approach takes advantage of the inherent geometric symmetry of CMEs when in close proximity to the Sun, a consequence of their constraint by the high magnetic pressure in that region.The HUXt model benefits significantly from this approach, as it incorporates the assumption of symmetrical CMEs during the initialisation process.

In order to simulate CMEs at a lower inner boundary, a number of adaptions were required to the HUXt model. Firstly, back-mapping the solar wind solution from $30\,R_\odot$ to $8\,R_\odot$. Secondly, as HUXt cannot accelerate a CME using its internal energy since it does not exist in the reduced-physics approach, the CME initial speed is required to be greater than it would at $30\,R_\odot$. This value is non-observable from coronagraphs as CMEs continue to accelerate out to a radial distance of approximately $20\,R_\odot$ and the speed values obtained from coronagraph images are lower than the $30\,R_\odot$ speed. Therefore, a technique using HI1 fitting to estimate the initial speed was introduced.

By these adaptations, simulating CME propagation from the lower inner boundary was shown to be a viable experiment as the deterministic run produced arrival time estimates in line with the BRaVDA-HUXt and MAS-HUXt simulations from the default boundary height. As a result, this chapter extended on the work of Chapter 4, exploring if L1 arrival estimates of the CME time and speed were accurately predicted using the information of longitudinal distortion in the HI1 field of view. This allowed us to explore if the shape of a CME which undergoes more distortion due to the influence of the solar wind speed produces a better representation of longitudinal distortion. For this, the two leading bright fronts, seen by the *Heliospheric Imager*, has been interpreted using the ghost front theory.

Using an ensemble where only the CME initial conditions are varied, it was interesting to find that the method produced a constant L1 arrival time in the two experiments. The only difference was the parameter space in which the ensembles could perturb. Such a result was not found when running the model from the default boundary height, suggesting the additional distance in which the CME could distort is beneficial in producing a unique outcome of the model run. Consequently, the

relationship between HI1 RMSE and arrival time error is better defined. This arrival time was approximately 2.9 h after the observed arrival, which was defined as 07:00 UT on 16 December 2008, based on an enhancement in ACE in-situ speed data.

The work was extended to look at the arrival estimates if only the CME flank was tracked. In this case, it was found that the ATE was reduced; 0.7 h and 1.6 h after the observed arrival for the two experiments. The analysis method was now viable by lowering the inner boundary, which was not the case in Chapter 4. However, further work is required to know why this is. Furthermore, such results suggest that the ghost front theory interpretation of the bright fronts in HI images is not essential when modelling from a lower boundary. However, since the ATE values are not consistent, further work is recommended to evaluate the benefit of the ghost front feature tracking.

Whilst the results from this study were interesting and the initial results show the benefit of modelling CME distortion from near-Sun distances, there are implications to being able to apply a lowered inner boundary technique to forecasting. Firstly, the solar wind structure used in this work makes use of a back mapping technique to a data-assimilated solar wind solution. Further work should look into current operational solar wind solutions, like MAS or WSA, to see the accuracy at which the back-mapping method can recreate the L1 data. Alternatively, techniques that have been developed to infer the solar wind speed at $8\,R_{\odot}$ radial distance using tomographic mapping of coronal plasma density (*Bunting and Morgan*, 2022) could be deployed. Secondly, the required initial speed of the CME in order to simulate a true speed observed later in the propagation was found using the quality of fit to the HI-1 time elongation profiles. In now-casting, this data is not available. Therefore, an alternate method must be developed which depends only on observations that would be available to the forecaster in real time.

Chapter 6

Can Heliospheric Imagers improve lead-time for arrival predictions?

This chapter explores the number of *Heliospheric Imager* (HI) observations that are required to give a valid indication of the HUXt model's performance at accurately simulating Coronal Mass Ejection (CME) distortion. Through evaluating the time difference between the HI observation and the known arrival of the 12 December CME at L1, the lead time of forecasts is assessed. Firstly, the current literature on CME forecast lead time is discussed.

6.1 Lead-time of CME forecasts

For technologies and businesses that are vulnerable to space weather hazards, advance warning of geomagnetic conditions is required for the timely implementation of risk plans that are used to mitigate the impacts. For example, a 1-3 day advanced warning of a CME's Earth arrival time and geoeffectiveness is desirable for Norway's Transmission Grid, with more specific details significant to the electric grid

technologies expected closer to arrival (*Krausmann et al.*, 2013).

Much work has been done in the solar physics community to attempt estimates of future conditions for the near-Earth environment, for example in the form of persistence-forecasting of solar wind conditions that give a 27-day advanced prediction based upon the in-situ observations of the current solar rotation (*Owens and Forsyth*, 2013). However, transient events are expelled from the solar surface on a much shorter timescale and, thus, other techniques must also be developed.

When forecasting the arrival of interplanetary CMEs at Earth using any of the modelling methods mentioned in Chapter 3, there is one thing in common; the use of near-Sun observations to estimate the upcoming conditions near Earth. Depending on the speed of a CME, it can take up to five days to propagate from the Sun to 1 au. Therefore, it seems feasible to provide predictions with reasonable lead time. In the case of very fast events, such as the Carrington event in 1859 which reached Earth in under 18 hours (*Carrington*, 1859; *Tsurutani et al.*, 2003), forecasts with long lead times suitable for warning systems are not possible, unless we can accurately predict an eruption from the Sun. Forecasts are based on numerous assumptions leading to substantial uncertainties. Firstly, kinematic parameters of a CME developed from coronagraph observation do not provide insight into the distortion, deflection, and acceleration that the CME body will undergo throughout the heliosphere (e.g., *Lugaz et al.*, 2017; *Manchester et al.*, 2017; *Török et al.*, 2018). Secondly, making simplistic assumptions about the initial state and evolution of the CME in models (for example, a limitation of the cone model is the assumption CMEs are symmetrical about the line of propagation when initialised) can often lead to outcomes that do not compare favourably with observations. Furthermore, reconstruction of CMEs using fitting techniques can be highly uncertain due to too few viewpoints. Small changes to the initial parameters of these models can result in quite varied results (*Kay et al.*, 2017). In spite of this, near-Sun observations from white light cameras have provided crucial information that has advanced the accuracy of predictions (e.g., *Amerstorfer et al.*, 2021; *Liu et al.*, 2010b; *Pizzo et al.*, 2011; *Riley et al.*, 2018a; *Scolini et al.*, 2018). Operationally, the WSA-ENLIL-Cone model performs very well at forecasting the arrival of CME/ CME shocks on Earth (*Pizzo et al.*, 2011; *Riley et al.*, 2018b; *Taktakishvili et al.*, 2010, 2011). Analysis of forecasts submitted to the

NASA's Community Coordinated Modeling Center (CCMC) web-based form over a five-year period showed that the WSA-ENLIL-Cone model was associated with accurate and long-lead time forecasts, with a mean absolute error of 17.3 h and an average lead time of 46.4 h across 70 CME forecasts submitted by MOSWOC (*Riley et al.*, 2018b). However, quantifying lead time in this study required knowledge of the real observed arrival of the CME (shock) at Earth, a value unobtainable in real-time forecasting. Whilst trends suggest the accuracy in the performance of a model with respect to lead time, anomaly forecasts and bias could skew the findings. Thus, an average of all the model predictions is also presented in the CCMC as an alternative estimate of CME arrival.

In order to improve the lead time of real-time forecasting, consistent remote sensing observations of the Sun and heliosphere is essential. With a wide field of view between the Sun and Earth, such as the view provided by heliospheric imagers, CME forecasts could be revised as the eruption evolves with time and distance (*Kilpua et al.*, 2019; *Rodriguez et al.*, 2020). Such an idea is deemed possible from a single viewpoint and possible with the future L5 mission, now called Vigil (*Gibney*, 2017; *Kilpua et al.*, 2019; *Vourlidas*, 2015).

Whilst the STEREO mission provides a suitable data set to test the theory on past events, SECCHI science data is only available three days after observation (*Rodriguez et al.*, 2020). On this timescale, SECCHI's HI data could not be used for real-time forecasting of fast CME events. Near real-time space weather beacon data from STEREO (*Kaiser et al.*, 2008), transmitted every 24-hours, has been used to investigate its application to forecasting (e.g., *Kirnosov, Vladimir et al.*, 2016; *Koning et al.*, 2009; *Tucker-Hood et al.*, 2015). It has been used to track CME with reasonable accuracy (*Koning et al.*, 2009), and automated CME tracking from low elongation has been successful (*Kirnosov, Vladimir et al.*, 2016). But other studies has suggested that the lower resolution and intermittent reception of STEREO beacon data reduces its impact in forecasting accuracy (*Tucker-Hood et al.*, 2015). Future missions aim to significantly reduce the transmission timescale of high-resolution data.

6.2 Method

For the 12 December 2008 CME event, STEREO observed a slow-moving CME travel through the heliosphere towards Earth. In the HI-1 field of view, 42 running-difference images show the CME up to an elongation of approximately 22°. The first observation was made by STEREO-B at 15:29:37 12 December, whilst STEREO-A's first observation was a single time-step later at 16:09:01 12 December. Both spacecraft make their final HI1 observation by 18:49:36 on 13 December. There is an approximate 37-second discrepancy between the timestamp of both spacecraft and hence we take the later timestamp, from STEREO-B, in the analysis. The CME arrived at L1, t_{arr}, at 07:00:00 ($\pm$ 1 hour) on 16 December 2008, just under four days from the initial HI1 observation as an enhancement of speed in the in-situ ACE data (Section 4.1).

In previous chapters, an evaluation of HUXt's performance to simulate CME longitudinal distortion was conducted. By simulating time-elongation profiles of the nose and flank of the CME and comparing with observations of bright frontal features in HI1 along the same plane (consistent with the ghost front theory *Scott et al.*, 2019) the error was quantified using the RMSE measurement. In the work, all available observations were considered as a whole, obtaining an error value for each elongation profile. In addition, the RMSE of all four time-elongation profiles (the nose and flank seen from both STEREO spacecraft) together was computed for the HUXt simulation. Now, this technique will be extended to evaluate the model's performance using a cumulative RMSE. Starting with a single HI1 observation and increasing the number of observations by increments of one until all observations are used, we explore how the RMSE value varies as a function of the number of observations and, thus, time. The expectation being that the more observations used to constrain the model, the better the accuracy of the results. On evaluating a single HUXt run, it implies that with more observations the more reliable the RMSE value should be at informing the skill of the member, albeit with a shorter lead time. However, this technique on a single model run would not lead to an improvement in the accuracy of estimating the arrival of a CME at Earth since the simulation will only produce one possibility, based on the assumed initial conditions. Therefore, an

ensemble method is applied.

By only changing the initial cone CME parameters, an ensemble of 201 members (1 deterministic member and 200 randomly perturbed members) is computed. There are five free parameters - source longitude, source latitude, speed, width, and thickness - that are randomly and uniformly perturbed within the estimated uncertainties of the coronagraph observations. For each HUXt simulation (i.e. ensemble member), the cumulative RMSE of the model's performance at recreating the four HI1 time-elongation profiles is measured along with the arrival time of the CME at L1. Previously, a quadratic trend was suitable to describe the correlation between the RMSE value and the L1 Arrival Time Error (ATE) when all available HI1 observations were used. By minimising the quadratic line of best fit and locating the local minimum, an ensemble arrival time estimate of the CME was produced based on constraining the model against HI1 observations. This technique is once again replicated here. Before, the arrival time was given as an Arrival Time Error from the observed arrival at 07:00 UT 16 December 2008. Now, this has been changed to UT arrival time only.

Repeating the process 42 times, for each STEREO-B HI1 timestamp, the modelled time-elongation profiles are compared with the observations made up to and including that time stamp. From this, an ensemble-based estimate of the CME arrival is produced. In a sense, the CME model and, thus, forecast prediction, is being updated whilst ''the CME is propagating''. As a result, changes to the ensemble arrival time estimate can be analysed in retrospect with the number of observations, CME radial distance, or lead time. The latter is explored here, whereby the lead time is presented as

$$\text{Lead Time} = t_{arr} - t_{obs} \tag{6.1}$$

where t_{obs} is the timestamp of the ''latest'' HI1 observation and t_{arr} is the observed arrival.

The ensemble method is applied to three HUXt set-ups; BRaVDA-HUXt and MAS-HUXt initialised from $30\,R_{\odot}$ (similar to operational physics models), and BRaVDA-HUXt initialised from $8\,R_{\odot}$. These are equivalent to Experiments 1, 3 and 4 in Chapter 4 and 5. In *Coronagraph* observations of many CMEs, their shape is

seen as a spherical structure whilst under magnetic pressure restraint and so a cone can be used to initialise the CME in HUXt. As HUXt is a reduced-physics approach, lowering the inner boundary to the height of COR2 observations is possible, as was discussed in Chapter 5. Furthermore, HI1 first observes the bright fronts of the CME at a radial height lower than $30\,R_\odot$ and, therefore, misses the opportunity to use early observations. In this work, HUXt ensembles starting from $30\,R_\odot$ uses 36 HI1 observations, starting after 19:00 UT 12 December, whilst ensembles starting from $8\,R_\odot$ use all HI1 observations. For a slow CME event, like the 12 December 2008 CME, the number of unused observations may be insignificant. However, a faster event would propagate through the HI1 field of view faster and, consequently, fewer HI1 observations would be obtained. Thus, these early observations could be vital in characterising CME kinematics.

Presented here are the results for modelling the CME with HUXt as a deterministic (single simulation) case and an ensemble case from $30\,R_\odot$ and $8\,R_\odot$.

6.3 Results

6.3.1 Deterministic HUXt run

The cumulative RMSE for a single run is explored using the deterministic runs of the experiments. Here, in Figure 6.1, the variation in RMSE value with an increasing number of observations is shown for the BRaVDA-HUXt experiments. Thus, by initialising the model from a default $30\,R_\odot$ inner boundary and the $8\,R_\odot$ lowered inner boundary, conclusions can be made about the significance of the boundary height. The simulations from the perspective of the two STEREO spacecraft have been separated to show the RMSE variation for the position of the nose and the flank independently and together. In the lowest panel, the whole model response is shown.

The general trend shows that the RMSE value increases with more observations. This tells us that the gradient of the time-elongation profiles does not match the observations precisely, but this is only understood by using observations at a greater radial distance. In the case of the majority of the profiles, except for the viewpoint of STEREO-A from $30\,R_\odot$, you would believe the model is performing well from the

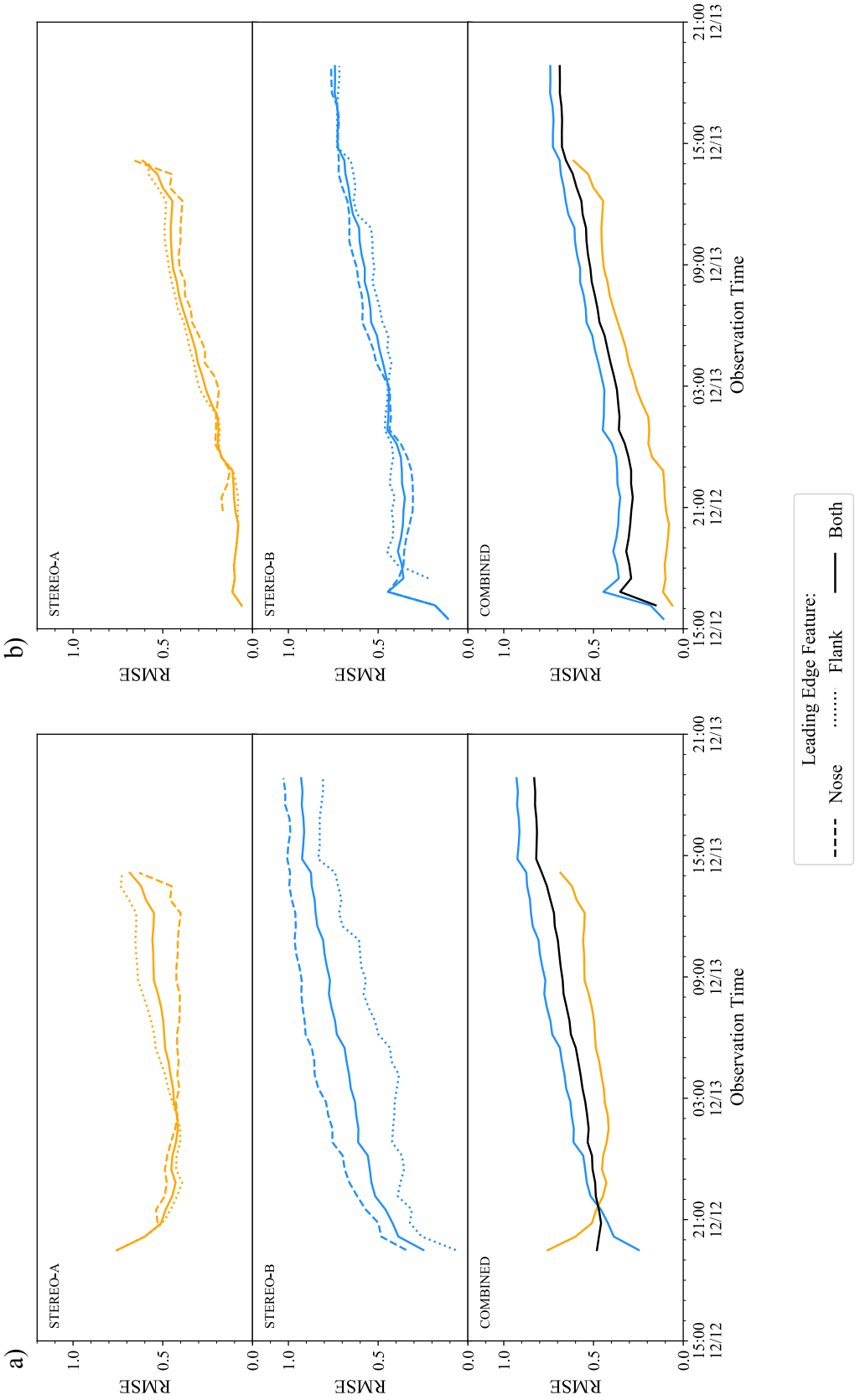
a)
b)
STEREO-A
STEREO-B
COMBINED
RMSE
0.0
0.5
1.0
15:00 12/12
21:00 12/12
03:00 12/13
09:00 12/13
15:00 12/13
21:00 12/13
Observation Time
Leading Edge Feature:
Nose
Flank
Both

Figure 6.1: The variation in Root-Mean-Square-Error between the model time-elongation profiles and HI1 observations as more HI1 observations are used. The HUXt model has an inner boundary height of (a) $30\,R_\odot$ and (b) $8\,R_\odot$. The flank and the nose of the CME leading edge are tracked in the model, in line with the Ghost front theory (*Scott et al.*, 2019), and are shown as a dotted line and dashed line, respectively. The combined error is represented by a solid line. The top panels show the time-elongation profiles from the STEREO-A position (orange) whilst the middle panels show them from STEREO-B's position (blue). The bottom panels show the combined error from both spacecraft (black).

first observation with the greatest RMSE measured for a single profile being 0.34° for the tracking of the nose feature from STEREO-B in BRaVDA-HUXt from $30\,R_\odot$. However, that profile has an RMSE of 1.03° by the end of the HI1 field of view.

There is a substantial difference in the benefit of using the ghost front theory between the two deterministic runs. When computed from an $30\,R_\odot$ inner boundary, the flank profile is continually measuring a lower RMSE value than the nose from STEREO-B with a gap ranging 0.15° to 0.45° between the two profiles. In this case, the average error of the two profiles, shown as a solid line, is beneficial to asses the model performance. From STEREO-A, the two profiles are not as clear as the nose profile goes from the ''worst'' fitting to plateauing at 0.4° RMSE and matching the observations better than the flank profile. In comparison, when computed from an $8\,R_\odot$ inner boundary, the separation between the nose and flank profiles is minimal from both spacecraft viewpoints with an approximate 0.1° difference between the error measurements. In this case, taking an average error is less beneficial. These findings support the conclusion of Section 5; tracking the flank alone is sufficient to assess model performance for simulating CME leading edge distortion throughout the HI1 field of view. But, ghost fronts are not detrimental to the method either (discussed further in Section 6.4.3). On the contrary, finding the average error between the profiles is a suitable method for assessing the whole model performance when using multi-spacecraft observations. Furthermore, the RMSE values are overall lower when time-elongation profiles are simulated from the lower inner boundary. This may be due to the technique used to identify the CME initial speed from $8\,R_\odot$ using HI1 observation fitting, thus, it may produce a low RMSE. In light of this, assessing the benefit of including the observations before 19:00 12 December 2008,

cannot be assessed from these results.

The RMSE values do not take the observational uncertainty into account and that anomaly data could skew the cumulative RMSE. This is likely the case with the final elongation observation of the nose from STEREO-A (refer to Figure 4.3) which is comparable with the flank elongation. As a result, the cumulative RMSE of the feature has a sudden increase despite plateauing for the previous observations. In noting this, the observation data point could be removed. However, since the flank elongation also appears to be lower than would be expected, there is not enough confidence to do this. If only a single time-elongation profile was tracked, this data point would not necessarily be characterised as an anomaly point and would be included in the analysis. Therefore, this observation continues to be considered a valid data point. Furthermore, since an average of time-elongation profiles are being used to assess the model performance, bias caused by anomalous data will be reduced.

6.3.2 Ensemble Results

Figure 6.2 shows the change in the CME L1 arrival time from ensemble analysis as a function of lead time for three ensemble experiments (Experiments 1, 3, and 4; Table 4.2). Following the technique to find the ensemble arrival time in Chapter 4 and 5, the local minimum of the correlation is represented by a solid line whilst the uncertainty of the fit is shown by the shaded region of the same colour.

For MAS-HUXt, with few observations (approximately 82-hour lead time), the CME arrival is estimated $12.9\,\mathrm{h} \pm 8.6\,\mathrm{h}$ after observation. The arrival estimates before an 82-hour lead time appear to be unreliable as the arrival time increases rapidly to much later than observed. As more observations are used, the forecast arrival time gradually becomes earlier and the uncertainty decreases. At a 70-hour lead time, this experiment starts to produce a result in agreement with the observed arrival time. The ensemble estimated arrival continues to become earlier with more HI1 observations. Eventually, from a lead time of 65 hours, the ensemble arrival time is earlier than the observed arrival, however, due to an increase in the ensemble uncertainty at this time, the estimated arrival still agrees with the in-situ observational arrival within the uncertainties.

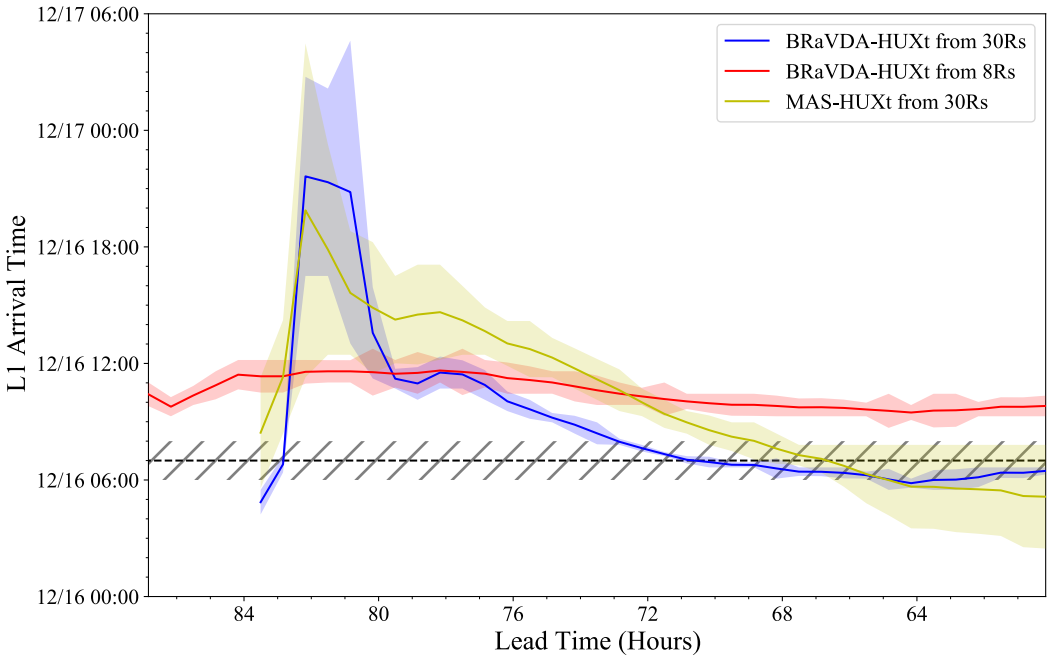

Figure 6.2: The variation in CME L1 arrival time, computed from ensembles, as more HI1 observations are used to assess the HUXt model performance of longitudinal distortion. The timestamp of the "last" HI1 observation has been converted to lead time, based on the difference between the HI1 timestamp and the observed arrival of the 12 December 2008 CME event. The observed arrival was estimated by an increase in solar wind speed at 07:00:00 UTC ± 1 hour, 16 December 2008 displayed as the horizontal grey-shaded region. The BRaVDA-HUXt experiment initialised from an inner boundary height of 30 $R_\odot$ (blue) and 8 $R_\odot$ (red) and the MAS-HUXt experiment from 30 $R_\odot$ (yellow) are shown, with the estimate (solid line) and uncertainty (shaded region) displayed.

For the BRaVDA-HUXt experiment also initiated from 30 $R_\odot$, a similar trend is found. Again, with few observations (82-hour lead time), the ensemble estimates a CME arrival that is in the region of 14.6 h±5.1 h after observation and maintains these respectively high values for a short while. The inclusion of observations following this leads to a quicker decline in the arrival estimate error and uncertainty than seen in the MAS-HUXt ensemble. With a 73-hour lead time, this experiment produces an accurate arrival time estimate and continues to produce an accurate estimate throughout the HI1 field of view. The uncertainty in the arrival time estimate is much smaller than seen in MAS-HUXt; a maximum uncertainty of approximately ± 0.5 h is given by the model from a 75-hour lead time. In addition, the arrival estimate begins to plateau from a lead time of around 68 hours within an hour range.

Given this, it suggests the BRaVDA-HUXt produces a hindcast result of greater reliability.

In contrast, the BRaVDA-HUXt experiment initiated from $8\,R_{\odot}$ shows a very different trend. Due to the inner boundary height being lower than the radial distance view of HI1, the maximum lead time of the hindcast is 87 hours. From the first observation, the ensemble technique produces an estimated arrival $3.4\,\mathrm{h} \pm 0.6\,\mathrm{h}$ later than observed. As seen with the other experiments, there is an increase in the estimate within the first few observations. The latest arrival time estimate obtained here is $4.6\,\mathrm{h} \pm 0.8\,\mathrm{h}$ after the observed arrival with a 78-hour lead time. This is an improvement on the latest arrival estimate from both $30\,R_{\odot}$ experiments by 68 % for BRaVDA-HUXt and 64 % for MAS-HUXt. This arrival time estimate is not classed as a peak in the results, especially as the arrival time estimates following this fluctuate little with time. Throughout the HI1 field of view, the arrival estimates vary between 09:30 - 11:40 UT (16 December) with a near-constant uncertainty (average $\pm 0.6\,\mathrm{h}$). Whilst the stable uncertainty could infer that the output of this experiment is more reliable, it cannot be ignored that all arrival time estimates do not agree with the observed arrival time - i.e., a systematic bias. Such an outcome is possibly unsurprising since in Chapter 5 it was found that the ensemble hindcast produced a later-than-observed arrival. However, the interesting fact that the ensemble arrival estimate did not alter when the CME parameter space was doubled was interpreted as a repercussion of the lower inner boundary set-up and the additional distortion of the modelled CME boundary. It is more likely that the realistic representation of a cone CME at $8\,R_{\odot}$ has allowed the HUXt model to simulate the boundary distortion with better accuracy, as was intended. The relatively constant estimates throughout the whole HI1 field of view does support the method of lowering the inner boundary. But the systematic bias towards a later-than-observed arrival is investigated in the next section with a comparison with in-situ measurements.

In general, the trend of the ensemble estimated arrival time supports the findings of the cumulative RMSE trends of the deterministic runs. With more observations, and thus a better evaluation of the model performance, the estimated ensemble arrival time is more accurate and more reliable.

6.4 Discussion

6.4.1 Signature Detection

As the analysis above shows, an ensemble of BRaVDA-HUXt from 8 $R_\odot$ produces arrival time estimates that vary within a 2 hour window, therefore well constrained, but displaying a systemic bias. Here a detailed comparison of the ensemble arrival time estimates with in-situ measurements is made. But what if, instead, the bias was contained in the estimated arrival time in the in-situ measurements? For three lead time values (84 hours, 72 hours, and 60 hours), ACE measurements of the solar wind speed, proton density, and magnetic field are shown in Figures 6.3, 6.4, and 6.5.

In all three figures, representing a spread of the stable estimates provided by BRaVDA-HUXt from 8 $R_\odot$, the ensemble arrival time is seen to correspond to the beginning of a period of enhanced proton density, and a drop in the B_x and B_y magnetic field. Since HI cameras detect light Thomson scattered from electrons, the time-elongation profiles of the fronts correspond to dense regions of plasma. Therefore, the earlier assignment of observed arrival using an enhancement of solar wind speed (Section 4.1) may contain a systematic bias, here a +3 hour difference between the speed enhancement and the proton density enhancement.

This ambiguity in defining the arrival time of a CME can be seen in the literature as well. For the 12 December 2008 event, studies are fairly confident with the arrival time of the magnetic cloud on 17 December as this is a clearly defined signature in observations (*Zurbuchen and Richardson*, 2006). However, the leading edge arrival is estimated over a broad range, between 07:00 - 18:30 UT 16 December (*Byrne et al.*, 2010; *Davis et al.*, 2009; *Deforest et al.*, 2013a; *Liu et al.*, 2010a; *Zhang et al.*, 2019), with the majority of these estimates occurring before midday. It is noted that estimates for the leading edge feature are often based on reasonably good outcomes of the research's methodology rather than a manual signature detection of in-situ observations. There are online databases of CME arrival times that can be used as a reliable estimate, such as the near-Earth CME list (*Richardson and Cane*, 2010), HELIO4CAST ICME catalogue (*Möstl et al.*, 2017), or the NASA's Community Coordinated Modeling Center Scoreboard (*Riley et al.*, 2018a). However, for this event, the arrival time of the leading edge is either not listed or the data set does

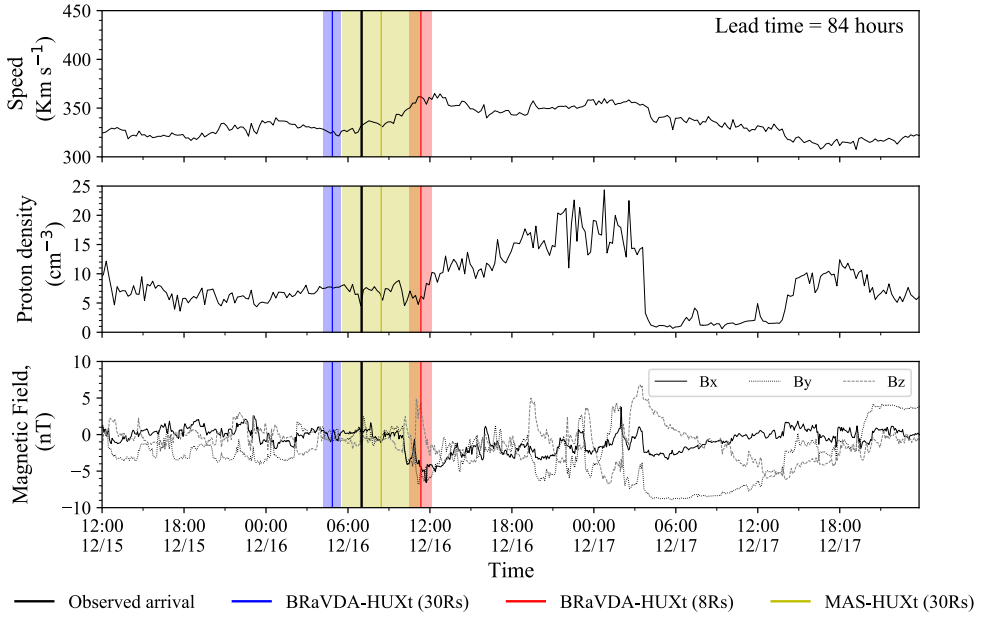

Figure 6.3: Ensemble estimate of CME arrival at L1 from three HUXt experiments, including uncertainty. The ensemble member accuracy has been quantified with an 84-hour lead time (i.e., at least one HI observation of each front).

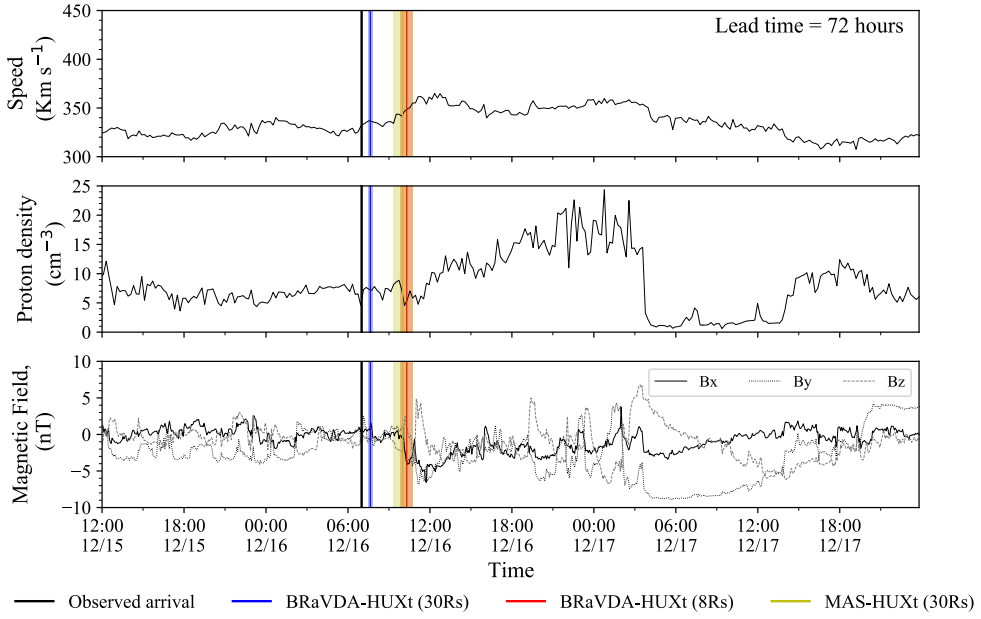

Figure 6.4: Ensemble estimate of CME arrival at L1 from three HUXt experiments, including uncertainty. The ensemble member accuracy has been quantified with a 72-hour lead time.

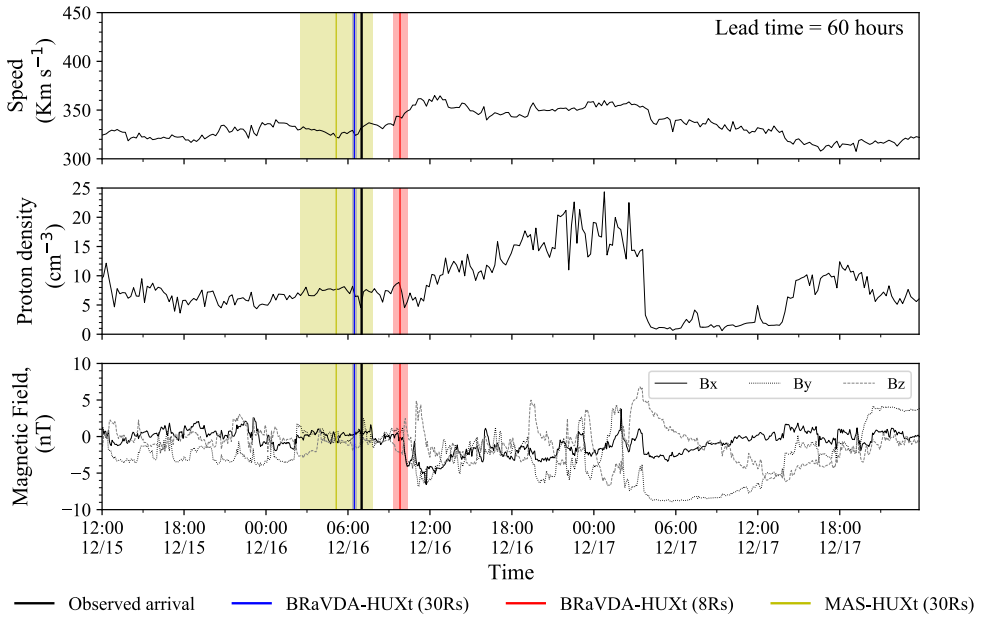

Figure 6.5: Ensemble estimate of CME arrival at L1 from three HUXt experiments, including uncertainty. The ensemble member accuracy has been quantified with a 60-hour lead time (i.e., all HI observations of each front).

not include this event. Therefore, the estimate of the CME arrival given earlier in this thesis is valid, but the uncertainty of the arrival may be larger than originally assigned ($\pm$ 1 hour based on the temporal resolution of the data) if this ambiguity is to be represented.

Using MAS-HUXt ensemble results in a relativity large arrival time uncertainty compared to either BRaVDA-HUXt ensemble runs. At 84-hour lead time, the steady enhancement in speed is the only clear signature within the uncertainty range. At 60-hour lead time, there is no clear signatures of a CME arrival. At 72-hour lead time, where the uncertainty of MAS-HUXt is much smaller and comparable to the size of both BRaVDA-HUXt uncertainties (Figure 6.4), the estimated L1 arrival time is in agreement with the time produced by BRaVDA-HUXt from 8 $R_{\odot}$. And, this corresponds to the enhancement in proton density signature. Despite the variable nature of arrival time estimates produced by MAS-HUXt over the four-day HI1 observation period, it is crucial to highlight that the periods of lowest uncertainty correspond to more accurate estimates. Although the model exhibits a broad range of uncertainties, emphasising the challenges in prediction, instances of minimal

uncertainty are indicative of heightened accuracy.

6.4.2 Important factors to lead time forecasting

Exploring how HI1 observations can aid the lead time of CME forecasts reveals several factors which could be beneficial to improving the results; the radial distance of observations, the number of observations, the position of the STEREO spacecraft, the interpretation of bright fronts in HI images, and the use of multi-spacecraft observations. Further work would be required to assess the sensitivity of these factors.

In the future, there are plans for a CME-observing spacecraft orbiting at the Lagrange 5 (Vigil) point, 60° from the Sun-Earth line (*Vourlidas*, 2015) after a number of studies have suggested this would be useful for forecasting (e.g. *Akioka et al.*, 2005; *Rodriguez et al.*, 2020; *Thomas et al.*, 2018). Understanding how HI observations could be interpreted from this position would be of most advantage, and the 12 December 2008 case study is a reasonable demonstration ($-44°$). From a single spacecraft, multiple time-elongation profiles (from the CME nose and flank) are not guaranteed. Thus, understanding how forecasts vary with lead time using the flank only would be most useful since the flank feature is always visible in HI images (e.g. *Barnard et al.*, 2020; *Möstl et al.*, 2010).

With the analysis of a single CME event, as presented here, it is not possible to determine whether the radial distance of the CME or frequency of observations is important. This could be investigated by applying the method to a fast CME scenario, where the travel time through the HI1 field of view is reduced, resulting in fewer observations.

6.4.3 Is it beneficial to use Ghost Front theory?

In the analysis, the fitting to HI1 observations has been optimised by using the elongation profiles of all four bright fronts seen in the images from STEREO A and STEREO B using the ghost front theory (*Scott et al.*, 2019). Chapter 4.1 found that the time-elongation profiles of the nose and flank were in good agreement with the HI1 observation and also produced an appropriate L1 arrival time estimate based on in-situ observations. Without the nose feature, the technique was unable to produce a viable L1 arrival time estimate. As seen in Figure 6.1a, the RMSE of the flank

and nose features were vastly different, especially from STEREO-B, and the ghost front theory provided a constraint. The findings in Chapter 5 found that tracking the flank only was sufficient to provide a viable L1 arrival time estimate (as well as using the ghost front). The results in Figure 6.1b support this as the time elongation profiles of the two features perform similarly and therefore there is little additional benefit to applying the ghost front theory although using the ghost front theory is not detrimental to the outcome. Moreover, only by applying the ghost front theory did the ensemble estimate produce a consistent arrival time regardless of the CME inner boundary parameter space. As found in this chapter, the arrival time estimate did not vary significantly with additional HI1 observations to constrain the model, thus, the lead time in which a theoretical forecast could be made is increased.

This ghost front case study indicates that there is a benefit to having multiple time-elongation profiles in CME modelling. But more work is required to know the limitations of this technique and the confidence of the conclusions when applied to a statistical study of CMEs with a range of speeds, longitudinal widths and viewing geometries.

6.5 Summary

In this chapter, the quantity of HI1 observations that are required to provide a measure of model performance has been assessed. By the assumption that the two bright fronts tracked through the HI1 field of view correspond to the time-elongation profiles of the nose and furthest flank from the observer, the cumulative RMSE between model and observation is evaluated for all available observations. For the 12 December 2008 event, 41 HI1 observations are available. Only 36 observations are viable when computing HUXt from a $30\,R_\odot$ inner boundary due to this radial distance being within the HI1 field of view, but all observations can be used when the boundary is lowered to $8\,R_\odot$.

Three ensemble experiments are presented here; MAS-HUXt from $30\,R_\odot$, BRaVDA-HUXt from $30\,R_\odot$, and BRaVDA-HUXt from $8\,R_\odot$. Experiments initialised from $30\,R_\odot$ have a similar trend in forecasting accuracy with time. For lead times of 82 hours or more, the estimated arrival is approximately 13 h to 15 h later than the observed arrival with an ± 8 h to 9 h uncertainty. For lead times less

than 82 hours, the estimate declines toward the observed arrival with the addition of more HI1 observations. For MAS-HUXt, the arrival estimate with the smallest uncertainty minimises at a 70-hour lead time and corresponds to the in-situ arrival (based on the 07:00 UT ± 1 hour solar wind speed enhancement in ACE data on 16 December). From there, the uncertainty increases while the ATE estimate continues to decline throughout the remainder of HI-1 observations. Meanwhile, BRaVDA-HUXt maintains an arrival estimate in line with in-situ arrival from a 73-hour lead time and plateaus about the observed arrival time. A BRaVDA-HUXt ensemble where the CME was initiated from 8 $R_\odot$ was also included in the analysis. In this case, the CME arrival estimate is almost constant (averaging around 10:00 UT on 16 December) despite including more HI1 observations. Compared with the in-situ ACE data, the estimated arrival times from this ensemble analysis corresponds to the beginning of a period of enhanced proton density.

By using an ensemble approach, HI1 observations can provide a means to weight ensemble members based on the agreement between the observed and modelled time-elongation profiles. The technique applied here idealises a real-time forecast method whereby the HUXt model can initialise a CME ensemble simulation based on COR observations and, with the availability of each new HI observation, recompute the analysis to produce an updated forecast. In this case, several forecasts could be produced with an 86 h to 60 h lead time, for an intermediate-speed CME. Currently, the HI instruments at 1 AU are only available on the STEREO science mission, where high-resolution data is available 3 days after observation. Near-real time data availability is assumed on future, forecast-focused missions.

These results look at a single case study. For a faster CME event, there would be fewer HI1 observations available. However, obtaining observations from a range of radial distances may be more significant than the total number of available observations. This may be because observations furthest from the Sun contain cumulative information on the leading edge distortion resulting from the propagation of the CME through the structured solar wind of the inner heliosphere.

Chapter 7

Conclusion

This thesis has tested a technique for using *Heliospheric Imager* (HI) data to infer the longitudinal shape of a CME through comparison of observed and modelled 'ghost fronts'. Highlighting regions of dense plasma in the heliosphere, fronts that lead and encase the majority of the CME material are observed in HI, giving a two-dimensional estimate of the transient's shape as a function of latitude. In some cases, nearly-identical fronts separated by a few degrees in elongation are seen, inferred as two regions of the CME leading edge under the ghost front theory (*Scott et al.*, 2019). Thomson scattering suggests bright features can be observed in HI images due to a locally dense plasma region or a large cumulative density of plasma along the line of sight of the observer. Respectively, this can occur at the nose of the CME and along the furthest flank from the observer.

A preliminary study is presented; the 12 December 2008 CME is one event which produced two leading fronts through the HI1 field of view. Modelling the CME and identifying the two ghost front features, the time-elongation profiles of the flank and nose were shown to correspond well with the spacecraft observations in Chapter 4.

HUXt, a reduced-physics solar wind model, is used to simulate the CME heliospheric propagation throughout the thesis. Despite the reduced-physics approach, the model is a great surrogate to MHD models used operationally and can be used

to generate large-member ensembles due to its computational efficiency. From inner boundary conditions, the solar wind is modelled as a purely radial outflow in one dimension and CMEs are initialised as velocity pulses with a cone-CME constraint. Simulation of the heliosphere is completed in the Sun-Earth plane, allowing the L1 arrival time and speed estimates to be obtained.

Solar wind speed is one of the inner boundary conditions explored in the work. A data assimilation scheme, BRaVDA, uses *Advanced Composition Explorer* (ACE) measurements to improve the solution of the solar wind speed at a radial distance of $30\,R_\odot$ during CR2077. At L1, the ambient solar wind speed was shown to be more representative of the in-situ profile and improved the CME arrival time by 5.5 h in comparison with the non-data assimilated MAS solution.

HUXt ensembles of 201 members are generated by purturbing the inner boundary conditions of the CME within the uncertainty of *Coronagraph* (COR) parameter estimates. Evaluation of the ghost front features' elongation variation with time against the HI1 observations, via Root-Mean-Square-Error (RMSE) measurement, provides a method of quantifying the accuracy of CME longitudinal distortion. When all ensemble members were plotted, a quadratic relationship was found between RMSE and the L1 arrival time. The minima, fitted to ensemble members with the lowest RMSE values in each arrival time bin, provided an ensemble estimate of the CME arrival time. Initialising CMEs from a $30\,R_\odot$ inner boundary height was the focus of Chapter 4. The ensemble arrival time estimate was in reasonable agreement with the observed arrival, with an error of $0.5\,\mathrm{h} \pm 0.2\,\mathrm{h}$ and $2.1\,\mathrm{h} \pm 0.5\,\mathrm{h}$ depending on initial condition parameter space size and assuming the ghost front theory. Similarly, this analysis of HI observations could be used as an assessment of member skill (*Harrison et al.*, 2009; *Murray*, 2018) and applied to CME modelling as a weighted ensemble technique (as seen in *Barnard et al.*, 2020).

In Chapter 5, the methodology was extended to a lowered inner boundary height of $8\,R_\odot$ at which COR observations are made. Cone-CME constraints are more realistic to the near-Sun loop-like structure. Thus, this technique removes the usual assumption of no CME distortion between COR observations and typical heliospheric inner boundary heights. Here, the ensemble arrival time errors increased to $2.8\,\mathrm{h} \pm 0.5\,\mathrm{h}$ and $2.9\,\mathrm{h} \pm 0.6\,\mathrm{h}$, but a near-identical estimate despite a change in

initial condition parameter space. Moreover, these estimates were an improvement on the deterministic arrival time. This was achieved using ghost front theory. This novel use of the HUXt model assumes a simplification in physical processes within the heliosphere at close radial distances. One of these simplifications is the solar wind residual acceleration parameter constant ($\alpha = 0.15$ in line with *Riley and Lionello*, 2011) that was verified suitable for an inner boundary height of $8\,R_\odot$ *Bunting and Morgan* (2023). Future research could benefit from investigating how this acceleration parameter influences the propagation of CMEs from $8\,R_\odot$. In the study by *Bunting and Morgan* (2023), inner boundary solar wind conditions were inferred from coronal electron density using tomography (CorTom *Bunting and Morgan*, 2022; *Morgan and Cook*, 2020). The back-mapping of $30\,R_\odot$ conditions technique, applied in Chapter 5 of this thesis, is an alternative method that by-passes the complication of solar wind acceleration as, essentially, the CME is only given extra distance to travel from initiation and the solar wind is mapped to be a near-equal array at the original boundary. The manual enhancement of CME initial speed, to compensate for no near-Sun acceleration of the CME within the model, was not independent of the HI1 time-elongation profiles used to assess the model's longitudinal distortion accuracy. In the future, a new method, that does not rely on the test data, would be desirable.

This research concludes that HI observations can be beneficial in constraining ensemble modelling. Furthermore, ghost fronts strengthened the evaluation of model performance from $30\,R_\odot$ yet provided no additional constraint when modelling a CME from $8\,R_\odot$. Chapter 6 has concentrated on studying the quantity of HI observations that is required in order to provide an accurate estimate of CME arrival time and speed at L1. By evaluating ensemble member model performance against an increasing number of HI observations as the event propagates, the L1 arrival time estimate was recalculated. From $30\,R_\odot$, an accurate arrival was obtained with 70 h to 60 h lead time for the mid-speed CME used in this study, regardless of solar wind speed solution. Initialising a CME from $8\,R_\odot$ produced a consistent arrival estimate from a 86 h lead time as the inclusion of more HI observations had very little impact on the ensemble estimated arrival time. The analysis indicates this is caused by a systematic bias. Compared with the ACE in-situ data, the $8\,R_\odot$ BRaVDA-HUXt arrival time corresponded to the beginning of the plasma density enhancement, which

is consistent with the plasma density enhancements generating fronts in HI images.

This thesis presents only a single case study, and the conclusions may alter when considering a larger statistical sample. The geometry of the observer with respect to the CME is expected to impact the ability to use the ghost front interpretation of multiple fronts in HI. For the 12 December 2008 event, the nose and furthest flank were visible in the HI1 field of view whilst the observing spacecraft was positioned 42° and 44° from the Sun-Earth line. This would not be expected whilst an observer is $\geq \pm 90°$ from the line of radial propagation. In preparation for the proposed forecasting mission to orbit at L5 (e.g. ESA's Vigil L5 mission *Vourlidas*, 2015), it would be of interest to explore the ghost front geometry from an Earth-Spacecraft separation of $\pm 60°$.

Using four different CME events, *Barnard et al.* (2020) concluded a non-linear trend between the accuracy of CME flank time-elongation simulation and the CME arrival time when observed from STEREO spacecraft both individually and combined. This is a similar result to the findings presented here suggesting the method could be applied to a statistical study of ghost fronts, assessing variations with CME speed and size. From the period of 2008 - 2014, STEREO HI captured another 75 Earth-impacting ghost-front CME events, according to a survey by volunteers of the Solar Stormwatch project. Some of these are fast CMEs which may include leading shock fronts in the HI observations. A shock front feature was not a characteristic of the CME presented in this thesis. In future work, it would be crucial to understand how the inclusion of a leading shock front would impact the observational data (i.e., are shock fronts clearly distinguishable from ghost front features?). Furthermore, the need for robust and consistent assessments of model accuracy has been highlighted within the Space Weather community, including multiple error measurements to ease comparability (*Verbeke et al.*, 2019). A statistical study of ghost fronts would provide this.

Throughout the writing of this thesis, the development of the HUXt model has continued. Now on version 4.0.0, new and improved functionality expands the possibilities of this work (*Barnard et al.*, 2022). Rather than identifying a $\geq 20\,\mathrm{km\,s^{-1}}$ difference to the ambient solution, the CME boundary is marked out with tracer particles at the inner boundary that advects through the heliospheric

simulation. As such, this technique does not have speed limitations. Tracing in three dimensions has been included as well, therefore, ghost front application can be explored across multiple latitudes, which has been shown in the preliminary study of *Chi et al.* (2021). Forecasting the magnetic field, in particular the direction of the B_z component, is essential for estimating the geomagnetic impact of a CME. Whilst the mapping of solar wind magnetic field streamlines has been included in the latest HUXt release, the CME remains a magnetic-free perturbation. Thus, coupling the output of HUXt with a full-physics MHD model would enable the investigation of magnetic parameters.

It is the nature of research that there is usually more that needs to be done than can be achieved in a single project. Some further work suggestions have been included already; some could be the next steps off the back of this research, and others would be long-term and depend on future space missions. The most obvious extensions to the work presented here are;

- A robust method of identifying the lowest subset of ensemble members to which the ensemble estimate is produced. This could be achieved using a clustering algorithm.
- Explore the sensitivity of initial parameters and infer the dependency of these.
- Increase the number of ensemble members to investigate how the results vary and possibly define an optimum ensemble size. This could be easily achieved with a computationally efficient model like HUXt.
- Extend to a statistically significant set of CME observations covering a range of CME speeds, widths and viewing geometries.

As current CME forecasting models (e.g. ENLIL) have an inner boundary height of $30\,R_\odot$, the work presented in this thesis strongly suggests HI time-elongation profiles inferred with the ghost front theory can provide additional model constraints when using an inner boundary significantly higher than the coronagraph observations used to constrain the CME. Future missions require a much lower latency in data availability in order to use multiple techniques to optimise CME modelling, as planned on forecasting-focused missions. With the launch of ESA's Vigil mission

expected in the next five years, an improvement in observations, CME modelling and, thus, space weather science is imminent.

References

Adhikari, L., G. P. Zank, and L.-L. Zhao, Does turbulence turn off at the alfvén critical surface?, *The Astrophysical Journal*, *876*, 26, doi:10.3847/1538-4357/ab141c, 2019.

Akioka, M., T. Nagatsuma, W. Miyake, K. Ohtaka, and K. Marubashi, The l5 mission for space weather forecasting, *Advances in Space Research*, *35*, 65--69, doi:10.1016/j.asr.2004.09.014, 2005.

Alfvén, H., Existence of electromagnetic-hydrodynamic waves, *Nature*, *150*, 405--406, doi:10.1038/150405d0, 1942.

Altschuler, M. D., and G. Newkirk, Magnetic fields and the structure of the solar corona, *Solar Physics*, *9*, 131--149, doi:10.1007/BF00145734, 1969.

Amari, T., J. J. Aly, Z. Mikic, and J. Linker, Coronal mass ejection initiation and complex topology configurations in the flux cancellation and breakout models, *The Astrophysical Journal*, *671*, L189--L192, doi:10.1086/524942, 2007.

Amerstorfer, T., C. Möstl, P. Hess, M. Temmer, M. L. Mays, M. A. Reiss, P. Lowrance, and P. A. Bourdin, Ensemble prediction of a halo coronal mass ejection using heliospheric imagers, *Space Weather*, *16*, 784--801, doi:10.1029/2017SW001786, 2018.

Amerstorfer, T., et al., Evaluation of cme arrival prediction using ensemble modeling based on heliospheric imaging observations, *Space Weather*, *19*, doi:10.1029/2020SW002553, 2021.

Antiochos, S. K., C. R. DeVore, and J. A. Klimchuk, A model for solar coronal mass ejections, *The Astrophysical Journal*, *510*, 485--493, doi:10.1086/306563, 1999.

Arge, C. N., J. G. Luhmann, D. Odstrcil, C. J. Schrijver, and Y. Li, Stream structure and coronal sources of the solar wind during the may 12th, 1997 cme, *Journal of Atmospheric and Solar-Terrestrial Physics*, *66*, 1295--1309, doi:10.1016/j.jastp.2004.03.018, 2004.

Aschwanden, M. J., A. Winebarger, D. Tsiklauri, and H. Peter, The coronal heating paradox, *The Astrophysical Journal*, *659*, 1673--1681, 2007.

B. J. Lynch, P. J. M. T. H. Z., S. K. Antiochos, and L. A. Fisk, Observable properties of the breakout model for coronal mass ejections, *The Astrophysical Journal*, p. 589–599, doi:10.1086/424564, 2004.

Bandyopadhyay, R., et al., Sub-alfvénic solar wind observed by the parker solar probe: Characterization of turbulence, anisotropy, intermittency, and switchback, *The Astrophysical Journal Letters*, *926*, L1, doi:10.3847/2041-8213/ac4a5c, 2022.

Barnard, L., M. J. Owens, C. J. Scott, and C. A. Koning, Ensemble cme modeling constrained by heliospheric imager observations, *AGU Advances*, *1*, doi:10.1029/2020av000214, 2020.

Barnard, L., M. Owens, C. Scott, M. Lang, and M. Lockwood, Sir-huxt—a particle filter data assimilation scheme for cme time-elongation profiles, *Space Weather*, *21*(6), e2023SW003,487, doi:https://doi.org/10.1029/2023SW003487, e2023SW003487 2023SW003487, 2023.

Barnard, L., et al., Quantifying the uncertainty in cme kinematics derived from geometric modeling of heliospheric imager data, *Space Weather*, *20*, doi:10.1029/2021SW002841, 2022.

Barnard, L. A., C. A. de Koning, C. J. Scott, M. J. Owens, J. Wilkinson, and J. A. Davies, Testing the current paradigm for space weather prediction with heliospheric imagers, *Space Weather*, *15*, 782--803, doi:10.1002/2017SW001609, 2017.

Billings, D., *A Guide to the Solar Corona*, 344 pp., Academic Press, 1966.

Bolduc, L., Gic observations and studies in the hydro-québec power system, *Journal of Atmospheric and Solar-Terrestrial Physics*, *64*, 1793--1802, doi:10.1016/S1364-6826(02)00128-1, 2002.

Boteler, D. H., Modeling geomagnetic interference on railway signaling track circuits, *Space Weather*, *19*, doi:10.1029/2020SW002609, 2021.

Bougeret, J. L., et al., S/waves: The radio and plasma wave investigation on the stereo mission, *Space Science Reviews*, *136*, 487--528, doi:10.1007/s11214-007-9298-8, 2008.

Braga, C. R., A. Vourlidas, G. Stenborg, A. D. Lago, R. R. S. de Mendonça, and E. Echer, Predicting the time of arrival of coronal mass ejections at earth from heliospheric imaging observations, *Journal of Geophysical Research: Space Physics*, *125*, 1--25, doi:10.1029/2020ja027885, 2020.

Browning, M., M. S. Miesch, A. S. Brun, and J. Toomre, Dynamo action in the solar convection zone and tachocline: Pumping and organization of toroidal fields, *The Astrophysical Journal*, doi:10.1086/507869, 2006.

Bunting, K. A., and H. Morgan, An inner boundary condition for solar wind models based on coronal density, *Journal of Space Weather and Space Climate*, *12*, doi:10.1051/swsc/2022026, 2022.

Bunting, K. A., and H. Morgan, An empirical relationship between coronal density and solar wind velocity in the middle corona with applications to space weather, *Space Weather*, *21*, doi:10.1029/2023SW003448, 2023.

Burch, J. L., and J. F. Drake, Reconnecting magnetic fields: The huge amounts of energy released from the relinking of magnetic fields in outer space are both mysterious and potentially destructive, `https://www.jstor.org/stable/27859391`, 2009.

Byrne, J. P., S. A. Maloney, R. T. McAteer, J. M. Refojo, and P. T. Gallagher, Propagation of an earth-directed coronal mass ejection in three dimensions, *Nature Communications*, *1*, doi:10.1038/ncomms1077, 2010.

Cabinet, O., Ccs's national risk register 2020, *Tech. rep.*, HM Government, 2020.

Cameron, R. H., M. Dikpati, and A. Brandenburg, The global solar dynamo, *Space Science Reviews*, *210*, 367--395, doi:10.1007/s11214-015-0230-3, 2017.

Cane, H. V., and I. G. Richardson, Coronal mass ejections, interplanetary ejecta and geomagnetic sotrms, *Journal of Geophysical Research: Space Physics*, *27*, 3591--3594, 2000.

Cannon, P., Extreme space weather: impacts on engineered systems and infrastructures, *Tech. rep.*, The Royal Academy of Engineering, UK, 2013.

Cargill, P., C. Parnell, P. Browning, I. D. Moortel, and A. Hood, Magnetic reconnection in the solar atmosphere: from proposal to paradigm, *Astronomy & Geophysics*, *51*, 3.31--3.35, doi:10.1111/j.1468-4004.2010.51331.x, 2010.

Cargill, P. J., On the aerodynamic drag force acting on interplanetary coronal mass ejections, *Solar Physics*, *221*, 135--149, doi:10.1023/B:SOLA.0000033366.10725.a2, 2004.

Carrington, R. C., Description of a singular appearance seen in the sun on september 1, 1859, *Monthly Notices of the Royal Astronomical Society*, *20*, 13--15, doi:10.1093/mnras/20.1.13, 1859.

Cash, M. D., D. A. Biesecker, V. Pizzo, C. A. D. Koning, G. Millward, C. N. Arge, C. J. Henney, and D. Odstrcil, Ensemble modeling of the 23 july 2012 coronal mass ejection, *Space Weather*, *13*, 611--625, doi:10.1002/2015SW001232, 2015.

Chen, P. F., Coronal Mass Ejections: Models and Their Observational Basis, *Living Reviews in Solar Physics*, *8*(1), 1, doi:10.12942/lrsp-2011-1, 2011.

Chi, Y., et al., Modeling the observed distortion of multiple (ghost) cme fronts in stereo heliospheric imagers, *The Astrophysical Journal Letters*, *917*, L16, doi:10.3847/2041-8213/ac1203, 2021.

Colaninno, R. C., and A. Vourlidas, First determination of the true mass of coronal mass ejections: A novel approach to using the two stereo viewpoints, *Astrophysical Journal*, *698*, 852--858, doi:10.1088/0004-637X/698/1/852, 2009.

Davies, J. A., et al., A synoptic view of solar transient evolution in the inner heliosphere using the heliospheric imagers on stereo, *Geophysical Research Letters*, *36*, doi:10.1029/2008GL036182, 2009.

Davies, J. A., et al., A self-similar expansion model for use in solar wind transient propagation studies, *Astrophysical Journal*, *750*, doi:10.1088/0004-637X/750/1/23, 2012.

Davis, C. J., J. A. Davies, M. Lockwood, A. P. Rouillard, C. J. Eyles, and R. A. Harrison, Stereoscopic imaging of an earth-impacting solar coronal mass ejection: A major milestone for the stereo mission, *Geophysical Research Letters*, *36*, 1--5, doi:10.1029/2009GL038021, 2009.

Deforest, C. E., T. A. Howard, and D. J. McComas, Disconnecting open solar magnetic flux, *Astrophysical Journal*, *745*, doi:10.1088/0004-637X/745/1/36, 2012.

Deforest, C. E., T. A. Howard, and D. J. McComas, Tracking coronal features from the low corona to earth: A quantitative analysis of the 2008 december 12 coronal mass ejection, *Astrophysical Journal*, *769*, doi:10.1088/0004-637X/769/1/43, 2013a.

Deforest, C. E., T. A. Howard, and S. J. Tappin, The thomson surface. ii. polarization, *Astrophysical Journal*, *765*, doi:10.1088/0004-637X/765/1/44, 2013b.

DeForest, C. E., T. A. Howard, and D. J. McComas, Inbound waves in the solar corona: A direct indicator of alfvÉn surface location, *The Astrophysical Journal*, *787*, 124, doi:10.1088/0004-637X/787/2/124, 2014.

Department for Business, Innovation and Skills, Uk severe space weather preparedness strategy, `https://assets.publishing.service.gov.uk/government/uploads/system/uploads/attachment_data/file/1020551/uk-severe-space-weather-preparedness-strategy.pdf`, 2021.

Dungey, J., Lxxvi. conditions for the occurrence of electrical discharges in astrophysical systems, *The London, Edinburgh, and Dublin Philosophical Magazine and Journal of Science*, *44*, 725--738, doi:10.1080/14786440708521050, 1953.

European Space Agency, Space weather effects, `https://www.esa.int/ESA_Multimedia/Images/2018/01/Space_weather_effects`, 2018.

Eyles, C. J., et al., The heliospheric imagers onboard the stereo mission, *Solar Physics*, *254*, 387--445, doi:10.1007/s11207-008-9299-0, 2009.

Galilei, G., *Istoria e Dimostrazioni Intorno alle Macchie Solari*, 1613.

Galvin, A. B., et al., The plasma and suprathermal ion composition (plastic) investigation on the stereo observatories, *Space Science Reviews*, *136*, 437--486, doi:10.1007/s11214-007-9296-x, 2008.

Gary, G. A., Plasma beta above a solar active region: Rethinking the paradigm, *Solar Physics*, *203*, 71--86, doi:10.1023/A:1012722021820, 2001.

Geiss, J., G. Gloeckler, and R. von Steiger, Origin of the Solar Wind From Composition Data, , *72*(1-2), 49--60, doi:10.1007/BF00768753, 1995.

Gibney, E., Space-weather forecast to improve with european satellite, *Nature*, doi:10.1038/541271a, 2017.

Gopalswamy, N., A. Lara, R. P. Lepping, M. L. Kaiser, D. Berdichevsky, and O. C. S. Cyr, Interplanetary acceleration of coronal mass ejections, *Geophysical Research Letters*, *27*, 145--148, doi:10.1029/1999GL003639, 2000.

Gopalswamy, N., A. Lara, S. Yashiro, M. L. Kaiser, and R. A. Howard, Predicting the 1-au arrival times of coronal mass ejections, *Journal of Geophysical Research: Space Physics*, *106*, 29,207--29,217, doi:10.1029/2001ja000177, 2001.

Gosling, J. T., The solar flare myth, *Journal of Geophysical Research: Space Physics*, *98*, 18,937--18,949, doi:10.1029/93ja01896, 1993.

Gosling, J. T., S. J. Bame, D. J. McComas, and J. L. Phillips, Coronal mass ejections and large geomagnetic storms, *Geophysical Research Letters*, *17*, 901--904, doi:10.1029/GL017i007p00901, 1990.

Gosling, J. T., J. Birn, and M. Hesse, Three-dimensional magnetic reconnection and the magnetic topology of coronal mass ejection events, *Geophysical Research Letters*, *22*, 869--872, doi:10.1029/95GL00270, 1995.

Green, J. C., J. Likar, and Y. Shprits, Impact of space weather on the satellite industry, *Space Weather*, *15*, 804--818, doi:10.1002/2017SW001646, 2017.

Guerrero, G., P. K. Smolarkiewicz, E. M. de Gouveia Dal Pino, A. G. Kosovichev, and N. N. Mansour, On the role of tachoclines in solar and stellar dynamos, *The Astrophysical Journal*, *819*, 104, doi:10.3847/0004-637X/819/2/104, 2016.

Hands, A. D. P., K. A. Ryden, N. P. Meredith, S. A. Glauert, and R. B. Horne, Radiation effects on satellites during extreme space weather events, *Space Weather*, *16*, 1216--1226, doi:10.1029/2018SW001913, 2018.

Hapgood, M., and A. Thomson, Space weather. its impact on earth and implications for business, *Tech. rep.*, Lloyds, 2018.

Hapgood, M., et al., Development of space weather reasonable worst-case scenarios for the uk national risk assessment, *Space Weather*, *19*, doi:10.1029/2020SW002593, 2021.

Harrison, R. A., J. A. Davies, D. Biesecker, and M. Gibbs, The application of heliospheric imaging to space weather operations: Lessons learned from published studies, *Space Weather*, *15*, 985--1003, doi:10.1002/2017SW001633, 2017.

Harrison, R. A., et al., Two years of the stereo heliospheric imagers : Iiiinvited review, *Solar Physics*, *256*, 219--237, doi:10.1007/s11207-009-9352-7, 2009.

Harrison, R. A., et al., An analysis of the origin and propagation of the multiple coronal mass ejections of 2010 august 1, *The Astrophysical Journal*, *750*, 45, doi:10.1088/0004-637X/750/1/45, 2012.

Hathaway, D. H., The solar cycle, *Living Reviews in Solar Physics*, *12*, doi:10.1007/lrsp-2015-4, 2015.

Henley, E. M., and E. C. Pope, Cost-loss analysis of ensemble solar wind forecasting: Space weather use of terrestrial weather tools, *Space Weather*, *15*, 1562--1566, doi:10.1002/2017SW001758, 2017.

Hesse, M., and P. A. Cassak, Magnetic reconnection in the space sciences: Past, present, and future, *Journal of Geophysical Research: Space Physics*, *125*, doi:10.1029/2018ja025935, 2020.

Hinterreiter, J., et al., Why are elevohi cme arrival predictions different if based on stereo-a or stereo-b heliospheric imager observations?, *Space Weather*, pp. 1--18, doi:10.1029/2020sw002674, 2021.

Howard, T., *Space Weather and Coronal Mass Ejections*, Springer New York, doi:10.1007/978-1-4614-7975-8, 2014.

Howard, T. A., and C. E. Deforest, Inner heliospheric flux rope evolution via imaging of coronal mass ejections, *Astrophysical Journal*, *746*, doi:10.1088/0004-637X/746/1/64, 2012a.

Howard, T. A., and C. E. Deforest, The thomson surface. i. reality and myth, *Astrophysical Journal*, *752*, doi:10.1088/0004-637X/752/2/130, 2012b.

Howard, T. A., S. J. Tappin, D. Odstrcil, and C. E. Deforest, The thomson surface. iii. tracking features in 3d, *Astrophysical Journal*, *765*, doi:10.1088/0004-637X/765/1/45, 2013.

Illing, R. M. E., and A. J. Hundhausen, Observation of a coronal transient from 1.2 to 6 solar radii, *Journal of Geophysical Research: Space Physics*, *90*, 275--282, doi:10.1029/JA090iA01p00275, 1985.

Iwai, K., D. Shiota, M. Tokumaru, K. Fujiki, M. Den, and Y. Kubo, Validation of coronal mass ejection arrival-time forecasts by magnetohydrodynamic simulations based on interplanetary scintillation observations, *Earth, Planets and Space*, *73*, 1--17, doi:10.1186/s40623-020-01345-5, 2021.

James, L. A., C. J. Scott, L. A. Barnard, M. J. Owens, M. S. Lang, and S. R. Jones, Sensitivity of model estimates of cme propagation and arrival time to inner boundary conditions, *Space Weather*, *21*, doi:10.1029/2022SW003289, 2023.

Jones, S. R., C. J. Scott, L. A. Barnard, R. Highfield, C. J. Lintott, and E. Baeten, The visual complexity of coronal mass ejections follows the solar cycle, *Space Weather*, *18*, doi:10.1029/2020SW002556, 2020.

Ju Jing, J. L. H. J. N. L. Y. X., Chang Liu, and H. Wang, Statistical analysis of torus and kink instabilities in solar eruptions, *The Astrophysical Journal*, *825*(2), doi:10.3847/1538-4357/aad6e4, 2018.

Kaiser, M. L., T. A. Kucera, J. M. Davila, O. C. S. Cyr, M. Guhathakurta, and E. Christian, The stereo mission: An introduction, *Space Science Reviews*, *136*, 5--16, doi:10.1007/s11214-007-9277-0, 2008.

Kay, C., M. Opher, and R. M. Evans, Global trends of cme deflections based on cme and solar parameters, *Astrophysical Journal*, *805*, 168, doi:10.1088/0004-637X/805/2/168, 2015.

Kay, C., N. Gopalswamy, A. Reinard, and M. Opher, Predicting the magnetic field of earth-impacting cmes, *The Astrophysical Journal*, *835*, 117, doi:10.3847/1538-4357/835/2/117, 2017.

Kilpua, E., N. Lugaz, M. L. Mays, and M. Temmer, Forecasting the structure and orientation of earthbound coronal mass ejections, *Space Weather*, *17*, 498--526, doi:10.1029/2018SW001944, 2019.

Kirnosov, Vladimir, Chang, Lin-Ching, and Pulkkinen, Antti, Combining stereo secchi cor2 and hi1 images for automatic cme front edge tracking, *J. Space Weather Space Clim.*, *6*, doi:10.1051/swsc/2016037, 2016.

Klein, L. W., and L. F. Burlaga, Interplanetary magnetic clouds at 1 au, *Journal of Geophysical Research*, *87*, 613, doi:10.1029/JA087iA02p00613, 1982.

Kliem, B., and T. Török, Torus instability, *Physical Review Letters*, *96*(25), doi:10.1103/PhysRevLett.96.255002, 2006.

Koga, D., W. D. Gonzalez, V. M. Souza, F. R. Cardoso, C. Wang, and Z. K. Liu, Dayside magnetopause reconnection: Its dependence on solar wind and magnetosheath conditions, *Journal of Geophysical Research: Space Physics*, *124*, 8778--8787, doi:10.1029/2019JA026889, 2019.

Koning, C. A. D., V. J. Pizzo, and D. A. Biesecker, Geometric localization of cmes in 3d space using stereo beacon data: First results, *Solar Physics*, *256*, 167--181, doi:10.1007/s11207-009-9344-7, 2009.

Koons, H., J. Mazur, S. Selesnick, J. Blake, J. Fennell, J. Roeder, and P. Anderson, The impact of the space environment on space systems, 1999.

Krausmann, E., E. Andersson, W. Murtagh, and N. Mitchison, Space weather and power grids: Findings and outlook, EGU General Assembly Conference Abstracts, doi:10.2788/42160, 2013.

Krausmann, E., E. Andersson, T. Russel, and W. Murtagh, Space weather and rail: Findings and outlook, *Publications Office of the European Union*, doi:10.2788/211456, 2015.

Kumar, P., K. S. Cho, S. C. Bong, S.-H. Park, and Y. H. Kim, Initiation of coronal mass ejection and associated flare caused by helical kink instability observed by sdo/aia, *The Astrophysical Journal*, *746*(1), doi:10.1088/0004-637X/746/1/67, 2012.

Lang, M., and M. J. Owens, A variational approach to data assimilation in the solar wind, *Space Weather*, *17*, 59--83, doi:10.1029/2018SW001857, 2019.

Lang, M., J. Witherington, H. Turner, M. J. Owens, and P. Riley, Improving solar wind forecasting using data assimilation, *Space Weather*, *19*, doi:10.1029/2020SW002698, 2021.

Lee, C. O., C. N. Arge, D. Odstrčil, G. Millward, V. Pizzo, J. M. Quinn, and C. J. Henney, Ensemble modeling of cme propagation, *Solar Physics*, *285*, 349--368, doi:10.1007/s11207-012-9980-1, 2013.

Li, X., Y. Wang, J. Guo, R. Liu, and B. Zhuang, Radial velocity map of solar wind transients in the field of view of stereo/hi1 on 3 and 4 april 2010, *Astronomy and Astrophysics*, *649*, doi:10.1051/0004-6361/202039766, 2021.

Lin, C., and J. Chen, Drag force on coronal mass ejections (cmes), *Journal of Geophysical Research: Space Physics*, *127*, doi:10.1029/2020JA028744, 2022.

Linker, J. A., Z. Mikic, D. a Biesecker, R. J. Forsyth, S. E. Gibson, a J Lazarus, and A. Lecinski, Magnetohydrodynamic modeling of the solar corona during whole sun month, *Geohysical Research*, *104*, 9809--9830, 1999.

Liu, Y., J. A. Davies, J. G. Luhmann, A. Vourlidas, S. D. Bale, and R. P. Lin, Geometric triangulation of imaging observations to track coronal mass ejections

continuously out to 1 au, *Astrophysical Journal Letters*, *710*, 82--87, doi:10.1088/2041-8205/710/1/L82, 2010a.

Liu, Y., A. Thernisien, J. G. Luhmann, A. Vourlidas, J. A. Davies, R. P. Lin, and S. D. Bale, Reconstructing coronal mass ejections with coordinated imaging and in situ observations: Global structure, kinematics, and implications for space weather forecasting, *Astrophysical Journal*, *722*, 1762--1777, doi:10.1088/0004-637X/722/2/1762, 2010b.

Lohmeyer, W., A. Carlton, F. Wong, M. Bodeau, A. Kennedy, and K. Cahoy, Response of geostationary communications satellite solid-state power amplifiers to high-energy electron fluence, *Space Weather*, *13*, 298--315, doi:10.1002/2014SW001147, 2015.

Lugaz, N., A. Vourlidas, and I. I. Roussev, Deriving the radial distances of wide coronal mass ejections from elongation measurements in the heliosphere - application to cme-cme interaction, *Annales Geophysicae*, *27*, 3479--3488, doi:10.5194/angeo-27-3479-2009, 2009.

Lugaz, N., C. J. Farrugia, J. A. Davies, C. Möstl, C. J. Davis, I. I. Roussev, and M. Temmer, The deflection of the two interacting coronal mass ejections of 2010 may 23-24 as revealed by combined in situ measurements and heliospheric imaging, *Astrophysical Journal*, *759*, doi:10.1088/0004-637X/759/1/68, 2012.

Lugaz, N., C. J. Farrugia, R. M. Winslow, C. R. Small, T. Manion, and N. P. Savani, Importance of cme radial expansion on the ability of slow cmes to drive shocks, *The Astrophysical Journal*, *848*, 75, doi:10.3847/1538-4357/aa8ef9, 2017.

Luhmann, J. G., N. Gopalswamy, L. K. Jian, N. Lugaz, and B. J. G. Luhmann, Icme evolution in the inner heliosphere, *Solar Phys*, *295*, 61, doi:10.1007/s11207-020-01624-0, 2020.

MacNeice, P., S. K. Antiochos, A. Phillips, D. S. Spicer, C. R. DeVore, and K. Olson, A numerical study of the breakout model for coronal mass ejection initiation, *The Astrophysical Journal*, *614*, 1028--1041, doi:10.1086/423887, 2004.

MacQueen, R., Coronal transients: a summary, *Philosophical Transactions of the Royal Society of London. Series A, Mathematical and Physical Sciences*, *297*, 605--620, doi:10.1098/rsta.1980.0236, 1980.

Manchester, W., E. K. Kilpua, Y. D. Liu, N. Lugaz, P. Riley, T. Török, and B. Vršnak, The physical processes of cme/icme evolution, *Space Science Reviews*, *212*, 1159--1219, doi:10.1007/s11214-017-0394-0, 2017.

Manchester, W. B., A. Vourlidas, G. Tóth, N. Lugaz, I. I. Roussev, I. V. Sokolov, T. I. Gombosi, D. L. D. Zeeuw, and M. Opher, Three-dimensional mhd simulation of the 2003 october 28 coronal mass ejection: Comparison with lasco coronagraph observations, *The Astrophysical Journal*, *684*, 1448--1460, 2008.

Mathioudakis, M., D. B. Jess, and R. Erdélyi, Alfvén waves in the solar atmosphere: From theory to observations, *Space Science Reviews*, *175*, 1--27, doi:10.1007/s11214-012-9944-7, 2013.

Mays, M. L., et al., Ensemble modeling of cmes using the wsa–enlil+cone model, *Solar Physics*, *290*, 1775--1814, doi:10.1007/s11207-015-0692-1, 2015.

Mazur, J. E., J. F. Fennell, J. L. Roeder, P. T. O'Brien, T. B. Guild, and J. J. Likar, The timescale of surface-charging events, *IEEE Transactions on Plasma Science*, *40*, 237--245, doi:10.1109/TPS.2011.2174656, 2012.

Mccomas, D. J., S. J. Bame, P. Barker, W. C. Feldman, J. L. Phillips, P. Riley, and J. W. Griffee, Solar wind electron proton alpha monitor (swepam) for the advanced composition explorer, *Space Science Reviews*, 1998.

Merkin, V. G., J. G. Lyon, D. Lario, C. N. Arge, and C. J. Henney, Time-dependent magnetohydrodynamic simulations of the inner heliosphere, *Journal of Geophysical Research A: Space Physics*, *121*, 2866--2890, doi:10.1002/2015JA022200, 2016.

Michalek, G., An asymmetric cone model for halo coronal mass ejections, *Solar Physics*, *237*, 101–118, doi:https://doi.org/10.1007/s11207-006-0075-8, 2006.

Millward, G., D. Biesecker, V. Pizzo, and C. A. D. Koning, An operational software tool for the analysis of coronagraph images: Determining cme parameters for input

into the wsa-enlil heliospheric model, *Space Weather*, *11*, 57--68, doi:10.1002/swe.20024, 2013.

Mishra, W., N. Srivastava, and J. A. Davies, A comparison of reconstruction methods for the estimation of coronal mass ejections kinematics based on secchi/hi observations, *The Astrophysical Journal*, *784*, 135, doi:10.1088/0004-637X/784/2/135, 2014.

Moldwin, M., *An Introduction To Space Weather*, 6 ed., 1-134 pp., Cambridge University Press, 2016.

Moortel, I. D., and P. Browning, Recent advances in coronal heating, *Philosophical Transactions of the Royal Society A: Mathematical, Physical and Engineering Sciences*, *373*, 20140,269, doi:10.1098/rsta.2014.0269, 2015.

Morgan, H., and A. C. Cook, The width, density, and outflow of solar coronal streamers, *The Astrophysical Journal*, *893*, 57, doi:10.3847/1538-4357/ab7e32, 2020.

Mundra, K., V. Aparna, and P. Martens, Using cme progenitors to assess cme geoeffectiveness, *The Astrophysical Journal Supplement Series*, *257*, 33, doi:10.3847/1538-4365/ac3136, 2021.

Murray, S. A., The importance of ensemble techniques for operational space weather forecasting, *Space Weather*, *16*, 777--783, doi:10.1029/2018SW001861, 2018.

Möstl, C., M. Temmer, T. Rollett, C. J. Farrugia, Y. Liu, A. M. Veronig, M. Leitner, A. B. Galvin, and H. K. Biernat, Stereo and wind observations of a fast icme flank triggering a prolonged geomagnetic, *Geophys. Res. Lett*, *37*, 24,103, doi:10.1029/2010GL045175, 2010.

Möstl, C., J. A. Davies, M. M. Bisi, R. A. Harrison, and N. Lugaz, Speeds and arrival times of solar transients approximated by self-similar expanding circular fronts, *Solar Phys*, *285*, 411--423, doi:10.1007/s11207-012-9978-8, 2013.

Möstl, C., et al., Strong coronal channelling and interplanetary evolution of a solar storm up to earth and mars, *Nature*, doi:10.1038/ncomms8135, 2015.

Möstl, C., et al., Modeling observations of solar coronal mass ejections with heliospheric imagers verified with the heliophysics system observatory, *Space Weather*, *15*, 955--970, doi:10.1002/2017SW001614, 2017.

Odstrcil, D., Modeling 3-d solar wind structure, *Advances in Space Research*, *32*, 497--506, doi:10.1016/S0273-1177(03)00332-6, 2003.

Odstrcil, D., P. Riley, and X. P. Zhao, Numerical simulation of the 12 may 1997 interplanetary cme event, *J. Geophys. Res*, *109*, 2116, doi:10.1029/2003JA010135, 2004.

Oughton, E. J., A. Skelton, R. B. Horne, A. W. P. Thomson, and C. T. Gaunt, Quantifying the daily economic impact of extreme space weather due to failure in electricity transmission infrastructure, *Space Weather*, *15*, 65--83, doi:10.1002/2016SW001491, 2017.

Oughton, E. J., et al., A risk assessment framework for the socioeconomic impacts of electricity transmission infrastructure failure due to space weather: An application to the united kingdom, *Risk Analysis*, *39*, 1022--1043, doi:10.1111/risa.13229, 2019.

Owens, M., and P. Cargill, Non-radial solar wind flows induced by the motion of interplanetary coronal mass ejections, *Annales Geophysicae*, *22*, 4397--4406, doi:10.5194/angeo-22-4397-2004, 2004.

Owens, M., et al., A computationally efficient, time-dependent model of the solar wind for use as a surrogate to three-dimensional numerical magnetohydrodynamic simulations, *Solar Physics*, *295*, doi:10.1007/s11207-020-01605-3, 2020a.

Owens, M. J., Solar-wind structure, doi:10.1093/acrefore/9780190871994.013.19, 2020.

Owens, M. J., and R. J. Forsyth, The heliospheric magnetic field, *Living Reviews in Solar Physics*, *10*, doi:10.12942/lrsp-2013-5, 2013.

Owens, M. J., P. J. Cargill, C. Pagel, G. L. Siscoe, and N. U. Crooker, Characteristic magnetic field and speed properties of interplanetary coronal mass ejections and

their sheath regions, *Journal of Geophysical Research: Space Physics*, *110*, doi: 10.1029/2004JA010814, 2005.

Owens, M. J., V. G. Merkin, and P. Riley, A kinematically distorted flux rope model for magnetic clouds, *Journal of Geophysical Research: Space Physics*, *111*, 1--8, doi:10.1029/2005JA011460, 2006.

Owens, M. J., M. Lockwood, and L. A. Barnard, Coronal mass ejections are not coherent magnetohydrodynamic structures, *Scientific Reports*, *7*, 1--6, doi:10.1038/ s41598-017-04546-3, 2017.

Owens, M. J., M. Lang, P. Riley, M. Lockwood, and A. S. Lawless, Quantifying the latitudinal representivity of in situ solar wind observations, *Journal of Space Weather and Space Climate*, *10*, doi:10.1051/swsc/2020009, 2020b.

Pant, V., S. Willems, L. Rodriguez, M. Mierla, D. Banerjee, and J. A. Davies, Automated detection of coronal mass ejections in stereo heliospheric imager data, *The Astrophysical Journal*, *833*, 80, doi:10.3847/1538-4357/833/1/80, 2016.

Parker, E. N., The formation of sunspots from the solar toroidal field., *The Astrophysical Journal*, *121*, 491, doi:10.1086/146010, 1955.

Parker, E. N., Dynamics of the interplanetary gas and magnetic fields, *Astrophysical Journal*, *128*, 664, doi:10.1086/146579, 1958.

Pizzo, V., G. Millward, A. Parsons, D. Biesecker, S. Hill, and D. Odstrcil, Wang-sheeley-arge-enlil cone model transitions to operations, *Space Weather*, *9*, 2, doi:10.1029/2011SW000669, 2011.

Plunkett, S. P., et al., The relationship of green-line transients to white-light coronal mass ejections, *Solar Physics*, *175*, 699--718, 1997.

Pomoell, J., and S. Poedts, Euhforia: European heliospheric forecasting information asset, *Journal of Space Weather and Space Climate*, *8*, doi:10.1051/swsc/2018020, 2018.

Priest, E., Solar physics: Overview, doi:10.1093/acrefore/9780190871994.013.21, 2020.

Pultarova, T., Powerful solar storm delays spacex rocket launch, stalls oil rigs in canada amid aurora-palooza, `https://www.space.com/solar-storm-delays-spacex-launch-supercharges-auroras`, 2023.

Reale, F., Coronal loops: Observations and modeling of confined plasma, *Living Reviews in Solar Physics*, *7*, doi:10.12942/lrsp-2010-5, 2010.

Reay, S. J., W. Allen, O. Baillie, J. Bowe, E. Clarke, V. Lesur, and S. Macmillan, Space weather effects on drilling accuracy in the north sea, *Annales Geophysicae*, *23*, 3081--3088, doi:10.5194/angeo-23-3081-2005, 2005.

Richardson, I. G., and H. V. Cane, Near-earth interplanetary coronal mass ejections during solar cycle 23 (1996–2009): Catalog and summary of properties, *Solar Physics*, *264*, 189--237, doi:10.1007/s11207-010-9568-6, 2010.

Riley, P., and R. Lionello, Mapping solar wind streams from the sun to 1 au: A comparison of techniques, *Solar Physics*, *270*, 575--592, doi:10.1007/s11207-011-9766-x, 2011.

Riley, P., J. A. Linker, and Z. Mikić, An empirically-driven global mhd model of the solar corona and inner heliosphere, *Journal of Geophysical Research: Space Physics*, *106*, 15,889--15,901, doi:10.1029/2000JA000121, 2001.

Riley, P., et al., Forecasting the arrival time of coronal mass ejections: Analysis of the ccmc cme scoreboard, *Space Weather*, *16*, 1245--1260, doi:10.1029/2018SW001962, 2018a.

Riley, P., et al., Forecasting the arrival time of coronal mass ejections: Analysis of the ccmc cme scoreboard, *Space Weather*, *16*, 1245--1260, doi:10.1029/2018SW001962, 2018b.

Rodriguez, L., C. Scolini, M. Mierla, A. N. Zhukov, and M. J. West, Space weather monitor at the l5 point: A case study of a cme observed with stereo b, *Space Weather*, *18*, doi:10.1029/2020SW002533, 2020.

Rollett, T., C. Möstl, M. Temmer, A. M. Veronig, C. J. Farrugia, and H. K. Biernat, Constraining the kinematics of coronal mass ejections in the inner heliosphere with

in-situ signatures, *Solar Physics*, *276*, 293--314, doi:10.1007/s11207-011-9897-0, 2012.

Rollett, T., C. Möstl, A. Isavnin, J. A. Davies, M. Kubicka, U. V. Amerstorfer, and R. A. Harrison, Elevohi: A novel cme prediction tool for heliospheric imaging combining an elliptical front with drag-based model fitting, *The Astrophysical Journal*, doi:10.3847/0004-637X/824/2/131, 2016.

Rouillard, A. P., et al., First imaging of corotating interaction regions using the stereo spacecraft, *Res. Lett*, *35*, 10,110, doi:10.1029/2008GL033767, 2008.

Russell, A. J. B., A. R. Yeates, and J. P. Eastwood, Magnetic reconnection now and in the future, *Astronomy & Geophysics*, *56*, 6.18--6.23, doi:10.1093/astrogeo/atv197, 2015.

Savani, N. P., M. J. Owens, A. P. Rouillard, R. J. Forsyth, and J. A. Davies, Observational evidence of a coronal mass ejection distortion directly attributable to a structured solar wind, *The Astrophysical Journal*, *714*, L128--L132, doi: 10.1088/2041-8205/714/1/L128, 2010.

Schatten, K. H., Current sheet magnetic model for the solar corona., *Cosmic Electrodynamics*, *2*, 232--245, 1971.

Schatten, K. H., J. M. Wilcox, and N. F. Ness, A model of interplanetary and coronal magnetic fields, *Solar Physics*, *6*, 442--455, doi:10.1007/BF00146478, 1969.

Scolini, C., C. Verbeke, S. Poedts, E. Chané, J. Pomoell, and F. P. Zuccarello, Effect of the initial shape of coronal mass ejections on 3-d mhd simulations and geoeffectiveness predictions, *Space Weather*, *16*, 754--771, doi:10.1029/2018SW001806, 2018.

Scott, C. J., M. J. Owens, C. A. de Koning, L. A. Barnard, S. R. Jones, and J. Wilkinson, Using ghost fronts within stereo heliospheric imager data to infer the evolution in longitudinal structure of a coronal mass ejection, *Space Weather*, *17*, 539--552, doi:10.1029/2018SW002093, 2019.

Sedares, L. M., R. J. Redmon, J. Rodriguez, B. Nowak, and A. Galvan, Determining if the root cause of an anomaly is a single event upset, *SpaceOps 2016 Conference*, doi:10.2514/6.2016-2564, 2016.

Sharpe, M. A., and S. A. Murray, Verification of space weather forecasts issued by the met office space weather operations centre, *Space Weather*, *15*, 1383--1395, doi:10.1002/2017SW001683, 2017.

Sheeley, N. R., J. H. Walters, Y.-M. Wang, and R. A. Howard, Continuous tracking of coronal outflows: Two kinds of coronal mass ejections, *Journal of Geophysical Research: Space Physics*, *104*, 24,739--24,767, doi:10.1029/1999ja900308, 1999.

Sheeley, N. R., et al., Heliospheric images of the solar wind at earth, *Astrophysical Journal*, *675*, 853--862, 2008.

Smith, B., Animation: Nasa's parker solar probe enters solar atmosphere, `https://svs.gsfc.nasa.gov/14036#section_credits`, 2021.

Stakhiv, M., S. T. Lepri, E. Landi, P. Tracy, and T. H. Zurbuchen, On solar wind origin and acceleration: Measurements from ace, *The Astrophysical Journal*, *829*(2), 117, doi:10.3847/0004-637X/829/2/117, 2016.

Steenbeck, M., F. Krause, and K.-H. Rädler, Berechnung der mittleren lorentz-feldstärke für ein elektrisch leitendes medium in turbulenter, durch coriolis-kräfte beeinflußter bewegung, *Zeitschrift für Naturforschung A*, *21*, 369--376, doi:10.1515/zna-1966-0401, 1966.

Stix, M., *The Sun's Differential Rotation*, pp. 248--266, Springer, Berlin, Heidelberg, doi:10.1007/978-3-642-75183-7_23, 1989.

Stix, M., *The Sun: an introduction*, Springer Science & Business Media, 2004.

Stone, E. C., A. M. Frandsen, R. A. Mewaldt, E. R. Christian, D. Margolies, J. F. Ormes, and F. Snow, The advanced composition explorer, *Space Science Reviews*, 1998.

Subramanian, P., and A. Vourlidas, Energetics of solar coronal mass ejections, *Astronomy and Astrophysics*, *467*, 685--693, doi:10.1051/0004-6361:20066770, 2007.

Taktakishvili, A., P. MacNeice, and D. Odstrcil, Model uncertainties in predictions of arrival of coronal mass ejections at earth orbit, *Space Weather*, *8*, 1--9, doi: 10.1029/2009SW000543, 2010.

Taktakishvili, A., A. Pulkkinen, P. MacNeice, M. Kuznetsova, M. Hesse, and D. Odstrcil, Modeling of coronal mass ejections that caused particularly large geomagnetic storms using enlil heliosphere cone model, *Space Weather*, *9*, n/a--n/a, doi:10.1029/2010SW000642, 2011.

Temmer, M., T. Rollett, C. Möstl, A. M. Veronig, B. Vršnak, and D. Odstrçil, Influence of the ambient solar wind flow on the propagation behavior of interplanetary coronal mass ejections, *Astrophysical Journal*, *743*, doi:10.1088/0004-637X/743/2/101, 2011.

Thomas, J. H., and N. O. Weiss, *Sunspots: Theory and Observations*, vol. 375, Springer Netherlands, doi:10.1007/978-94-011-2769-1, 1992.

Thomas, S. R., A. Fazakerley, R. T. Wicks, and L. Green, Evaluating the skill of forecasts of the near-earth solar wind using a space weather monitor at l5, *Space Weather*, *16*, 814--828, doi:10.1029/2018SW001821, 2018.

Thomson, A., C. Gaunt, P. Cilliers, J. Wild, B. Opperman, L.-A. McKinnell, P. Kotze, C. Ngwira, and S. Lotz, Present day challenges in understanding the geomagnetic hazard to national power grids, *Advances in Space Research*, *45*, 1182--1190, doi:10.1016/j.asr.2009.11.023, 2010.

Thomson, A. W. P., E. B. Dawson, and S. J. Reay, Quantifying extreme behavior in geomagnetic activity, *Space Weather*, *9*, doi:10.1029/2011SW000696, 2011.

Tomczyk, S., S. W. Mcintosh, S. L. Keil, P. G. Judge, T. Schad, D. H. Seeley, and J. Edmondson, Alfvén waves in the solar corona, *New Series*, *317*, 1192--1196, doi:10.1126/science.ll46421, 2007.

Török, T., and B. Kliem, The evolution of twisting coronal magnetic flux tubes, , *406*, 1043--1059, doi:10.1051/0004-6361:20030692, 2003.

Tousey, R., The solar corona, *Space Research Conference*, pp. 713--730, 1973.

Tsurutani, B. T., and G. S. Lakhina, Magnetic reconnection in the earth's magnetosphere, 1997.

Tsurutani, B. T., W. D. Gonzalez, G. S. Lakhina, and S. Alex, The extreme magnetic storm of 1 - 2 september 1859, *Journal of Geophysical Research*, doi:10.1029/2002JA009504, 2003.

Tucker-Hood, K., et al., Validation of a priori cme arrival predictions made using real-time heliospheric imager observations, *Space Weather*, *13*, 35--48, doi:10.1002/2014SW001106, 2015.

Turner, H., M. J. Owens, M. S. Lang, and S. Gonzi, The influence of spacecraft latitudinal offset on the accuracy of corotation forecasts, *Space Weather*, *19*, 1--15, doi:10.1029/2021sw002802, 2021.

Tóth, G., et al., Space weather modeling framework: A new tool for the space science community, *Journal of Geophysical Research: Space Physics*, *110*, 1--21, doi:10.1029/2005JA011126, 2005.

Török, T., C. Downs, J. A. Linker, R. Lionello, V. S. Titov, Z. Mikić, P. Riley, R. M. Caplan, and J. Wijaya, Sun-to-earth mhd simulation of the 2000 july 14 "bastille day" eruption, *The Astrophysical Journal*, *856*, 75, doi:10.3847/1538-4357/aab36d, 2018.

Verbeke, C., et al., Benchmarking cme arrival time and impact: Progress on metadata, metrics, and events, *Space Weather*, *17*, 6--26, doi:10.1029/2018SW002046, 2019.

Vourlidas, A., Mission to the sun-earth l5 lagrangian point: An optimal platform for space weather research, *Space Weather*, *13*, 197--201, doi:10.1002/2015SW001173, 2015.

Vourlidas, A., and R. A. Howard, The proper treatment of coronal mass ejection brightness: A new methodology and implications for observations, *Astrophysical Journal*, pp. 1216--1221, 2006.

Vourlidas, A., P. Subramanian, K. P. Dere, and R. A. Howard, Large-angle spectrometric coronagraph measurements of the energetics of coronal mass ejections, *THE ASTROPHYSICAL JOURNAL*, *534*, 456--467, 2000.

Vršnak, B., Deceleration of coronal mass ejections, *Solar Physics*, *202*, 2001.

Vršnak, B., Forces governing coronal mass ejections, *Advances in Space Research*, *38*(3), 431--440, doi:10.1016/j.asr.2005.03.090, coronal Mass Ejections and Solar Particle Events in Solar Cycle 23, 2006.

Vršnak, B., D. Ruždjak, D. Sudar, and N. Gopalswamy, Kinematics of coronal mass ejections between 2 and 30 solar radii: What can be learned about forces governing the eruption?, *Astronomy and Astrophysics*, *423*, 717--728, doi:10.1051/0004-6361:20047169, 2004.

Vršnak, B., D. Vrbanec, and J. Čalogović, Dynamics of coronal mass ejections, *Astronomy & Astrophysics*, *490*, 811--815, doi:10.1051/0004-6361:200810215, 2008.

Vršnak, B., M. Temmer, T. Žic, A. Taktakishvili, M. Dumbović, C. Möstl, A. M. Veronig, M. L. Mays, and D. Odstrčil, Heliospheric propagation of coronal mass ejections: Comparison of numerical wsa-enlil+cone model and analytical drag-based model, *Astrophysical Journal, Supplement Series*, *213*, doi:10.1088/0067-0049/213/2/21, 2014.

Wang, Y.-M., Coronal holes and open magnetic flux, *Space Science Reviews*, *144*, 383--399, doi:10.1007/s11214-008-9434-0, 2009.

Webb, D. F., and T. A. Howard, Coronal mass ejections: Observations, *Living Reviews in Solar Physics*, *9*, doi:10.12942/lrsp-2012-3, 2012.

Webb, D. F., S. W. Kahler, P. S. Mcintosh, and J. A. Klimchuck, Large-scale structures and multiple neutral lines associated with coronal mass ejections, *JOURNAL OF GEOPHYSICAL RESEARCH*, *102*, 161--185, doi:10.1029/97JA01867, 1997.

Welsch, B. T., Magnetic flux cancellation and coronal magnetic energy, *The Astrophysical Journal*, *638*, 1101--1109, doi:10.1086/498638, 2006.

Wuelser, J.-P., et al., Euvi: the stereo-secchi extreme ultraviolet imager, *Telescopes and Instrumentation for Solar Astrophysics*, *5171*, 111, doi:10.1117/12.506877, 2004.

Y.-M. Wang, E. R., R. Grappin, and N. R. S. Jr, On the nature of the solar wind from coronal pseudostreamers, *The Astrophsyical Journal*, *749*(2), doi:10.1088/0004-637X/749/2/182, 2012.

Yardley, S. L., L. M. Green, L. van Driel-Gesztelyi, D. R. Williams, and D. H. Mackay, The role of flux cancellation in eruptions from bipolar ars, *The Astrophysical Journal*, *866*, 8, doi:10.3847/1538-4357/aade4a, 2018.

Zhang, M., X. S. Feng, and L. P. Yang, Three-dimensional mhd simulation of the 2008 december 12 coronal mass ejection: From the sun to interplanetary space, *Journal of Space Weather and Space Climate*, *9*, 1--17, doi:10.1051/swsc/2019034, 2019.

Zhao, X. P., and J. T. Hoeksema, The magnetic field at the inner boundary of the heliosphere around solar minimum, *Solar Physics*, *266*, 379--390, doi:10.1007/s11207-010-9618-0, 2010.

Zhao, X. P., S. P. Plunkett, and W. Liu, Determination of geometrical and kinematical properties of halo coronal mass ejections using the cone model, *Solar and Heliospheric Physics*, doi:10.1029/2001JA009143, 2002.

Zheng, Y., et al., Forecasting propagation and evolution of cmes in an operational setting: What has been learned, *Space Weather*, *11*, 557--574, doi:10.1002/swe.20096, 2013.

Zurbuchen, T. H., and I. G. Richardson, In-situ solar wind and magnetic field signatures of interplanetary coronal mass ejections, *Spacce Science Reviews*, *0*, 2006.